NATIONAL TECHNICAL UNIVERSITY OF ATHENS
SCHOOL OF NAVAL ARCHITECTURE AND MARINE ENGINEERING
SHIPBUILDING TECHNOLOGY LABORATORY

EXPERIMENTAL AND NUMERICAL STUDY OF A STEEL-TO-COMPOSITE ADHESIVE JOINT UNDER BENDING MOMENTS

DIPLOMA THESIS

Andrianakis Andreas

Supervisor: Tsouvalis N.

Athens, October 2011

NATIONAL TECHNICAL UNIVERSITY OF ATHENS

SCHOOL OF NAVAL ARCHITECTURE AND MARINE ENGINEERING

SHIPBUILDING TECHNOLOGY LABORATORY

EXPERIMENTAL AND NUMERICAL STUDY OF A STEEL-TO-COMPOSITE ADHESIVE JOINT UNDER BENDING MOMENTS

Andrianakis Andreas

Supervisor: Tsouvalis N.

Athens, October 2011

ACKNOWLEDGEMENTS

I would like to show my gratitude from this point to my supervisor, Tsouvalis N., for all his guidance and support in order to make this project reality.

I am also heartily thankful to Anyfantis K., whose encouragement and guidance enabled me to develop an understanding of the subject.

As a major part of this thesis took place at the Technical University of Denmark and at Risø National Laboratory for Sustainable Energy, it is a pleasure to thank all the people that made this collaboration possible. Firstly, I would like to thank my supervisor professor at DTU, Berggreen C., for all his help and counseling during my stay in Denmark. A special thanks must be given to the Head of the Research Program at Materials Research Division at Risø DTU, Sørensen B.F.; his deep understanding of the subject was a catalyst for this project. Finally, I would like to thank Vogeley E. for providing me all the technical help that was needed for the experimental tests.

I am indebted to these people for all the time they spent on this project.

Contents

1. INTRODUCTION

1.1 Adhesive joints

Throughout the history of mankind adhesives have played an important role. Human structures are usually made of separate parts which are joined together and bonding techniques have been developed in order to facilitate the assembly of such structures. The oldest known use of adhesive is actually dated to about 200,000 BC as shown by a discovery made recently [1], where some spear stone flakes were found glued to a wood with birch bark tar. However, it isn't but until the past century that science and industry enabled the development of a vast range of adhesives with the introduction of synthetic polymers. Before then, the only adhesives available were derived from natural sources such as plants and animal collagen. In the 1930s, the first synthetic resin glues were produced, followed by epoxies, neoprenes and acrylonitriles during the World War II, where technology advanced under the pressure of improvement of weapons. All these led the adhesive technology to a leap and to the development of many industries of highly specialized adhesives which can be applied to almost all type of constructions. Today, despite all this progress, natural adhesives are the ones dominating the market since they are less expensive than the synthetic-based and they usually meet the standards of the intended function.

In Table 1 the most common uses of adhesives can be seen. The industry which has been using adhesives the most so far and has been leading the improvement of adhesive technology is the aircraft and aerospace industry. For this industry light weight is the main key for an efficient construction. Adhesive joining is ideal for this purpose and has been used to bring together a variety of materials through time, from wood to aluminium and titanium. It can be mentioned that the Boeing 787 and the Airbus A 350 contain more than 50% bonded composite structure.

By extrapolating the experience gained from the aircraft industry, adhesives are starting to be used more and more by other industries like the marine industry. Contributing to this fact is a long list of advantages offered by the adhesive bonding technology compared to other bonding techniques, like welding or bolting. First of all, adhesive bonding offers the possibility of joining completely dissimilar materials, including metals, independent of their metallurgical properties. As it was mentioned before, another main advantage of adhesive joining is the reduction of the weight of the structure. Additionally, adhesives offer a superior flexibility in order to join dissimilar materials, enabling the designer to choose the most fitting material for each part of structure. They provide vibration isolation and they give no shape distortion, improving the appearance of the structure and avoiding any surface modifications. They also provide galvanic isolation, a fact that reduces corrosion when joining different metals. Finally, a very important factor why adhesive bonding is preferred to other techniques is the better load carrying capability it offers, since the stresses are distributed more uniformly than welding or bolting (where stress concentration areas are easily observed).

Especially for the marine industry a few more advantages can be mentioned when choosing adhesive bonding with patches to repair damaged areas. The hotwork of welding is avoided, minimizing thus the risk of a fire, plus the repair can be done on the spot with no need of dry-docking of the ship. The stripping out of neighboring compartments needed for welding is also avoided. The sealing of the cracks made by adhesive joining is water-tight and it can be performed on complex surface

geometries. Repairs of this kind can adapt to any substrate geometry and fit into places where normal welding would not easily reach. The maintenance cost is reduced and the materials used are light, so they are easy to transport and to handle with no need of heavy lifting machinery.

Table 1.1. **Common uses of adhesives in various industries.**

Industry	**Applications**
Construction	Manufacture and installation of laminated wood panels, prefabricated beams, wall panels, general building construction; installation of flooring, tile, carpeting, ceiling panels and wall coverings.
Consumer goods	Manufacture of office supplies, hobby and model supplies, and stationery.
Nonrigid bonding	Bonding of woven and non-woven fabrics; manufacture of athletic shoes, rugs, filters, books, and sporting goods.
Packaging	Manufacture of cartons, boxes and corrugated boards; bags, envelopes, disposable products (paper products); cigarettes; and labels and stamps.
Rigid bonding	Manufacture of appliances, electronics, household products and furniture.
Tapes	Manufacture of all tapes, including those used for surgery, packaging, industrial applications, consumer applications and masking applications.
Transportation	Aircraft and aerospace structural assemblies; automotive, truck, boat, and bus assembly; mobile home manufacturing.

The limitations presented when choosing adhesive bonding concern mainly the preparation of the surfaces that are to be bonded. Surface preparation is critical to make the joint efficient: the surfaces should be totally clean from grease and oil and as flat as possible. Abraded surfaces are preferred rather than totally smooth ones, since they provide better bonding strength due to the interlocking of the adhesive material in the surface microvoids. It also removes unwanted particles like oxides, rust, paints etc. The most common abrading techniques are sand blasting, wire brushing and sanding by glass paper. Chemical pretreatment of the surface may sometimes be applied if additional cleaning is needed. Additionally, for many adhesives, the environmental conditions have to be kept constant in time to guarantee the required joint properties and many adhesives have limited storage life or need to be refrigerated limiting this way their application. Moreover, since adhesives belong in the class of materials known as ‘polymers’ or ‘synthetic resins’, they present the same limitations with these materials. They are less strong than metals and their properties are very temperature dependent: with increasing temperature the bond strength decreases and the strain properties become more and more plastic. The transition temperature depends on the particular adhesive with usual values ranging from 70 to 220^{o}C. Adhesives also have a curing time during which the strength of the bond increases up to a maximum level, which means that maximum strength is not reached immediately as with mechanical fastening or welding. Finally, if any damage is

presented in an adhesive joint, a repair cannot easily be made: bonded assemblies cannot be dismantled as easily as mechanically fastened joints.

Other parameters that should be taken into account when choosing adhesive joining are the properties of the adhesive and the adherends. These are likely to influence the stress distribution of the structure: a mismatch between the coefficient of thermal expansion of the adhesive and the adherends could lead to substantial internal stresses. The modulus of elasticity of the adhesive can make the joint either compliant (low modulus producing low stresses) or rigid (high modulus producing high internal stresses). Also, high flexibility and toughness of the adhesive are required for a longer life service of the joint.

Today, adhesive industry can offer a vast variety of adhesives which can be categorized using different ways: their chemistries (epoxies, polyimides etc.), their form (paste, liquid, film, pellets, tape), their type (hot melt, thermosetting, pressure sensitive etc.). They may be applied on the adherends in different ways depending on their form: this can be done by either manually spreading the adhesive on a surface or even sophisticated robotic machinery can be used if it is needed.

As in every structure, design is an important aspect of an adhesive joint. If a structure was designed to be bonded for welding or mechanical fastening it is not proper to simply change to adhesive bonding. Design factors of an adhesive joint include the joint geometry, the manufacturing conditions, the working conditions of the structure, the mechanical properties of the adherends and the adhesive. Adhesive joints can be subjected to tensile, shear, peel or compressive stresses, most often in a combination of them. They perform better in shear, compression and tension while they are usually less effective under peel and cleavage loading. A proper design should direct the loading conditions of the joint along the lines of the adhesive's greatest strength.

In Figure 1.1, five different loading conditions of an adhesive joint are presented along with the stress distribution. It can be seen that while tension, compression and shear produce a more uniform distribution of stresses, cleavage and peel produce a single line of high stress. That means that cleavage and peel should be avoided as much as possible during the design of a bonded joint.

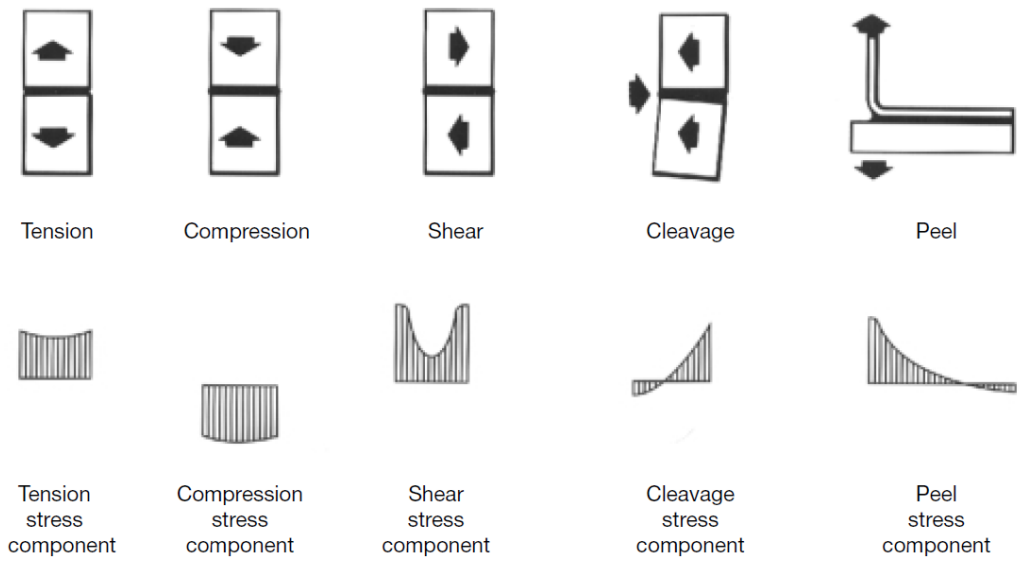

Figure 1.1 Loading conditions and stress distribution of an adhesive joint

Although adhesive joint design is used successfully in many industries offering all the advantages mentioned before and proving the viability of this technology, a complete transition to adhesive bonding has not yet been made. And as it seems this situation will not change for the next years, although there is a clear rising trend. This is due to the lesser understanding of the adhesive joint performance over the life of a structure compared to other bonding techniques. Furthermore, there are still problems concerning the control of all the manufacturing variables to the extent needed for the validation of the bonding. What is needed in order to expand the application of adhesive joints is to obtain more research results, which will prove the efficiency of this technology.

1.2. Cohesive Zone Model

Before any technology is applied, its effectiveness must be validated through an experimental procedure. The same rule applies to adhesive bonding and as it was said before, the fact that so far there haven't been any conclusive research results proving the efficiency of adhesive bonding is what makes this technology not being universally applied.

The prediction of the deformation of adhesive joints can be done quite easily by describing the elastic properties of the structure. What is important now is to develop proper tools that will be able to predict the failure evolution of adhesive joints. That includes all the stages of the failure: crack initiation, propagation and crack size.

The fracture of adhesive joints is located at the weakest point of the structure and is usually divided into two types: usually at either the interface of the adhesive and the adherend (interfacial failure) or inside the adhesive itself (cohesive failure)-as adhesives usually are less strong than the adherends. These types of failure are shown in Figure 1.2 and 1.3.

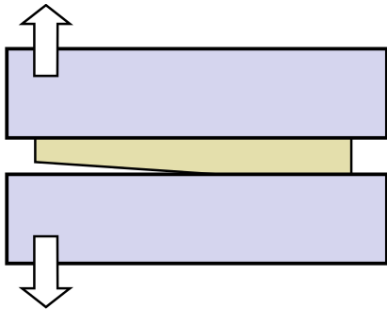

Figure 1.2. Interfacial failure of an adhesive joint.

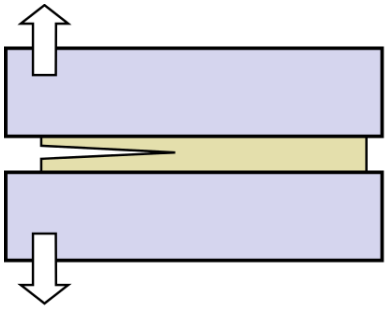

Figure 1.3 Cohesive failure of an adhesive joint.

The use of interfacial fracture mechanics is the approach that is mostly used in order to analyze the fracture of adhesive joints.

Modern fracture mechanics is mostly based on the work done by A. A. Griffith, who in 1921 presented a criterion for brittle fracture in elastic materials. According to the criterion, fracture is initiated at flaws in the material, where at such points the stresses are mathematically infinite at almost any load. The criterion was based on the concept of a critical energy balance between the energy required to create new surface area with the propagation of the crack and the strain energy released. Griffith showed that this mathematical infinity could be circumvented by

taking into account the integrated strain energy for an elastic plate with such flaws. An equation of the form $\sigma_c=K(E\gamma_c/\alpha)^{1/2}$ is the result of the balance between this energy and the one required to create the fracture surface, where σ_c is the stress required for crack propagation, K is a geometric factor depending on the shape of the flaw and mode of loading, E is the Young's modulus of elasticity, α is the flaw size and γ_c is the specific fracture energy.

Interfacial fracture mechanics uses a very much similar logic and energy balance. It should also be noted that Williams [2] introduced the idea of cohesive and interfacial failure being physically similar, with their difference concentrated on the fact that the different material properties on either side of the crack should be taken into account along with the different interpretation of the specific fracture energy: for cohesive failure the specific fracture energy is the required energy to create a unit of new fracture energy; for adhesive failure is defined by the energy per unit area required to separate the two materials.

Studies on bi-material systems begin many decades ago starting with the work presented by Williams [3] and many other studies following that. Most of the above mentioned studies use the linear elastic fracture mechanics (LEFM), obtaining this way good results. However, it must be pointed that despite the fairly good approximations of these studies, LEFM cannot be always used due to some limitations that may occur. For example, if during crack initiation and propagation the interface presents nonlinear behavior the elasticity theory is no longer valid. Also, the use of toughened adhesives may lead to a significant extension of the plastic zone, so that the small-scale yielding assumption cannot be used anymore, which invalidates the LEFM theory.

Seeing these limitations of LEFM, work was made in creating a new model that would overcome this problem. So, the theory of nonlinear fracture mechanics (NLFM) was introduced. Barenblatt [4] and Dugdale [5] proposed the cohesive zone model in 1960's, where stresses across a potential crack path are bounded and that a traction-separation law can describe locally the fracture behavior inside the cohesive zone ahead of the crack tip. But something more was needed in order to relate the local cohesive zone to the global behavior. And that was done by Rice [6] with his theory of J-integral, where large-scale plasticity and the interfacial nonlinear behavior can be considered. And the fact that the status of the energy release rate during crack initiation can be related to a status of the local traction-separation law made the connection between local and global behavior.

Despite being introduced in the 1960's, cohesive zone models only recently started being more and more used with the advance of numerical analysis. Cohesive zone elements can be introduced in Finite Element codes and simulate quite well crack initiation and propagation, and according to new methods by some researchers (e.g. Zhang and Paulino [7]) the crack path can also be predicted.

The concept of a cohesive law is that the stress along the crack faces of the fracture process zone can be described by a traction-separation law. That means that the local normal stress σ_n and the local shear stress σ_t inside the process zone are functions of the local normal crack opening δ_n and tangential opening δ_t. This can be written as:

$$\sigma_n = \sigma_n(\delta_n, \delta_t), \qquad \sigma_t = \sigma_t(\delta_n, \delta_t) \tag{1.1}$$

According to [8], the evaluation of the path-independent J-integral along a path around the fracture process zone yields:

$$J = \int_0^{\delta_n^*} \sigma_n(\delta_n, \delta_t) d\delta_n + \int_0^{\delta_t^*} \sigma_t(\delta_n, \delta_t) d\delta_t \tag{1.2}$$

with δ_n^* and δ_t^* defined as the normal and tangential crack opening displacement at the cohesive zone respectively, as seen in Figure 1.4.

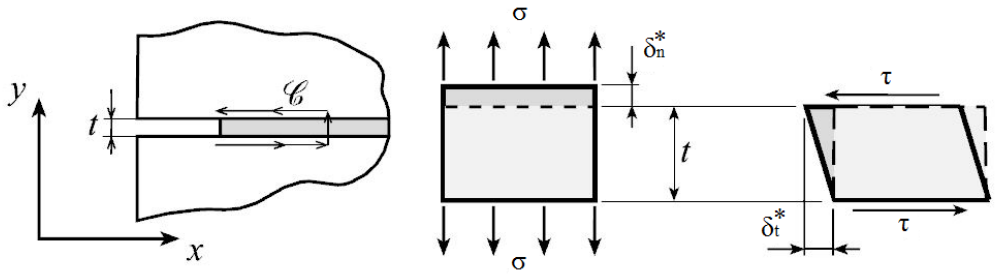

Figure 1.4. Adhesive joint and basic deformation modes of an adhesive layer with thickness t under normal stress σ and shear stress τ.

When $\delta_n^* \neq 0$ and $\delta_t^* = 0$, a situation called pure normal opening or Mode I (see Figure 1.5) the second integral of the Equation (1.2) turns to zero, and the equation now yields:

$$\sigma_n(\delta^*_n) = \frac{\partial J}{\partial \delta^*_n} \tag{1.3}$$

and the pure Mode I cohesive law is derived by differentiation. Respectively, the pure Mode II cohesive law can be derived when only tangential opening is present, meaning that $\delta_n = 0$, by the following equation:

$$\sigma_t(\delta^*_t) = \frac{\partial J}{\partial \delta^*_t} \tag{1.4}$$

As it can be seen, it is assumed that the local cohesive stresses depend on the local opening displacement but not on the crack opening history.

It will also be assumed that the cohesive laws are decoupled and independent, as done by [9]. This means that there is no interaction between the pure Mode I and pure Mode II cohesive law and that the normal cohesive stresses depend weakly on the tangential crack opening and that the shear stresses depend weakly on the normal crack opening.

$$\sigma_n = \sigma_n(\delta_n), \qquad \sigma_t = \sigma_t(\delta_t) \tag{1.5}$$

This leads to the ability to measure pure Mode cohesive laws under mixed mode loading by measuring both the normal and tangential crack opening.

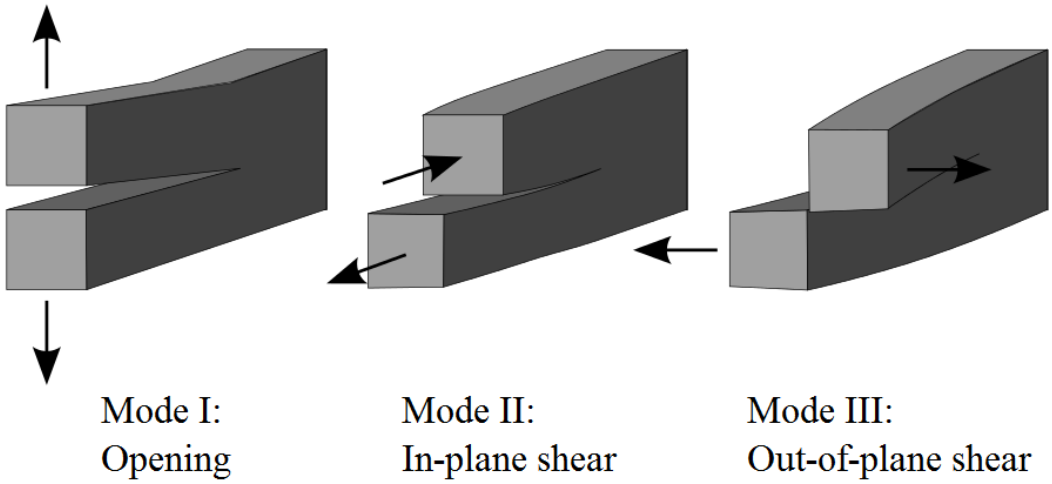

Figure 1.5. Opening modes of an adhesive joint.

The importance of cohesive laws is that they can be introduced in Finite Element models and predict the failure of adhesive joints. So far, many models have been used in the literature assuming an idealized shape and function of the cohesive law. The most commonly used are of the following shapes: bilinear, exponential and trapezoidal [10]. These three types are presented in Figure 1.6. Their analytical expressions are:

- *Bilinear law*

$$\sigma = \begin{cases} K_0\delta & \text{if } \delta \leqslant a_0, \\ \frac{a_1-\delta}{a_1-a_0}\sigma_0 & \text{if } a_0 \leqslant \delta \leqslant a_1, \\ 0 & \text{if } \delta \geqslant a_1, \end{cases} \tag{1.6}$$

where α_0 and α_1 can be seen in Figure 1.6, and they are given by $\alpha_0 = \frac{\sigma_0}{K_0}, \alpha_1 = \frac{2G_c}{\sigma_0}$, G_c represents the fracture energy dissipated during the complete debonding process and is equal to the area enclosed by the σ-δ curve and K_0 is the initial penalty stiffness. If K_0 takes very high values, it means that the law gives a very stiff initial approach, with the traction being non-zero when displacement is equal to zero, and the law is called *extrinsic*. If K_0 takes low values, then the initial stress is equal to zero when there is no displacement and the law is called *intrinsic*.

- *Exponential law*

$$\sigma = \begin{cases} K_0\delta e^{-\delta/c_0} & \text{if } \delta \leqslant c_0, \\ \sigma_0[1+\beta(\delta-c_0)]e^{-\beta(\delta-c_0)} & \text{if } \delta \geqslant c_0, \end{cases} \tag{1.7}$$

with $c_0 = \frac{\sigma_0 e}{K_0}$ and β is calculated by making the dissipated energy equal to G_c.

- *Trapezoidal law*

$$\sigma = \begin{cases} K_0 \delta & \text{if } \delta \leqslant d_0, \\ \sigma_0 & \text{if } d_0 \leqslant \delta \leqslant d_1, \\ \frac{\sigma_0}{(d_2 - d_1)}(d_2 - \delta) & \text{if } d_1 \leqslant \delta \leqslant d_2, \\ 0 & \text{if } \delta \geqslant d_2, \end{cases} \tag{1.8}$$

where $d_0 = \frac{\sigma_0}{K_0}, d_1 = \frac{G_c}{\sigma_0}, d_2 = d_0 + d_1$.

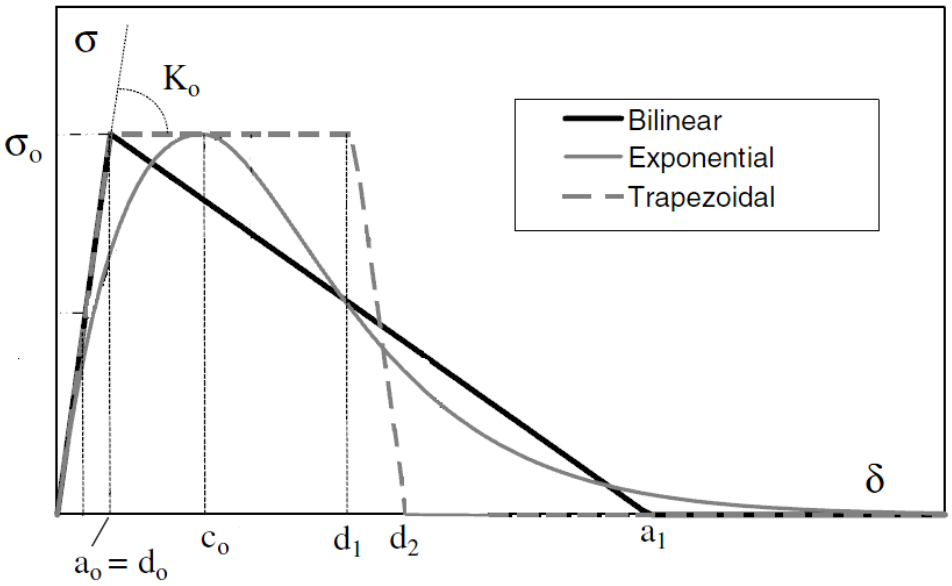

Figure 1.6. Cohesive law shapes: bilinear, exponential and trapezoidal

1.3 Experimental methods measuring cohesive laws

In order for the cohesive laws to be implemented in the Finite Element models, their parameters are needed to be measured first. Various experimental testing methods have been used to measure these parameters, depending on the mode type of cohesive law that needs to be measured. The parameters that are measured usually during the experiments are the fracture toughness denoted as G_c or J_c, the maximum stress σ_{max} and the maximum opening displacement δ_{max}. Next are presented experiment set-ups used to measure cohesive laws.

- *Mode I*

The most commonly used experiment set-up in order to measure Mode I cohesive laws is the Double Cantilever Beam (DCB) as seen in Figure 1.7. In [11], Ji G. et al. measured the Mode I cohesive laws of a bonded joint trying to provide data for the parameter calibrations in numerical models as also investigate the dependency between adhesive thickness and interface toughness. The adherends used were made from low carbon steel and the adhesive used was LOCTITE Hysol 9460, an epoxy adhesive. Six different adhesive thicknesses were used 0.09, 0.2, 0.4, 0.6, 0.8 and 1.0mm and the adherends had a constant thickness of about 6.35mm. The geometry of the specimens used is presented in the Table 1.2.

By using the J-integral theory an analytical solution (Equation (1.9)) for the energy release rate J was calculated and the interface normal stress was then calculated by differentiating with respect to the crack tip opening δ (Equation (1.10)).

$$J = \frac{(Pa)^2}{D} + P\theta_0 \tag{1.9}$$

$$\sigma(\delta) = \frac{\partial J}{\partial \delta} \tag{1.10}$$

P is the global peel load, D is the adherend's bending stiffness, θ_0 is the relative rotation between the upper and lower adherend at the the crack tip. So the derivation of the cohesive law can be made if the load P and rotation θ_0 are measured.

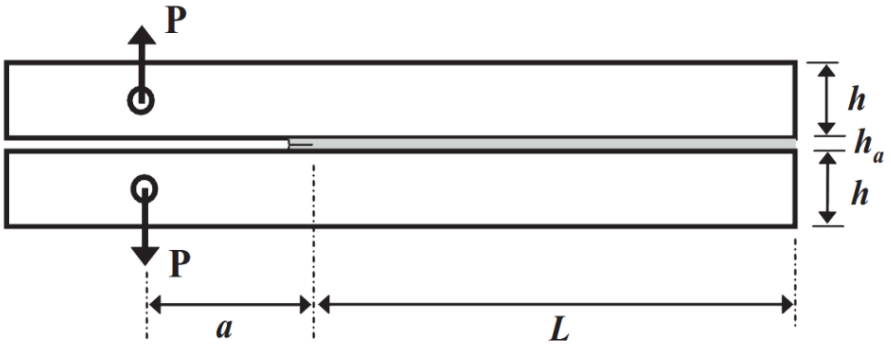

Figure 1.7. DCB test specimen.

Table 1.2. Geometry of specimens used in [11].

Group number	Average adhesive thickness (mm)	Length (mm)	Height (mm)	Width (mm)	Initial crack length (mm)
1	0.09	254.10	6.35	25.41	52.12
2	0.2	254.11	6.35	25.44	52.22
3	0.4	254.09	6.34	25.42	52.18
4	0.6	254.08	6.35	25.39	52.44
5	0.8	254.10	6.36	25.46	52.37
6	1.0	254.08	6.35	25.37	52.11

In Figure 1.8 a typical relationship between displacement of the DCB specimens at the loadline Δ and peel force P is presented, followed by Figure 1.9 where the J-integral versus the displacement is presented. The load and the rotation angle were measured during the experiments so the energy release rate was calculated.

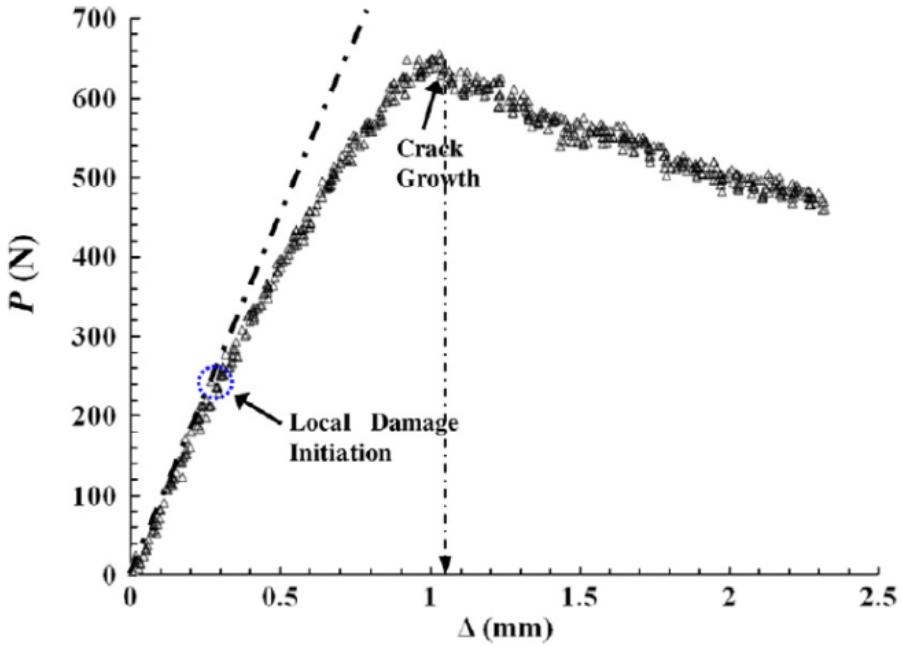

Figure 1.8. Typical displacement versus load in [11].

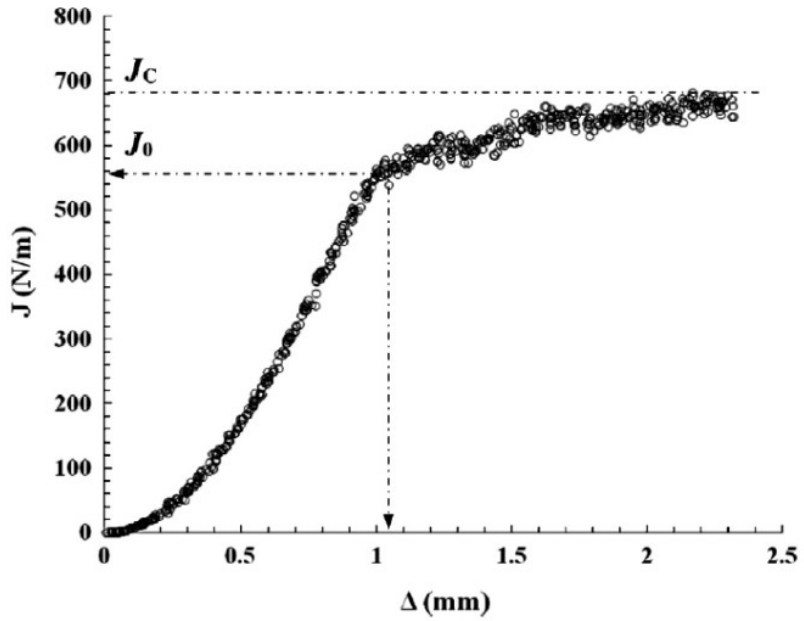

Figure 1.9. Typical displacement versus energy release rate in [11].

To obtain the cohesive law a differentiation was needed and the results taken are presented in Figure 1.10. It can be seen that the cohesive laws derived depended substantially on the adhesive layer thickness.

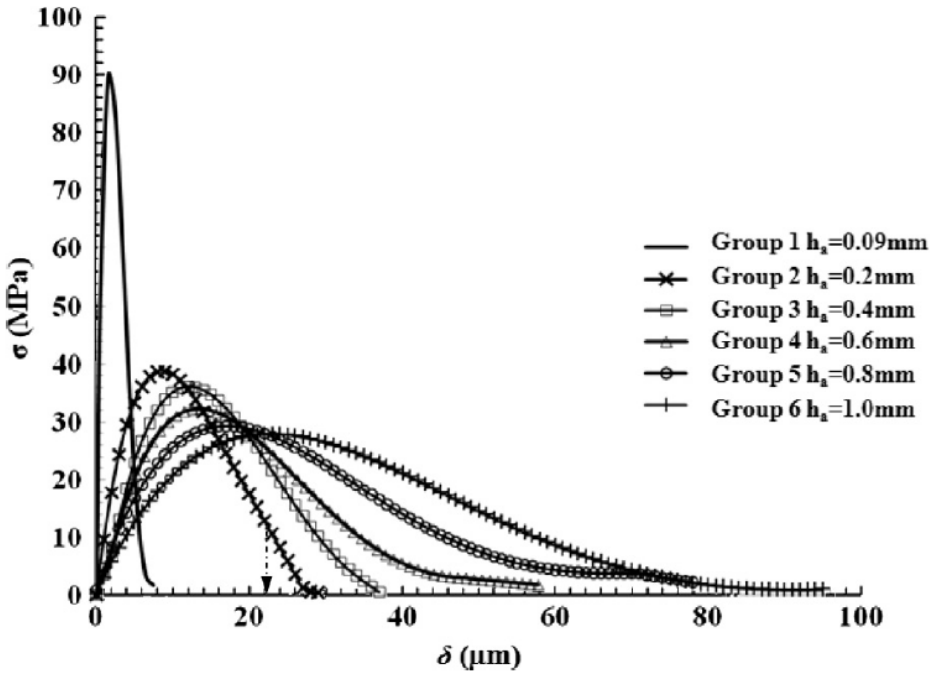

Figure 1.10. Cohesive laws derived with six different thicknesses of adhesive layer from [11].

The authors indicated that these results could be calibrated in numerical models to predict the behaviors of similar joints, but no study has been made so far on that. The maximum cohesive stress shown in Figure 1.10 had a range of values between 30 and 90MPa and the critical opening for which stress turns to zero had a range of values between 8 and 150μm.

In [12], Ouyang Zh. et al. used the same test configuration to obtain pure Mode-I cohesive laws, but also using dissimilar adherends (see Figure 1.11). They used the same procedure as [10] in order to obtain the energy release rate and then the cohesive law was also obtained by differentiation.

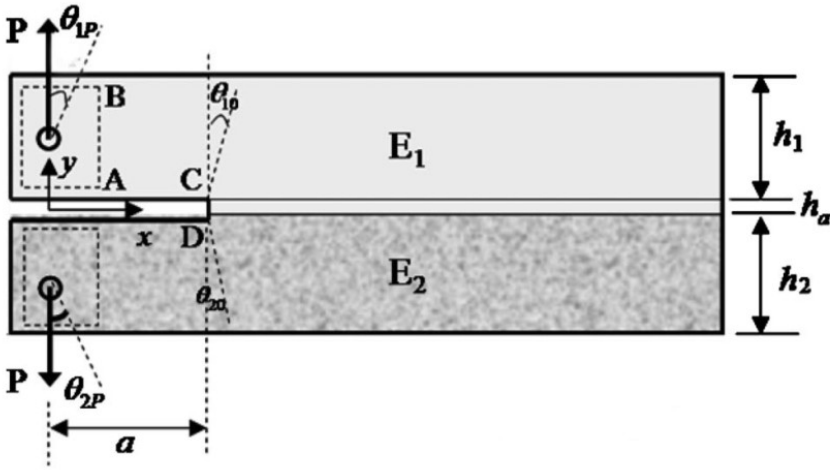

Figure 1.11. Dissimilar DCB specimen used in [12].

However, the problem they had to solve was how to achieve pure Mode-I loading in the dissimilar DCB specimen and avoid as much as possible the presence of shear stresses that will appear due to the asymmetry of the geometry. What they proposed is a decoupling condition under which the shear stresses vanish. After giving a theoretical demonstration of the feasibility of the idea, a comparison between numerical and experimental results was presented in order to evaluate the proposed method.

The decoupling condition proposed is written as:

$$\frac{h_1}{h_2} = \frac{D_1}{D_2} \tag{1.11}$$

where h_1 and h_2 are the beam thicknesses as seen in Fig.1.11 and D_1 and D_2 are the bending stiffness per unit width under plane strain conditions of material of beam 1 and 2 respectively.

Three different specimen groups were used, presented in Table 1.3.

Table 1.3 Materials and geometry of specimens used in [12].

(a) Material	Initial crack length (mm)	Width (mm)	Thickness h_1 (mm)	Thickness h_2 (mm)
Group 1 ($h_1/D_1=h_2/D_2$) (steel/aluminum)	52	25.4	6.04	10.53
Group 2 ($h_1=h_2$) (steel/aluminum)	52	25.4	6.04	6.04
Group 3 ($h_1=h_2$) (steel/steel)	52	25.4	6.04	6.04

(b) Material	Tensile modulus (GPa)	Tensile strength (MPa)
Adhesive	2.76	30.3
Steel	206.5	400
Aluminum	68.2	120

Group 1 is consisted by dissimilar DCB specimens complying with the decoupling condition mentioned before, Group 2 by dissimilar DCB specimens that don't comply with the condition and the adherends are of the same thickness and Group 3 is the standard symmetric DCB specimen.

From the experimental results from these groups it was shown that for Group 1, there is actually very small crack tip tangential slip opening (see Figure 1.12) compared to the normal opening (less than 1%). Group 2 that didn't comply with the decoupling condition presented a much higher crack tip tangential slip opening, more than 20%.

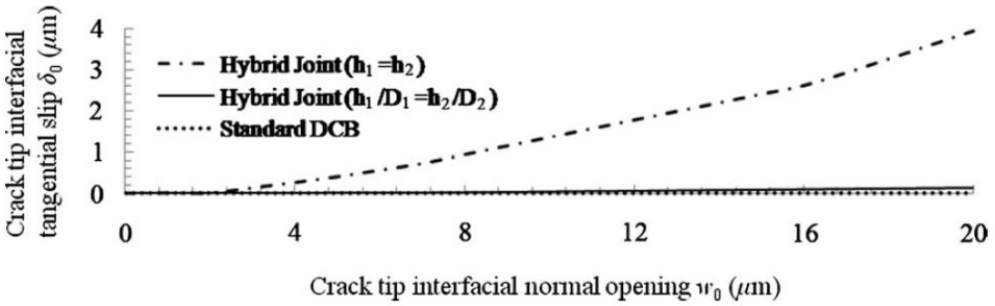

Figure 1.12. Tangential opening versus normal opening for the three different groups of [12].

The authors indicate that the remarkable difference between Groups 1 and 2 concerning the tangential opening gives experimental evidence that the proposed

method can nearly eliminate the Mode II effects of the dissimilar specimen and be treated as a pure Mode I experiment.

The Mode I cohesive laws could then be derived through the calculation of the energy release rate based on the J-integral. Typical results for Groups 1 and 3 (the Groups that were tested under Mode I) are shown in Figure 1.13.

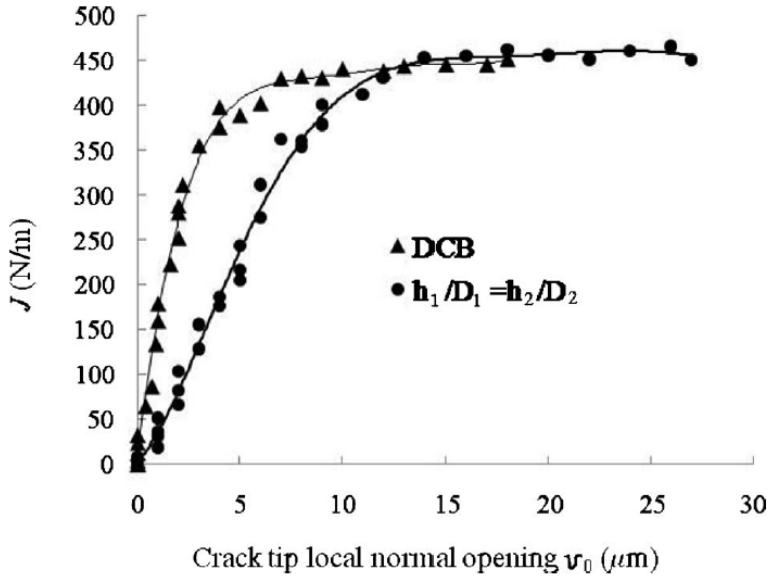

Figure 1.13. Energy release rate versus normal opening for Groups 1 and 3.

By differentiating the traction-separation law is obtained and typical results are presented in Figure 1.14. It should be noted that although the fracture toughness of the two Groups is about the same for the two Groups, around 450 N/m, the maximum cohesive stress for Group 3 is much higher: $\sigma_{max} \approx 100$MPa for Group 3 while $\sigma_{max} \approx 55$MPa for Group 1. This reduction could be explained by the different constraints from the dissimilar materials and extensive experimental characterizations are proposed for various bimaterial interfaces.

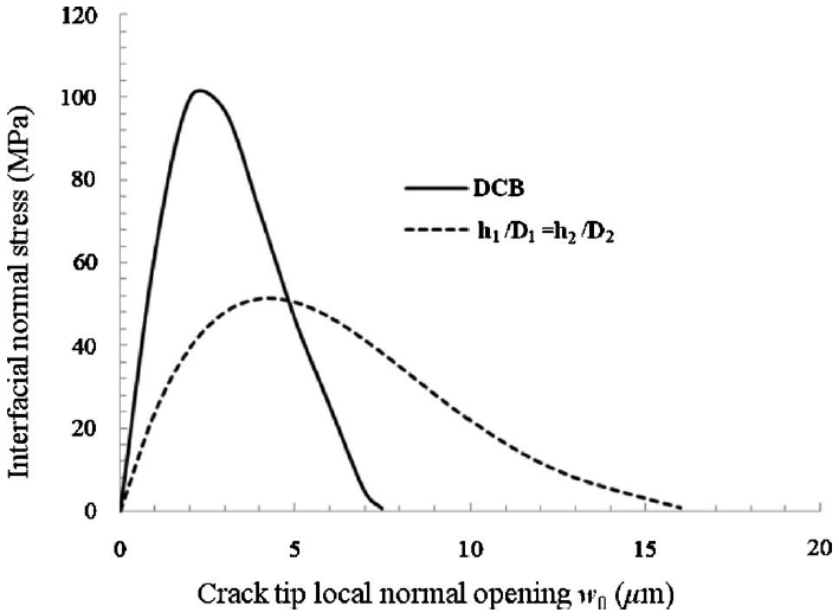

Figure 1.14. Cohesive law obtained for the Groups 1 and 3.

- *Mode II*

To measure the Mode II cohesive laws different experiment set-ups have been used with the most common being the End-Notched Flexure (ENF), introduced by Russell in 1982 [13]. Leffler et al. [14] later used this set-up to investigate the shear behavior of adhesive layers. The geometry of the specimen is presented in Figure 1.15

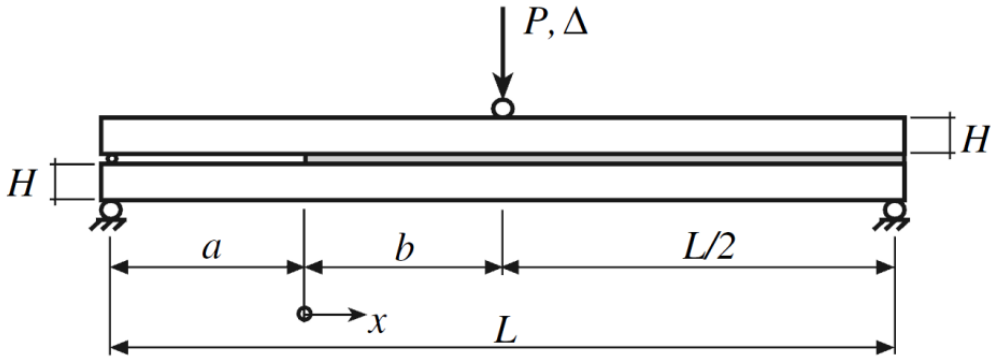

Figure 1.15. End-Notch Flexure (ENF) specimen.

An analytical equation is presented calculating the energy release rate which takes into account the influence of a flexible adhesive layer. The material used for the

adherends was steel and the adhesive type was DOW Betamate XW1044-3, an epoxy adhesive. The dimensions used for the specimens are presented in Table 1.4.

Table 1.4 Dimensions of specimens used in [14].

Specimen	L (m)	a (m)	H (mm)	W (mm)
A	1.00	0.20	32	32
B, N–O	1.00	0.35	32	32
C–D, K–M	1.00	0.35	25	32
E–J	1.00	0.35	16	32

The expression for the energy release rate used is:

$$J \approx \frac{9}{16}\frac{P^2a^2}{EW^2H^3} + \frac{3}{8}\frac{Pv_0}{WH} \tag{1.12}$$

where the dimensions L, α and H are seen in Figure 1.15, W is the width of the specimen, P is the load applied and u_0 is the shear deformation of the adhesive layer at the crack tip. So, for the evaluation of the energy release rate the applied load and the shear deformation were measured throughout the experiments.

Later, by using the experimentally measured energy release rate, the shear traction was calculated by differentiation. However, due to the scatter observed in the results, an approximation was done first of the J-u_0 curve with a Prony-series in order to minimize the scatter. In Figure 1.16 a typical energy release rate versus shear deformation is presented and in Figure 1.17 the resulting energy release rate versus shear traction.

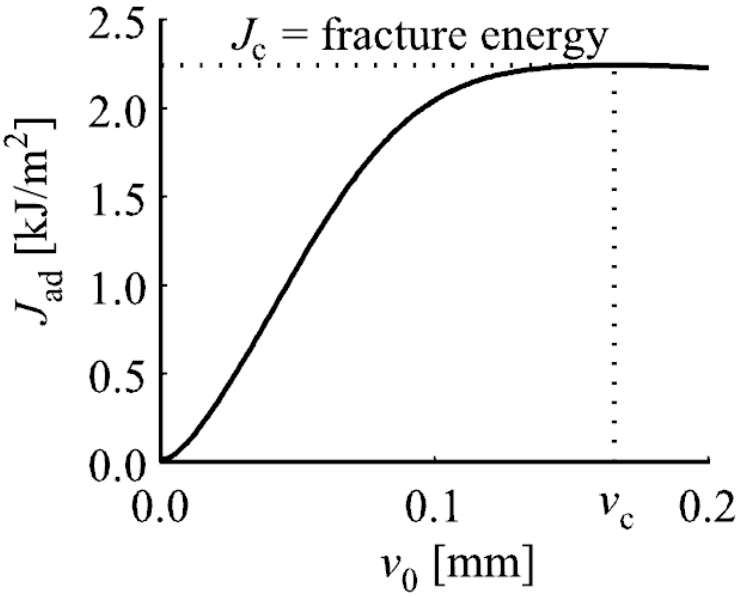

Figure 1.16. Typical curve of energy release rate versus shear deformation at the crack tip at [14].

The experiments were done with either a constant deflection rate or a constant shear deformation rate. The energy release rate calculated had a range of values between the 2.1 to 3.5MPa with higher values for the constant deflection rate tests.

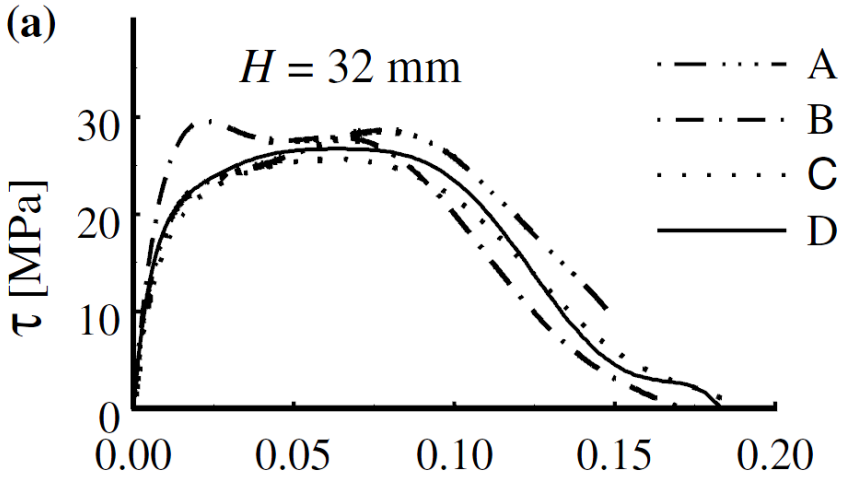

Figure 1.17. Typical Mode-II traction-separation law measured in [14].

Another experiment set-up is also used in literature for the determination of Mode II fracture toughness called End Loaded Split (ELS) which then can lead to the calculation of the Mode II cohesive law. The experiment set-up is seen in Figure 1.18.

In [15] ELS tests are used to measure the Mode II energy release rate of Pinus Pinaster wood. The equation used was based on the compliance calibration method:

$$G_{IIc} = \frac{9P^2}{4B^2h^3E_1}\left[(C - C_0)\frac{2Bh^3E_1}{3} + a_0^3\right]^{2/3} \tag{1.13}$$

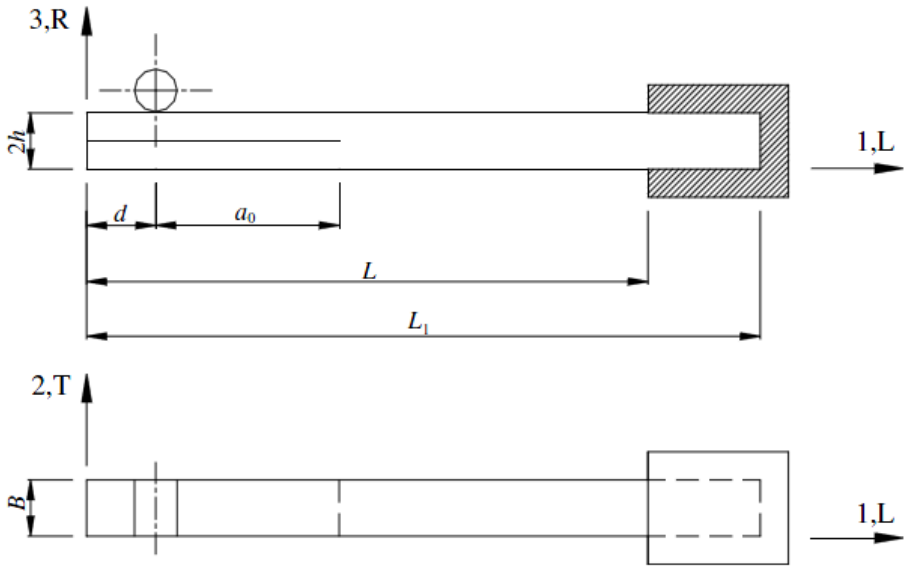

Figure 1.18. End Loaded Split set-up.

where α_0, B, h and L are the dimensions shown in Figure 1.18, C is the compliance which depends on the displacement and C_0 the initial compliance, E_1 the longitudinal Young's modulus and P is the applied load. This equation is useful since it depends only on the applied load and displacement during crack propagation and not on the crack length.

Results from the energy release rate are presented in Figure 1.19. The experimental results were then individually simulated with Finite Element analysis based on a cohesive damage model in order to numerically validate the proposed method. Excellent agreement was obtained between simulation and experimental results confirming the validity of the method.

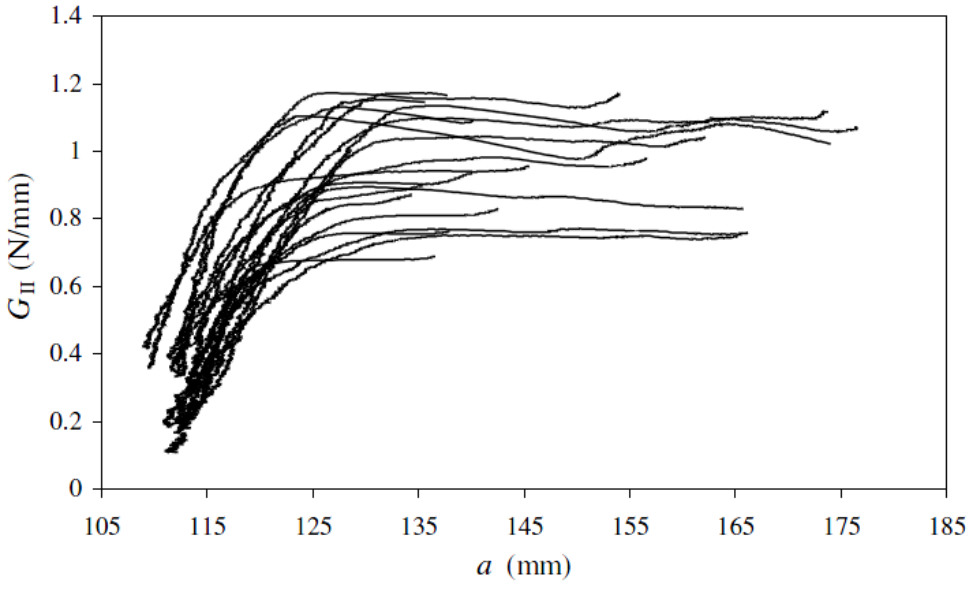

Figure 1.19. Energy release rate versus crack length from ELS tests in [15].

- *Mixed Mode*

For the measurement of mixed mode cohesive laws also different experimental set-ups have been used. Efforts have been made to find a test set-up that will allow testing under the full range of mode-mixities, which means from pure Mode I to pure Mode II, with just one type of specimen geometry.

One of the most used experiment set-ups is the Mixed Mode Bending (MMB) introduced by Reeder and Crews providing an easy variation of the mode ratio by just altering the lever length of the loading lever c (see Figure 1.20). This set-up is used in [16] in order to test Maritime pine wood. Specimen dimensions shown in Figure 1.20 are 2h=20mm, L=230mm, L_1=250mm, α_o=162mm and B=20mm.

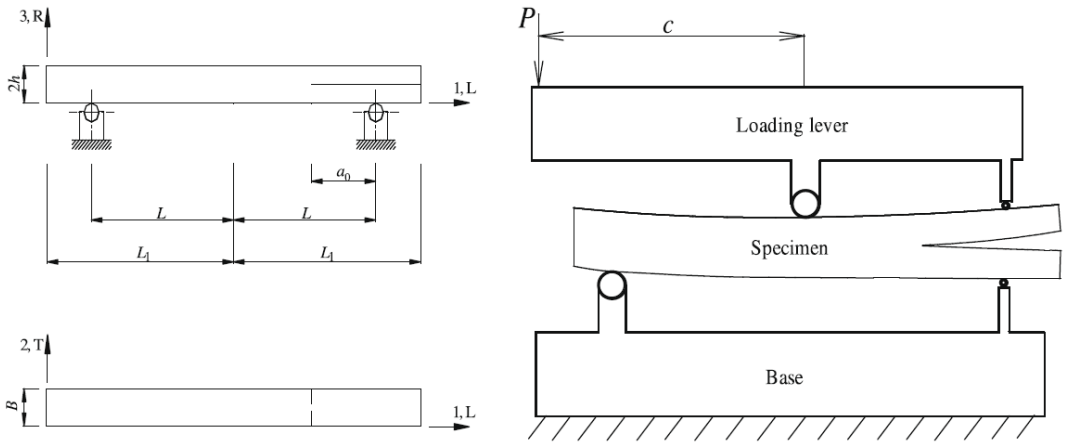

Figure 1.20. Mixed Mode Bending specimen's geometry and loading conditions.

The MMB test can be considered as a superposition of the DCB and the ENF tests mentioned before used for the fracture characterization of pure Mode I and pure Mode II respectively. The energy release rates can be calculated using the compliance method yielding for the Mode I component of the energy release rate:

$$G_{\mathrm{I}} = \frac{6P_{\mathrm{I}}^2}{B^2 h}\left(\frac{2a_{\mathrm{eqI}}^2}{h^2 E_{\mathrm{fl}}} + \frac{1}{5G_{\mathrm{LR}}}\right) \tag{1.14}$$

where the dimensions B and h are shown in Figure 1.20, P is the applied load, G_{LR} is the shear modulus, α_{eql} is the equivalent crack length estimated using the current specimen compliance and E_{fl} is the corrected flexural modulus, all independent of the actual crack length. Following a similar procedure the energy release rate for pure Mode II equation is obtained:

$$G_{\mathrm{II}} = \frac{9P_{\mathrm{II}}^2 a_{\mathrm{eqII}}^2}{16E_{\mathrm{fII}}B^2 h^3} \tag{1.15}$$

As it can be seen, Equations (1.14) and (1.15) are both independent of the crack length, so there is no need to monitor the crack length; only the applied load and the displacement need to be measured in order to obtain the energy release rates. Typical results from the experiments are shown in Figure 1.21 for a mode ratio of $G_I/G_{II}=0.5$.

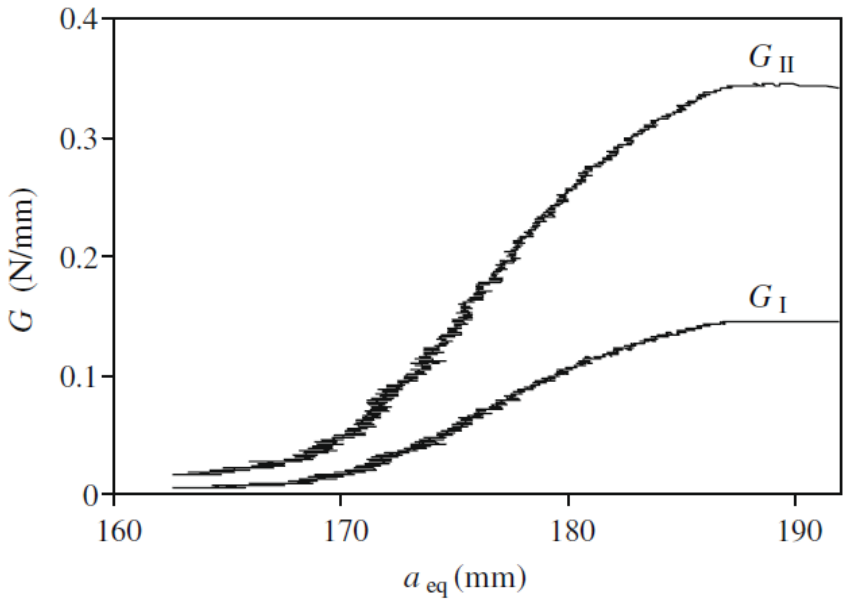

Figure 1.21. Energy release rates versus equivalent crack length for mode ratio of 0.5 measured in [16].

The authors then proceeded to a numerical analysis using cohesive elements for the verification of the proposed method. The input data for the cohesive zone model used were the elastic properties of the material and the average fracture energies in pure modes obtained from the experiments. The comparison between the numerical and experimental results can be seen in Figure 1.22.

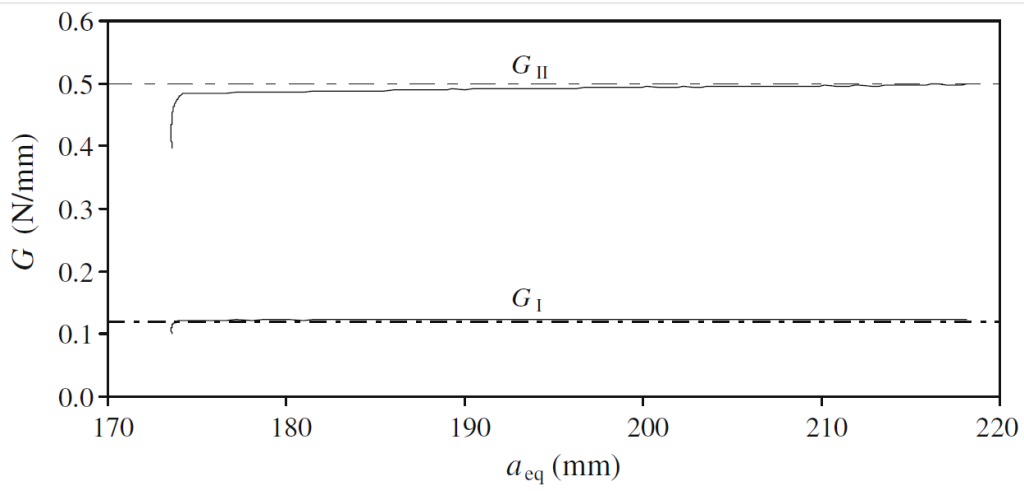

Figure 1.22. Comparison between the numerically measured energy release rate (solid lines) and the experimental values (dashed lines).

As it can be seen, the plateau values of the numerical curves present excellent agreement with the average strain energy release rates measured from the experiments, confirming once again the validity of the cohesive zone models.

Apart from the MMB specimen, other configurations have been also used. One promising one is presented in [17], where Choupani used modified Arcan specimens. This test set-up is consisted of various combinations of adhesive, composite and metallic adherends with a special loading fixture, in which by altering the loading angle a full range mode mixity loading is achieved. Choupani was able to obtain Mode I, Mode II and mixed mode fracture data and perform numerical analyses of the experiments. His main goal was to measure the fracture toughness K_{Ic} and K_{IIc}. The experiment set-up and the geometry of the specimen used is shown in the following Figure 1.20.

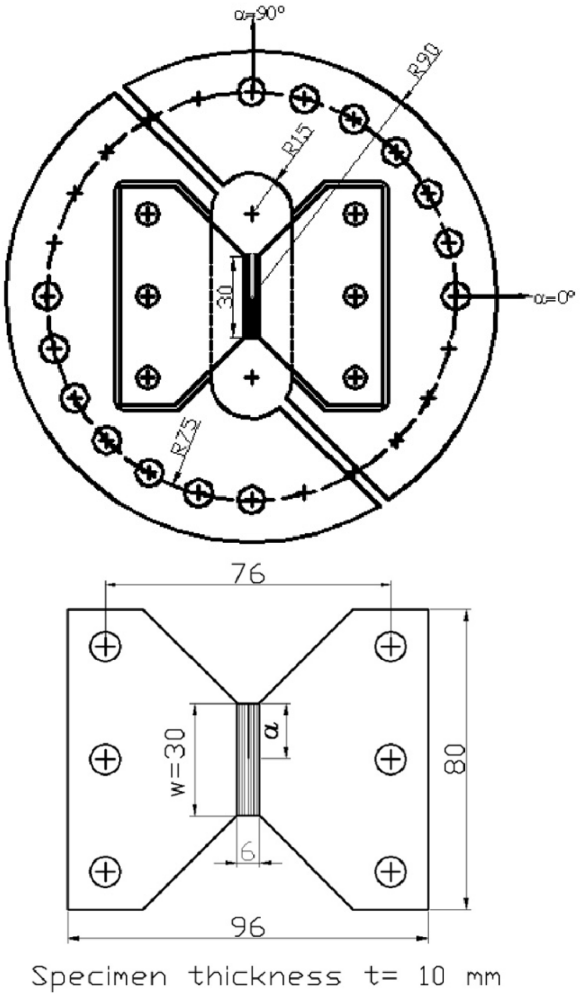

Figure 1.23. Up:The experimental set-up used in [17], Down: Geometry of the modified Arcan specimen.

The specimens were pinned into the loading device in order to transmit the applied loads. By applying a load P and by varying the loading angle α from 0^o to 90^o, pure Mode I to pure Mode II loading conditions are achieved.

The stress intensity factors ahead of the crack tip were measured by generalizing an equation of the stress intensity factor given by ASTM standards for plane strain Mode I loading. The equations that were used:

$$K_I = \frac{P_c\sqrt{\pi a}}{wt}\cos\alpha f_I(a/w)$$
$$K_{II} = \frac{P_c\sqrt{\pi a}}{wt}\sin\alpha f_{II}(a/w) \quad (1.16)$$

where P_c is the critical load, α is the loading angle, w is the specimen length, t is the specimen thickness and α is the crack length. The factors f_I(a-w) and f_{II}(a-w) are geometrical factors that were calculated using finite element analysis.

Energy release rates can then be calculated during the experiment by using the following equations:

$$G_I = K_I^2/\bar{E}$$
$$G_{II} = K_{II}^2/\bar{E} \quad (1.17)$$

The adhesive and bonded joint systems investigated in this study were chosen based on their anticipated usage on aerospace applications. Fracture tests were performed for Mode I, Mode II and five mixed-mode conditions. The average values of critical fracture loads were used to determine the critical mixed-mode stress intensity factors and strain energy release rates data using equations (14) and (15) respectively. Table 1.5 summarizes the mean values of experimentally determined critical strain energy release rates $(G_I)_c$, $(G_{II})_c$ and $(G_T)_c = (G_I)_c + (G_{II})_c$.

Table 1.5 Averaged critical strain energy release rates for different adherends with crack length 15mm and adhesive thickness 0.4mm.

Loading angle		0°	15°	30°	45°	60°	75°	90°
CF/PEI	$(G_I)_C$	153.2	149.6	151	137.3	126.3	62.2	–
	$(G_{II})_C$	–	1.8	8.6	23.5	65	148.9	235.3
	$(G_T)_C$	153.2	151.5	159.7	160.8	191.2	211.1	235.3
Aluminum	$(G_I)_C$	210.7	201.3	178.5	155	135.5	79.5	–
	$(G_{II})_C$	–	3.8	15.6	40.5	106.6	292.3	552.1
	$(G_T)_C$	210.7	205.1	194.1	195.5	242	371.8	552.1
Steel	$(G_I)_C$	80.4	78.1	75.9	71	53.8	32.8	–
	$(G_{II})_C$	–	1.7	7.6	21.3	48.6	139.4	279.1
	$(G_T)_C$	80.4	79.8	83.5	92.3	102.4	172.3	279.1

Observing the results obtained, the relationship between Mode I, Mode II and mixed-mode fracture toughness of all the adherends used is: $(G_I)_c < (G_{mixedT})_c < (G_{II})_c$. However, in order to choose the toughest system would be difficult since the material combinations responded differently in terms of Mode I, Mode II and mixed-mode.

It can be seen now, that many methods are proposed in literature for the fracture toughness characterization of adhesive joints.

1.4 The DCB-UBM specimen

All of the aforementioned experiment set-ups that have been used in literature for fracture characterization have their advantages and disadvantages and it is up to each researcher to choose which test fits the most to his needs. However, there are some main characteristics that an experiment set-up should present in order to make it attractive. An experiment set-up should not be limited to only a specific mode ratio, such as the ENF or the DCB specimens; enabling tests under the full range of mode mixity, from Mode I to Mode II is a very important characteristic. Furthermore, another very important feature of the test is to allow stable crack growth for all the mode mixities. For example, the MMB and the ENF tests may present unstable crack growth as it has been observed in [18], which leads to problems obtaining valid results from these tests. Another drawback which is present in any Mode II test where a transverse force is transmitted between the crack faces is the possible friction between the two separating faces. The friction coefficient can reach high values, increasing the toughness of the interface and thus making it difficult to calculate its contribution to the total fracture toughness.

In this study the specimen geometry used is called Double Cantilever Beam under Uneven Bending Moments (DCB-UBM). The test configuration is shown in Figure 1.24.

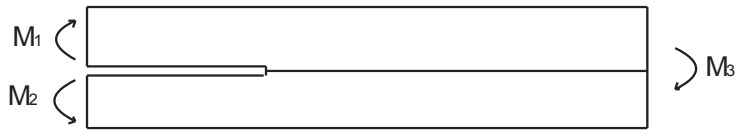

Figure 1.24. The Double Cantilever Beam specimen loaded with uneven bending moments

This test configuration presents the advantages that were mentioned above along with other interesting characteristics that are useful for the experiments that are to be made for this project. Firstly, the energy release rate can be calculated analytically as it will be shown later in Chapter 2 with no need to measure the crack propagation. Moreover, since the specimen is loaded with pure moments there are no transverse forces transmitted, reducing significantly this way any friction between the opening faces. The same specimen geometry can be used for all the range of mode mixities, so that there are no errors associated with differences in the process.

The fracture of an adhesive joint between steel and a carbon fiber reinforced plastic (CFRP) laminate using the DCB-UBM specimen geometry is studied in this thesis. In the next chapter, the design of the experiment is presented: the geometry of the specimens, the materials used, their manufacturing process and the test procedure is explained. Experiments will be performed for three different mode ratios using one specimen geometry. In the following chapter, the data obtained from the experiments are presented followed by their analysis which will lead to the extraction of the

cohesive laws of the steel-CFRP interface. The energy release rate is calculated first based on the results and then the tractions are obtained by differentiation as was done in literature mentioned before in this Chapter. A numerical implementation of the obtained cohesive laws will also be made in Chapter 4 in order to verify the procedure. The experiment set-up will be simulated and the cohesive laws will be inserted in the model using the ANSYS program. The results from the simulation will be compared to the experimental results for the verification of the proposed method. Finally, in the last chapter the conclusions from this work are presented.

2. EXPERIMENTAL PROGRAM

2.1 Specimen Geometry

The main goal of this study is to measure the Mode I and Mode II cohesive laws of a steel-CFRP adhesive joint using a ductile adhesive. So, a specimen geometry has to be designed that will enable the derivation of these laws through an experimental procedure. As it has been mentioned in the previous chapter, the double cantilever beam loaded with uneven bending moments specimen geometry is chosen for this purpose since the benefits it offers compared to other methods are important.

The materials and their dimensions were chosen based on their possible application in the marine industry. It is more often recently for composite materials to be used on repairs of marine steel structures. It can be seen in literature that composite patches have been used as a repair solution of damaged oil platforms and vessels, offering advantages over conventional methods (see [19]). In this study carbon fiber reinforced plastic (CFRP) was used for repairing a fatigue crack on a type 21 Frigate and it was proven as an excellent choice, as it was shown that the repair can last more than 10 years in service.

So, a unidirectional CFRP was chosen as the material to be studied in this report, joined adhesively with mild steel. Araldite 2015 was the adhesive chosen; it is a ductile tough adhesive as it can be extracted from [20]. It is suitable for bonding dissimilar substrates, presenting low shrinkage and high shear and peel strength.

The geometry of the DCB-UBM specimen that was chosen can be seen in Figure 2.1. The dimensions mentioned can be seen in Table 2.1.

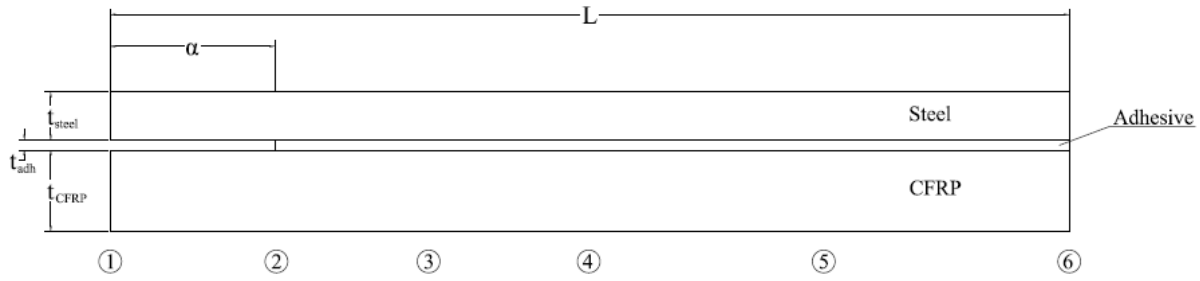

Figure 2.1. DCB-UBM specimen geometry used for this study. Numbers in circles present the thickness measuring positions shown in Tables 2.5-2.7.

Table 2.1. Dimensions chosen for the DCB-UBM specimen to be tested as seen in Figure 2.1.

t_{CFRP} (mm)	t_{steel} (mm)	t_{adh} (mm)	L (mm)	α (mm)	w (mm)
9.5	5	0.9	420	60	30

The length L of the specimen of 420mm was chosen as the longest possible, with the restriction of the dimensions of the oven that would be used later for the

curing of the adhesive. A long specimen presents the advantage that a longer crack extension can be achieved and thus the fully developed fracture process zone will be clearer than a shorter specimen. The pre-crack length α at 60mm was achieved with the insertion of a Teflon sheet and the width w of the specimens at 30mm were chosen based on previous DCB-UBM tests that were performed on the test rig that will be used for this project also. The thicknesses of the materials were chosen based on the fact that the sizes used are commonly encountered in marine applications.

2.2 Manufacturing of the specimens-Materials

- *Carbon Fiber Reinforced Plastic*

Two plates of unidirectional CFRP were made to be adhesively joined later with steel plates. The method used to fabricate the composite plates is the vacuum bagging technique, an inexpensive and efficient method for fabrication of composites. The manufacturing of the specimens was performed at the Shipbuilding Technology Laboratory at the National Technical University of Athens.

This technique is commonly used in composite materials because of the advantages it can offer compared to other methods, like the hand lay-up technique. An illustration of a cross section of a simple vacuum bag lay-up is shown in Figure 2.2.

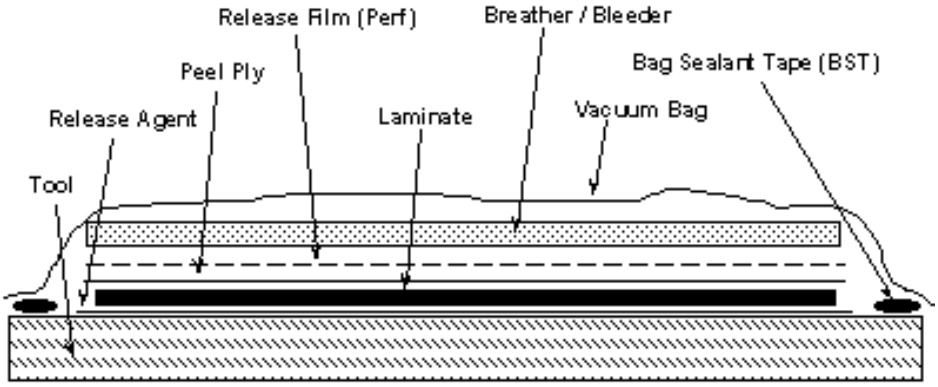

Figure 2.2. Cross section of a vacuum bag lay-up.

Figure 2.2 is explained below:

Release Agent: before the start of the laying-up, a release agent is applied on the tool (the surface on which the procedure is taking place). This is usually either a liquid release coating, such as wax, or a solid barrier such as a Teflon tape. Its purpose is to facilitate the release of the laminate after the procedure has finished.

Bag Sealant Tape: a dough-like material which comes in rolls with a release paper on one side, used for the airtight seal of the vacuum bag. This usually goes on after the part is laid-up.

Peel Ply: after the laminate is in place the first thing that is placed is the peel ply, a tightly woven fabric, often nylon, which is impregnated with a release agent. This sticks to the laminate but it can be pulled out without much difficulty and allows resin to seep through. Its common purpose is to give the laminate a rough instead of smooth finish.

Release Film: placed after the peel ply, it is a thin plastic film which will not bond to the laminate. It controls the resin flow during cure and it releases the vacuum consumable lay-up from the laminate after the cure is finished.

Breather/Bleeder: non-woven polyester breather/bleeder fabric is used to allow free passage of air across the bag while under vacuum pressure. This allows volatiles and air to be pulled out from the laminate and a uniform pressure to be applied on the surface. Excess resin is also absorbed from the fabric during cure.

Vacuum Bag: the last item to be placed. It is usually a nylon film due to the physical properties it presents that are needed for the procedure: high toughness along with good flexibility and high elongation. Vacuum bags must be completely airtight to ensure that no leaks will occur during the cure.

The uniform pressure that is achieved on the surface of the lay-up with this technique minimizes any voids in the buildup of the layers. Moreover, in the case where a breather-cloth is used during the procedure, any excess of resin is squeezed out achieving this way an optimum ratio of resin to carbon fiber.

In this project, uni-directional carbon fabric was chosen for the manufacture of the CFRP plates; 22 plies of the CST200 composite material textile were used. The ply thickness is 0.4mm and the textile presents a weight of 200gr/m^2. The resin used was the epoxy resin LH160 with hardener 135-136. The resin-hardener ratio was 35/100 respectively.

This technique was used for the fabrication of two CFRP plates with dimensions (485mm x 538mm) and an average thickness of 9.5mm. However, the thickness of the laminate was not constant throughout the length of the plate, presenting a significant variation. The plate presented its smallest thickness value of 7.5mm on its sides and it increased to about 10mm on the middle of the laminate. For this reason only a part was used for the fabrication of the specimens; this can be seen in the following Figure 2.3 as the shaded part of the plate along with the locations of the maximum (t_{max}) and minimum (t_{min}) thickness.

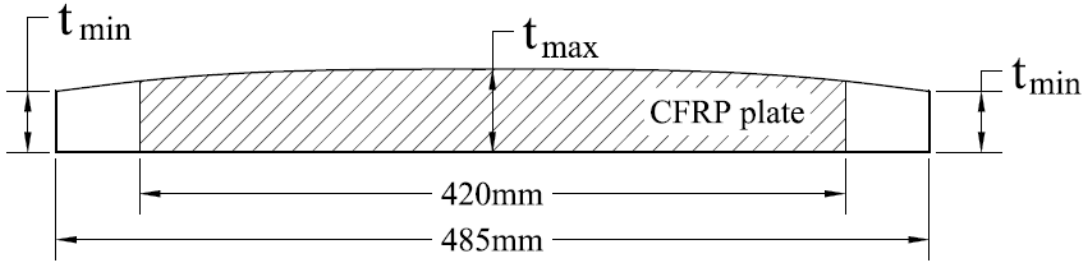

Figure 2.3. Cross section of the fabricated CFRP plate along with the part that was used for the fabrication of the specimens (shaded).

In the following Figure 2.4 the CFRP plate is shown during the curing procedure, inside the vacuum bag. A pressure of 0.6bar was applied throughout the curing of the plate.

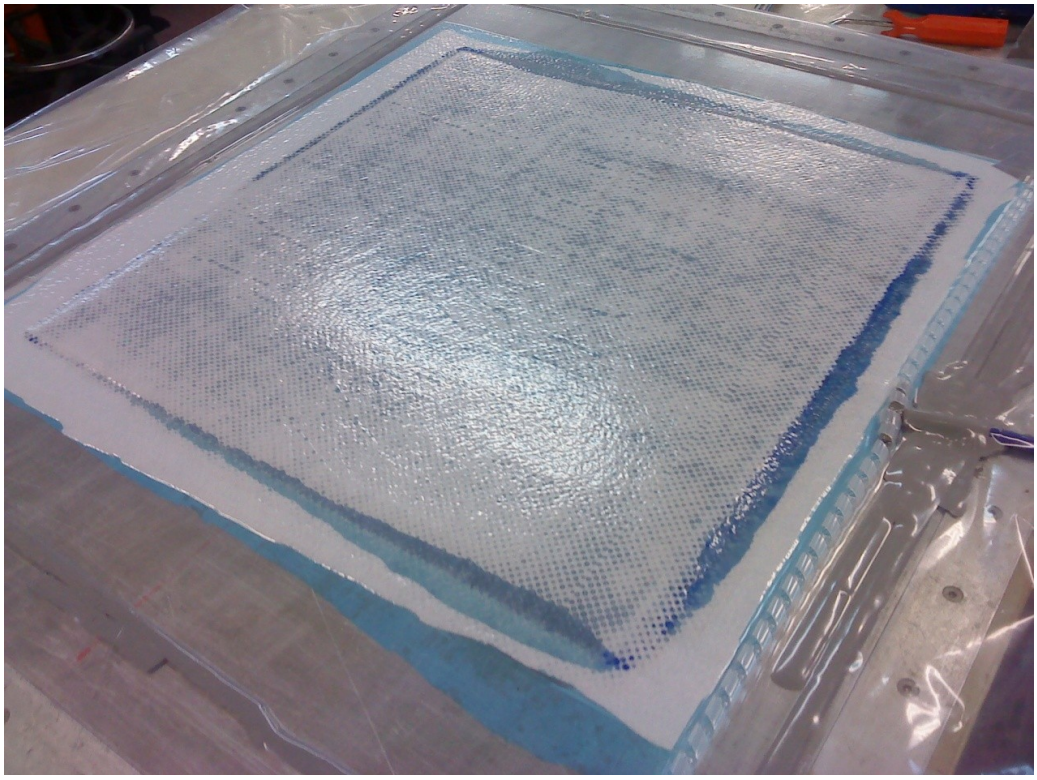

Figure 2.4. CFRP plate manufacturing with the vacuum bag lay-up procedure.

- *Steel*

The steel chosen as an adherend is mild steel, normal grade. Two 5mm thick plates with the same dimensions as the CFRP plates were ordered so that the two materials could be adhesively joined together.

- *Adhesive*

The adhesive chosen is the Araldite 2015. It is a thixotropic, two component, room temperature curing, toughened paste adhesive. It presents low shrinkage, it is gap filling, with no sagging up to 10mm thickness.

The physical properties of all the materials used are presented in the next table. They were evaluated through a finite element model simulation performed by Anyfantis K.

Table 2.2. Properties of the materials used in the project.

	Young's Modulus	Shear Modulus	Poisson's ratio
CFRP	E_1=35GPa	G_{12}=2GPa	v_{12}=0.35
	E_2=E_3=3GPa	G_{23}=G_{13}=1.5GPa	v_{23}=v_{13}=0.3
Steel	E=170GPa	G=65GPa	v=0.3
Adhesive	E=2GPa	G=0.9GPa	v=0.33

Before the adhesive bonding could take place, the surfaces of the materials had to be prepared. The steel plates were grit-blasted on the surface that was to be adhered in order to acquire a cleanness of SA 2 ½ (according to Norsok Standard M-501 'Surface Preparation and Protection Coating'). The surface roughness of the steel was measured with a TR100 Surface Roughness Tester. The arithmetical mean roughness R_a and the ten-point mean roughness R_z with cut-off length λ_1=0.25mm and λ_3=2.5mm were acquired. The average results are presented in Tables 2.3 and 2.4 for the two plates manufactured. It can be extracted that the second plate is a bit rougher than the first plate.

Table 2.3. Roughness measurements of the steel surface of the first plate.

λ_1=0.25mm		λ_3=2.5mm	
R_a(μm)	R_z(μm)	R_a(μm)	R_z(μm)
3.60	20.69	7.05	48.68

Table 2.4. Roughness measurements of the steel surface of the second plate.

λ_1=0.25mm		λ_3=2.5mm	
R_a(μm)	R_z(μm)	R_a(μm)	R_z(μm)
5.29	25.45	8.58	60.95

The surface of the CFRP was made rougher with the use of sandpaper in order to obtain better adhering properties. Then, the surfaces had to be cleaned from any traces of grease, oil and dirt that could reduce the quality of the bond. This was achieved by using acetone and Loctite 7063, a solvent cleaner on the surfaces. Finally, the two plates were ready to be adhesively joined: the Araldite adhesive was applied on the surfaces of the two materials along with spacers of 1mm to ensure the desired adhesive thickness. A sheet of Teflon was also placed in one end of the plates in order to act as a pre-crack. The plates were brought together and pressure was applied on both sides of the joint to ensure the bond. The joint was then inserted into an oven for the adhesive to cure at 60^{o}C for 1.5 hour. The joining procedure finished with a smooth cooling to ambient temperature.

After the plates have been bonded and the adhesive was cured, the specimens were cut from the plates with water-jet cutting. The part of the plates used for the fabrication of the specimens has been shown in Figure 2.3. A gap of at least 5mm was left between each specimen and a total of nineteen specimens were acquired with an average width of 30mm. However, four of the specimens had to be discarded due to the great variation they presented in their thickness resulting in a final of fifteen specimens that were used in the experiments.

As it has been mentioned before, the CFRP plate did not present a completely uniform thickness, so the thickness of the specimens was measured in various positions. The measurements are shown in the following Tables, where t_{tot} is the total thickness of the joint, t_{CFRP} is the thickness of the CFRP and t_{adh} is the thickness of the adhesive. Measurements refer to positions from 1 to 6 which are shown in Figure 2.1.

Table 2.5. Thickness measurements of the specimens for the Mode I tests.

MI-1				MI-2			
Position	t_{tot} (mm)	t_{CFRP}(mm)	t_{adh}(mm)	Position	t_{tot}(mm)	t_{CFRP}(mm)	t_{adh}(mm)
1	15.3	9.4	0.9	1	15.3	9.4	0.9
2	15.5	9.5	1.0	2	15.5	9.5	1.0
3	15.7	9.8	0.9	3	15.8	9.7	1.0
4	16.1	10.2	0.9	4	15.9	9.8	1.0
5	15.6	9.9	0.7	5	15.6	9.8	0.8
6	15.1	9.5	0.6	6	15.0	9.2	0.8
MI-3				**MI-4**			
Position	t_{tot} (mm)	t_{CFRP}(mm)	t_{adh}(mm)	Position	t_{tot}(mm)	t_{CFRP}(mm)	t_{adh}(mm)
1	15.3	9.3	1.0	1	15.3	9.3	1.0
2	15.3	9.2	1.1	2	15.7	9.7	1.0
3	15.6	9.5	1.1	3	16.0	9.9	1.1
4	15.6	9.5	1.1	4	16.2	10.0	1.2
5	15.3	9.3	1.0	5	15.7	9.7	1.0
6	15.1	9.1	1.0	6	14.6	9.0	0.6
MI-5				**MI-6**			
Position	t_{tot} (mm)	t_{CFRP}(mm)	t_{adh}(mm)	Position	t_{tot}(mm)	t_{CFRP}(mm)	t_{adh}(mm)
1	15.1	9.3	0.8	1	15.0	9.2	0.8
2	15.1	9.1	1.0	2	15.5	9.5	1.0
3	15.0	9.0	1.0	3	15.8	9.7	1.1
4	15.5	9.3	1.2	4	15.9	9.8	1.1
5	15.2	9.1	1.1	5	15.6	9.8	0.8
6	15.0	9.0	1.0	6	15.5	9.9	0.6

Table 2.6. Thickness measurements of the specimens for the mixed mode tests.

MM-1				MM-2			
Position	t_{tot} (mm)	t_{CFRP}(mm)	t_{adh}(mm)	Position	t_{tot}(mm)	t_{CFRP}(mm)	t_{adh}(mm)
1	14.5	8.8	0.7	1	14.5	8.5	1.0
2	14.5	8.8	0.7	2	14.5	8.5	1.0
3	15.0	9.0	1.0	3	14.0	8.2	0.8
4	14.8	8.9	0.9	4	13.8	8.0	0.8
5	14.6	8.8	0.8	5	14.0	8.2	0.8
6	14.3	8.8	0.5	6	14.3	8.3	1.0
MM-3				**MM-4**			
Position	t_{tot} (mm)	t_{CFRP}(mm)	t_{adh}(mm)	Position	t_{tot}(mm)	t_{CFRP}(mm)	t_{adh}(mm)
1	14.8	8.9	0.9	1	15.4	9.3	1.1
2	15.0	9.0	1.0	2	15.2	9.3	0.9
3	14.6	8.8	0.8	3	15.6	9.5	1.1
4	14.9	8.9	1.0	4	15.8	9.6	1.2
5	15.0	9.0	1.0	5	15.5	9.4	1.1
6	15.0	9.0	1.0	6	15.2	9.2	1.0

Table 2.7. Thickness measurements of the specimens for the Mode II tests.

MII-1				MII-2			
Position	t_{tot} (mm)	t_{CFRP}(mm)	t_{adh}(mm)	Position	t_{tot}(mm)	t_{CFRP}(mm)	t_{adh}(mm)
1	15.3	9.6	0.7	1	15.9	9.6	1.3
2	15.3	9.8	0.5	2	16.0	10.0	1.0
3	15.6	9.8	0.8	3	16.1	10.0	1.1
4	16.1	10.0	1.1	4	16.2	10.1	1.1
5	15.8	9.8	1.0	5	15.5	9.7	0.8
6	15.4	9.6	0.8	6	15.1	9.5	0.6
MII-3				**MII-4**			
Position	t_{tot} (mm)	t_{CFRP}(mm)	t_{adh}(mm)	Position	t_{tot}(mm)	t_{CFRP}(mm)	t_{adh}(mm)
1	14.7	8.9	0.8	1	15.4	9.4	1.0
2	14.5	8.8	0.7	2	15.4	9.3	1.1
3	14.3	8.6	0.7	3	15.7	9.5	1.2
4	13.9	8.2	0.7	4	16.0	9.7	1.3
5	14.2	8.3	0.9	5	15.7	9.5	1.2
6	14.3	8.5	0.8	6	15.2	9.2	1.0

MII-5			
Position	t_{tot} (mm)	t_{CFRP}(mm)	t_{adh}(mm)
1	15.0	9.3	0.7
2	15.0	9.3	0.7
3	15.3	9.5	0.8
4	15.1	9.4	0.7
5	15.0	9.3	0.7
6	14.9	9.2	0.7

From the measurements listed above the mean values of the respective thicknesses can be extracted. In the following Table 2.8 the average dimension values of the manufactured specimens are presented as seen in 2.1.

Table 2.8. Average values of the dimensions seen in Figure 2.1 of the manufactured DCB-UBM specimens.

t_{CFRP}(mm)	t_{steel}(mm)	t_{adh}(mm)	L(mm)	α(mm)	w(mm)
9.5	5	0.9	419	60	30

In Figure 2.5, a manufactured DCB-UBM specimen is presented. The Teflon sheet that was inserted to act as an initial crack can also be seen.

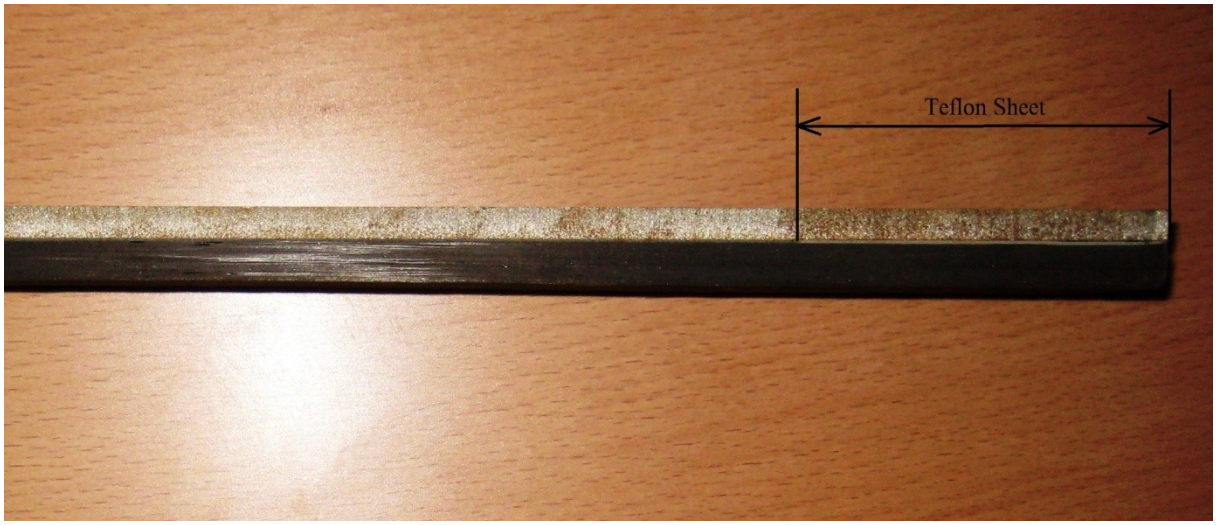

Figure 2.5. A DCB-UBM specimen that was tested in this study. The Teflon sheet used as the initial crack can be seen.

2.3 Test procedure

The test configuration is a double cantilever beam specimen loaded with uneven bending moments (DCB-UBM). The tests were carried out at the Risø National Laboratory for Sustainable Energy, Materials Research Division, Technical University of Denmark. A special fixture was used that can apply pure bending moments to the specimen by two transverse arms, using a wire/roller system at the cracked ends of the beams. A sketch of the set-up is shown in Figure 2.6. The lower beam is displaced downwards at a steady rate which causes the force in the wire to be increased. The moment applied at each beam of the DCB specimen can be controlled through the length of the transverse arms, l_1 and l_2 in the figure:

$$M_1=Pl_1, \qquad M_2=Pl_2 \tag{2.1}$$

where P is the force applied by the wire. So, by changing the lengths l_1 and l_2 different moment ratios M_1/M_2 can be obtained, enabling this way the same specimen geometry to be used for different mode mixities and eliminating the errors that could occur by changing the testing procedure in order to obtain different mode mixity. Moreover, since this set-up produces pure moments, the moment ratio throughout the length of the specimen is the same.

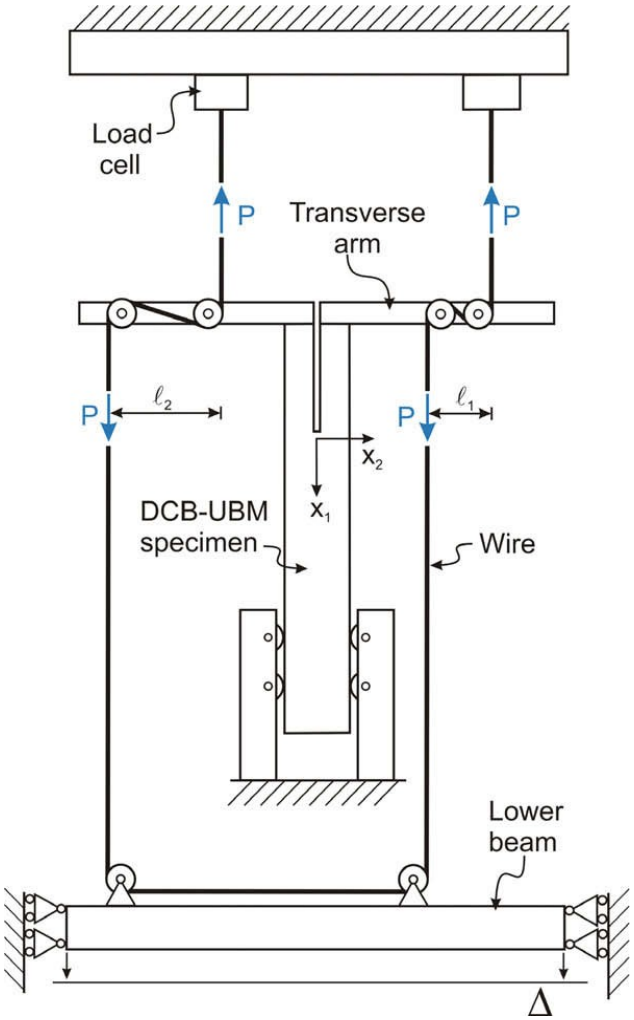

Figure 2.6. Overview of the test set-up (taken from [21]).

In order to mount the transverse beams (moment arms) to the specimens, aluminum parts had to be attached on the cracked ends of the specimens. Then a grip at the end of each transverse arm can be used to grab these aluminum parts.

For the mounting of the measuring devices the DCB specimens had to be mounted with pins. These pins were placed in the neutral axis of each part of the specimens at the end of the slip-foil. On one side of the specimen an extensometer was mounted to keep a record of the displacement between the pins. The extensometer used was an INSTRON 2620-602, with a range of $\pm$2.5mm. On the other side, two linear variable differential transformers (LVDTs) LDI 8/1 were mounted through a special set-up to keep a record of the tangential displacements at the neutral axis. These records were used later in order to obtain the normal and tangential opening at the pre-crack tip, using trigonometric equations.

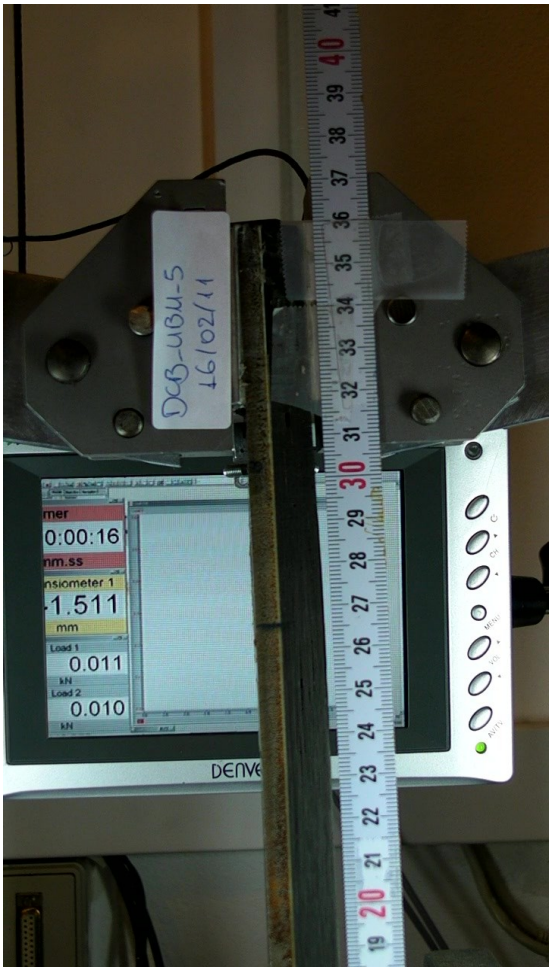

Figure 2.7. A DCB specimen under testing.

The specimens were loaded using a constant displacement rate of the lower beam at 5 or 10 mm/min. The data were recorded at a PC using a data acquisition program called DASYLab at 25 Hz.

The basic aim of the work was to measure the traction-separation laws under pure Mode I and pure Mode II and produce experimental data under a combined Mode I and Mode II loading. Three different loading cases were considered to achieve this: a Mode I configuration with a moment of CFRP to steel ratio equal to

$\frac{M_{CFRP}}{M_{Steel}} = +2$ (sign conventions can be seen in Figure 2.8), a mixed-mode configuration with $\frac{M_{CFRP}}{M_{Steel}} = -6$, and a Mode II dominant configuration with $\frac{M_{CFRP}}{M_{Steel}} = -3.4$. The above magnitudes were calculated from an initial FE analysis performed by Anyfantis K.. However, the magnitude calculated for the Mode II configuration did not achieve a pure Mode II test. This matter will be discussed later on. The moments were controlled through the change of the moment arms.

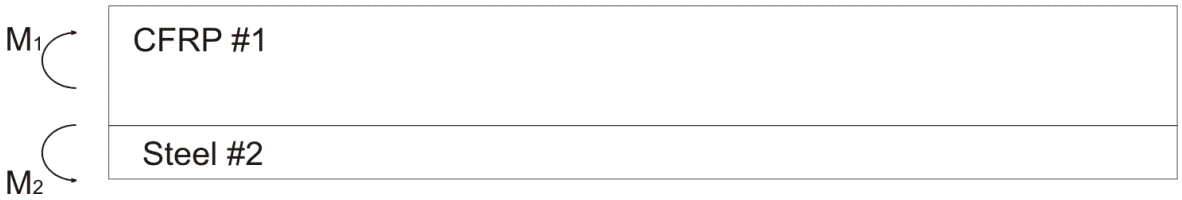

Figure 2.8. Moments are considered positive as above.

A total of 15 specimens were tested: six specimens under $\frac{M_{CFRP}}{M_{Steel}} = +2$, four specimens under $\frac{M_{CFRP}}{M_{Steel}} = -6$ and five specimens under $\frac{M_{CFRP}}{M_{Steel}} = -3.4$.

3. EXPERIMENTAL RESULTS

3.1. Data obtained from the experiments

During the experiments the load on the wire was measured directly. The normal and tangential displacements of the end-opening were determined from the data of the measuring devices (extensometer and LVDTs). The equations used are:

$$\delta_n = (\bar{d} + \Delta^{Ext})\sin\theta_5 - \bar{d}\cos\theta_4$$
$$\delta_t = (\bar{d} + \Delta^{Ext})\cos\theta_5 + \frac{d_2 - d_1}{2}\sin\theta_4 \qquad (3.1)$$

where all the dimensions used are known and they are all explained in Appendix A along with the procedure followed in order to obtain these equations.

The next graphs show the load (in kN) versus the displacements (in mm) for each specimen. For the moment ratio $\frac{M_{CFRP}}{M_{Steel}} = +2$, only normal opening is shown since the tests were very close to pure Mode I loading and no tangential opening was measured.

- For moment ratio $\frac{M_{CFRP}}{M_{Steel}} = +2$ the response of six specimens is presented in Figure 3.1. The moment arms used are l_1=+86.5mm for the steel beam and l_2=+176.5mm for the CFRP beam:

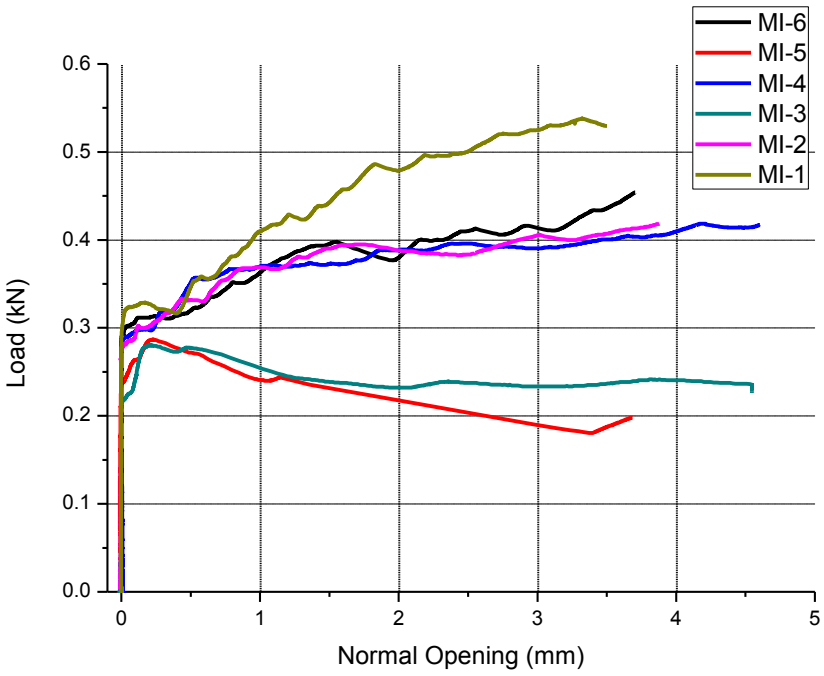

Figure 3.1. Load versus normal opening for MCFRP/MSteel=+2

As it can be seen, for most of the specimens, the load continued to increase even after the crack started to propagate. A possible explanation to this can be that the crack may start inside the adhesive layer, meaning that there is cohesive failure where a first plateau is reached for the load values. Then, the load starts to increase again as the crack moves to the interface between the adhesive-CFRP materials reaching a new steady value for the interfacial failure. Moreover, another explanation could be the slight increase of the thickness of the CFRP through the length of the specimens, which can cause a higher load to be needed to continue the crack propagation. Finally, the load increase could have been caused by the slight decrease of the adhesive thickness throughout the length of the specimens used; it has been shown in literature (e.g. [11]) that a decreasing adhesive layer thickness may increase the fracture toughness of the joint. No fiber bridging was observed, so this cannot be the case for the increase of the load. The unloading of the specimens followed a linear path which means that the two beams remained in the elasticity area.

The crack started to propagate for load values ranging from 0.22kN up to 0.32kN. For specimen MI-1 the substantial increase of the load after the end opening reached a value of 0.5mm can be explained by the crack moving into the CFRP beam leading to the delamination of the material. For specimens MI-3 and MI-5 the load drop is caused by a rapid crack growth leading to the unloading of the wire.

It can be seen that the results present some repeatability: data from specimens MI-2, MI-4 and MI-6 have an average percentage difference of $\pm$8%. All these specimens were cut from the second CFRP plate which means they were produced by the same manufacturing procedure. Specimen MI-1 was also made from the second plate, but the adhesive thickness of this specimen presented a significant decrease which may be the reason of the higher fracture toughness measured. The results from the other two specimens are again similar but lower than the rest of the specimens, a fact that can be possibly attributed to the differences coming from the manufacturing process of the specimens and that rapid crack growth was present.

In the following Figure 3.2 the fracture surface of two Mode I specimens is presented, showing that the crack propagated mainly through the CFRP-adhesive interface. However, the propagation of the crack could have been monitored more easily to move through a specific interface if a crack starter had been used during the manufacturing of the specimens.

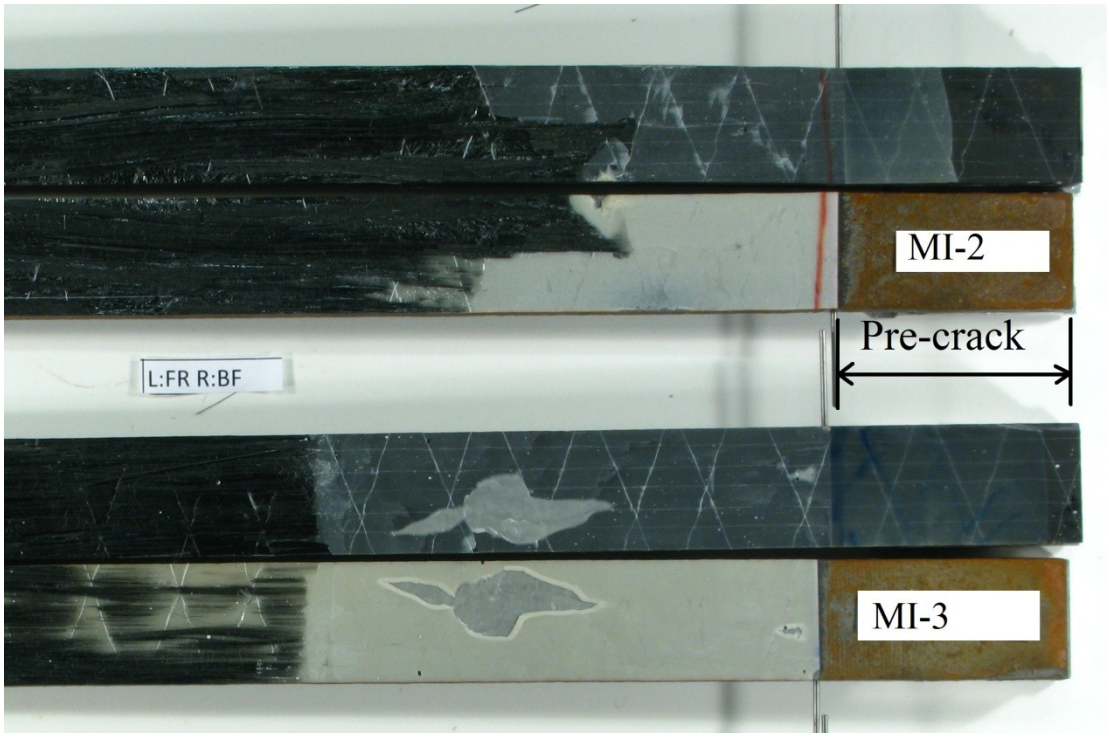

Figure 3.2. Fracture surface photo from MI-2 and MI-3 specimens showing the pre-crack and the crack propagation through the CFRP-adhesive interface.

- For moment ratio $\frac{M_{CFRP}}{M_{Steel}} = -6$, four specimens were tested. The moment arms used are l_1=-86.5mm for the steel beam and l_2=+519mm for the CFRP beam. In Figures 3.3-3.4, the results are concentrated for all four specimens:

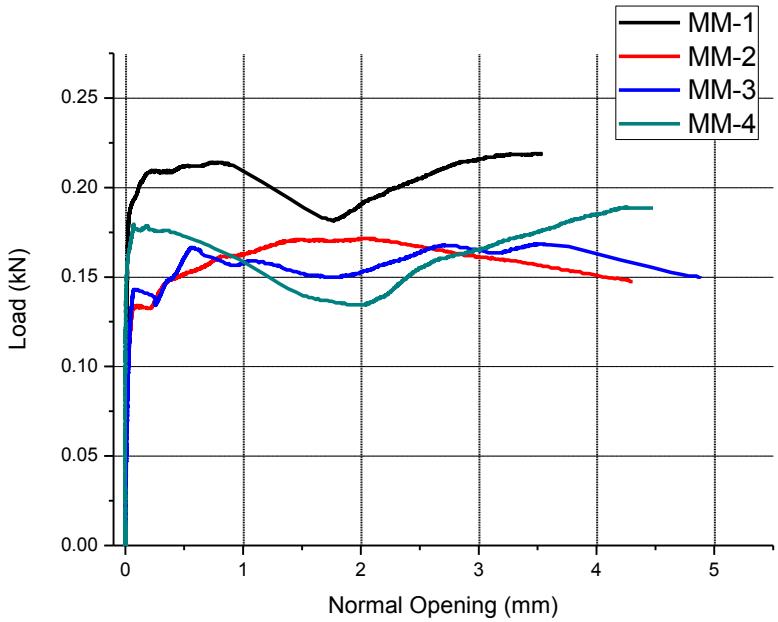

Figure 3.3. Load versus normal opening for MCFRP/MSteel=-6

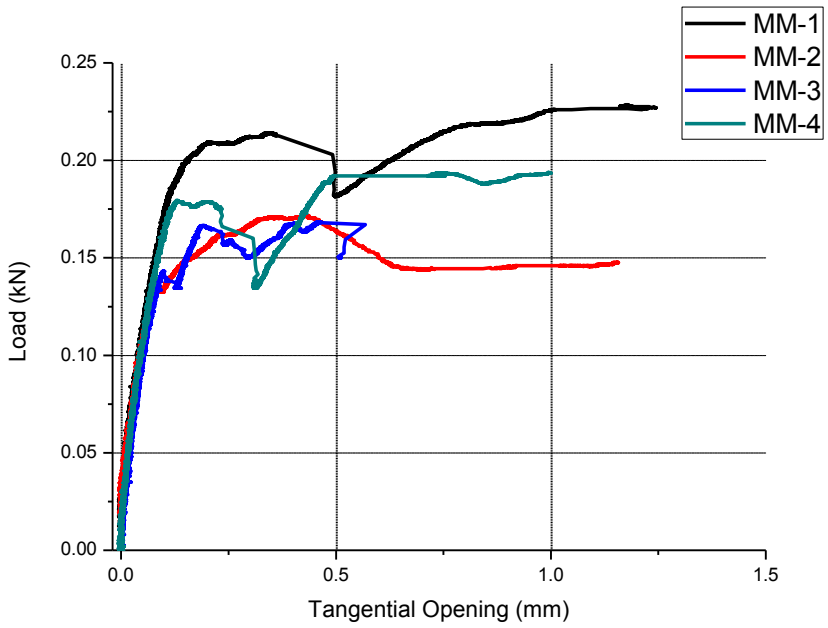

Figure 3.4. Load versus tangential opening for MCFRP/MSteel=-6

The crack propagated through the CFRP-adhesive interface at a load value ranging from 0.14kN up to 0.20kN, so the results don't present the repeatability wanted. Rapid crack growth was also observed here in all of the specimens resulting in a respective load drop.

Specimen MM-1 presents higher load values, while the rest of the specimens present values with less variation. The fact that specimen MM-1 was manufactured from the second CFRP plate can again be a cause of this difference presented in the fracture toughness between the specimens.

Figure 3.5 shows the normal opening versus the tangential opening for all four specimens:

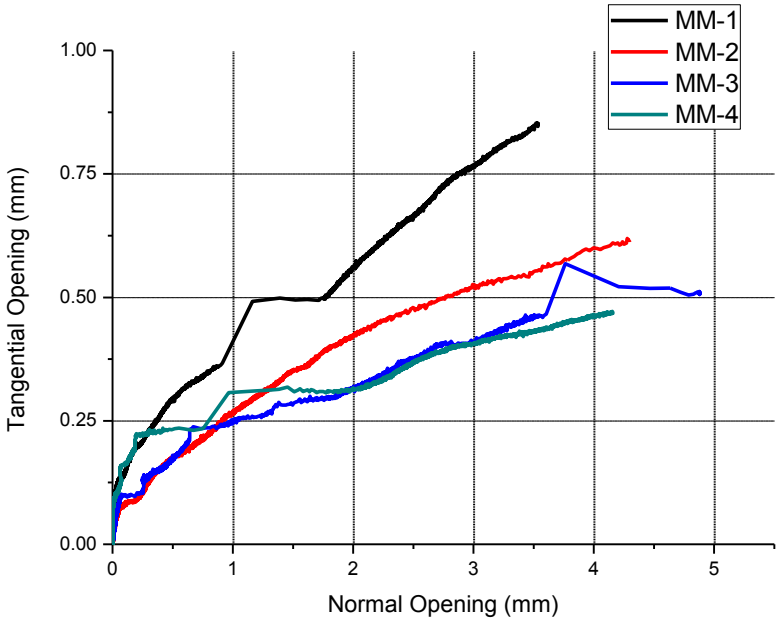

Figure 3.5. Normal versus tangential opening for MCFRP/MSteel=-6.

The ratio of normal to tangential end-opening is of an average value $\frac{\delta_n}{\delta_t} = 10$. This means that the loading mode is closer to Mode I than to Mode II loading.

- For moment ratio $\frac{M_{CFRP}}{M_{Steel}} = -3.4$ five specimens were tested. The moment arms used are l_1=-86.5mm for the steel beam and l_2=+289mm for the CFRP beam.

  Figures 3.6-3.7 show the load versus the openings from all five specimens together:

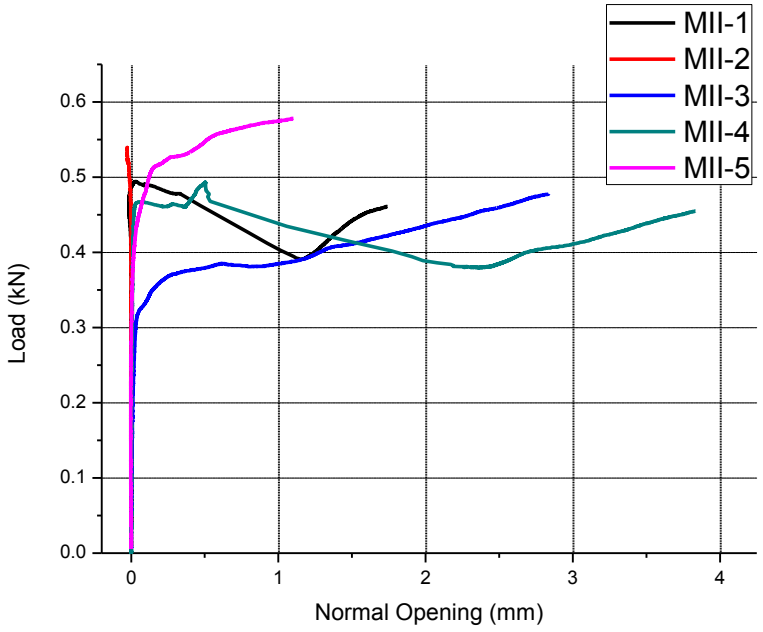

Figure 3.6. Load versus normal opening for MCFRP/MSteel=-3.4.

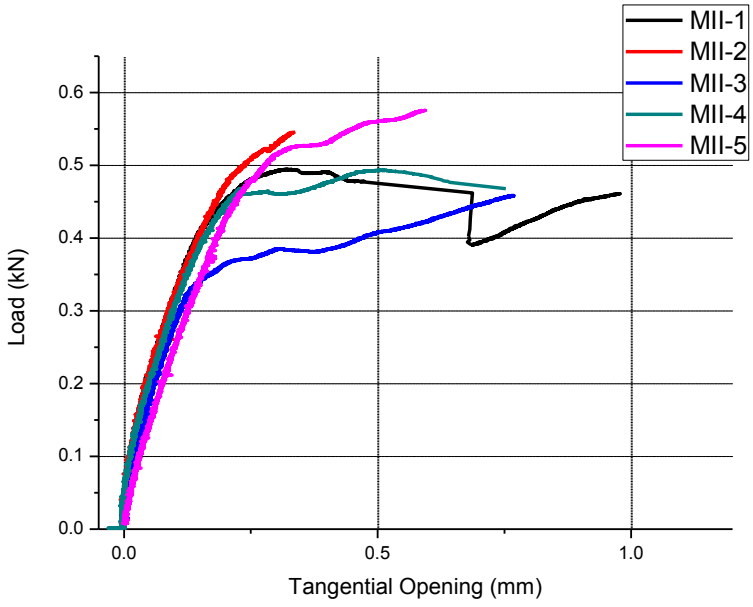

Figure 3.7. Load versus tangential opening for MCFRP/MSteel=-3.4.

Figure 3.8 shows the normal opening versus the tangential opening for all five specimens. For all specimens, there is an increase of the tangential opening of about 0.25mm at the beginning of the experiment without any significan normal opening. However, after the crack started propagating, the normal opening increased substantially overcoming the tangential opening. The average ratio of openings is $\frac{\delta_n}{\delta_t} = 2$, which means that the test was closer to Mode II than the previous moment ratio, but still there was significant Mode I opening. Thus, a pure Mode II test was not achieved with this moment ratio. The initial finite element simulation (see page 38) that was performed to evaluate the needed moment ratios in order to achieve pure Modes of opening was not absolutely correct. This was expected, as the cohesive laws of the adhesive joint were unknown still then and their values that were used in the modelling procedure had to be initially assumed. This assumption led to a miscalculation of the pure Mode II moment ratio configuraiton.

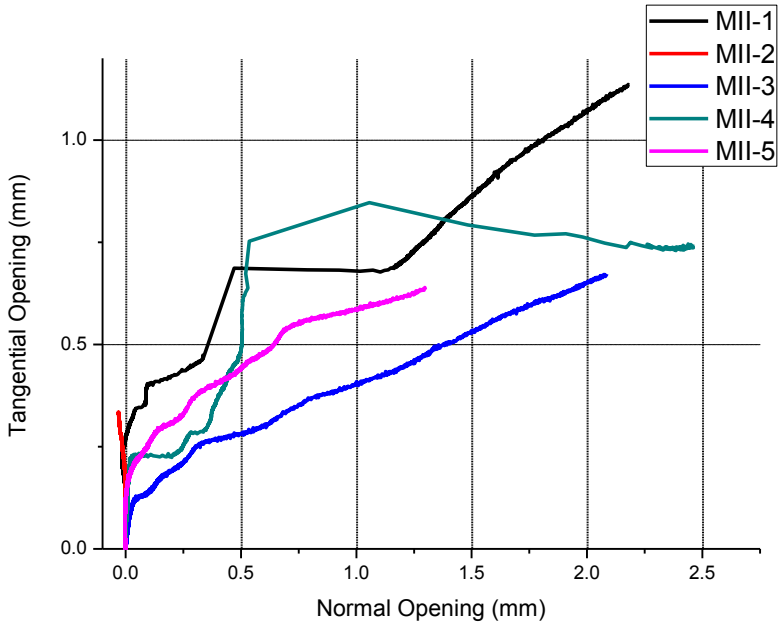

Figure 3.8. Tangential versus normal opening for MCFRP/MSteel=-3.4.

Failure began for load values varying from 0.33kN up to 0.52kN. Crack propagated through the CFRP-adhesive interface for specimens MII-1, MII-2, MII-5 and through the steel-adhesive interface for specimens MII-3 and MII-4. This can be seen in Figure 3.8, where a specimen after testing is shown. The ratio of tangential to normal opening is higher than the mixed mode tests, but the tests are still not mode-II dominated. During testing, the composite beam failed shortly after the crack began to propagate, more specifically when moment M_{CFRP} reached an average value of 150Nm (load value of 0.52kN). Delamination occurred at the gripping part of the composite beam as seen in Figure 3.9. No data are available after this point. This means that most probably it wasn't possible to achieve a pure Mode II test with these specimens since an even higher moment would be needed.

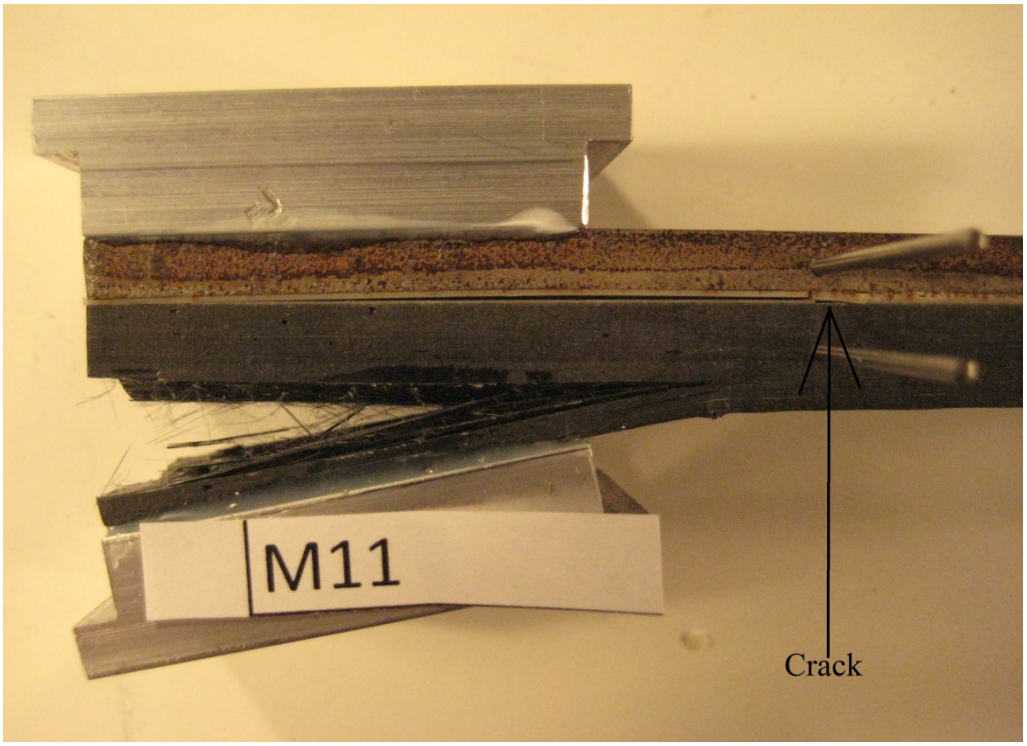

Figure 3.9. DCB specimen MII-5 after testing, showing the delamination that occurred at the gripping part of the CFRP and the crack propagating through the CFRP-adhesive interface.

The fact that the normal opening of MII-2 specimen decreased rather than increased before failure can be attributed to the fact that the thickness of the CFRP was higher than the average. This led to the two beams moving closer together: the moment of inertia of the CFRP beam increased causing a smaller deflection to be achieved. Delamination occurred early for this specimen, before the crack propagated significantly. On the contrary, specimen MII-3 presented a thickness smaller than the average, so the crack started to propagate at a lower load.

3.2. Energy release rate

Having measured the load and the openings, now it is possible to measure the energy release rate G for each specimen analytically in the context of linear elastic fracture mechanics. The calculation of the energy release rate is made analytically following the procedure presented by Suo and Hutchinson [22]. Thus, the specimen has been considered as a bimaterial joint which means that the adhesive layer has been ignored. For the double-cantilever beam specimen and the loading configuration of pure moments, the energy release rate calculated by the J-integral approach is given by [23]:

$$G = \frac{c_2}{16h^3}\left(\frac{M_1^{\,2}}{I_1} + \frac{M_2^{\,2}}{I_2} - \frac{(M_1 - M_2)^2}{I_3}\right) \tag{3.2}$$

where the symbols are explained here,

$$c_m = \frac{\kappa_m + 1}{\mu_m}, \tag{3.3}$$

$$\kappa_m = \frac{3 - \nu_m}{1 + \nu_m} \quad \text{for plane stress and } \kappa_m = 3 - 4\nu_m \text{ for plane strain,} \tag{3.4}$$

μ_m is the shear modulus of material m, m=1,2 with 1 being the CFRP and 2 the steel and ν_m is the Poisson´s ratio,

$$I_1 = \frac{1}{12n^3} \tag{3.5}$$

$$I_2 = \frac{1}{3n^3} + \frac{\Delta}{n}\left(\Delta - \frac{1}{n}\right) + \Sigma\left[\left(\frac{1}{n} - \Delta\right)^2 + \left(\frac{1}{n} - \Delta\right) + \frac{1}{3}\right] \tag{3.6}$$

$$I_3 = \frac{2}{n^3} + \frac{3}{2n} + \frac{3}{n^2} + \frac{\Sigma}{4} \tag{3.7}$$

$$\Delta = \frac{1 + 2\Sigma n + \Sigma n^2}{2n(1 + \Sigma n)} \tag{3.8}$$

$n = \frac{h}{H}$ is the thickness of steel to CFRP ratio (see Figure 3.10), (3.9)

$\Sigma = \frac{\bar{E}_1}{\bar{E}_2}$, with $\bar{E}_m = E_m$ for plane stress and $\bar{E}_m = \frac{E_m}{1 - \nu_m^{\,2}}$ for plane strain conditions. (3.10)

M_m, is the moment per unit thickness that are applied at the edges of each beam, as shown in Figure 3.10.

As it can be seen from Equation (3.2), the energy release rate depends on the loading and the geometry of the DCB specimen, but not on the crack length. This fact facilitates the obtention of the release rate since the crack length is usually hard to measure.

The results are based on the assumption of plane stress condition. For reasons of completeness, data were also obtained with the assumption of plane strain conditions; it has been calculated that there is an average 8% difference between the plane stress and the plane strain conditions.

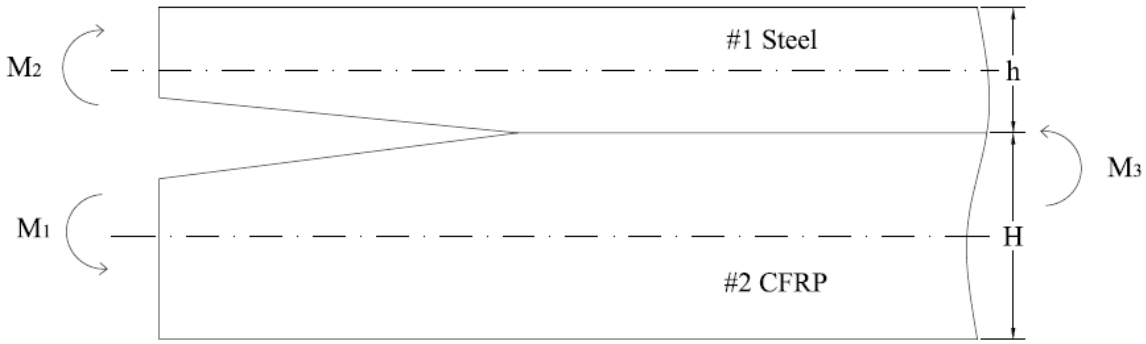

Figure 3.8. DCB-UBM specimen with the dimensions used to calculate the energy release rate.

- The results for the six specimens of moment ratio $\frac{M_{CFRP}}{M_{Steel}} = +2$ are presented next.

All curves are shown together in Figure 3.11:

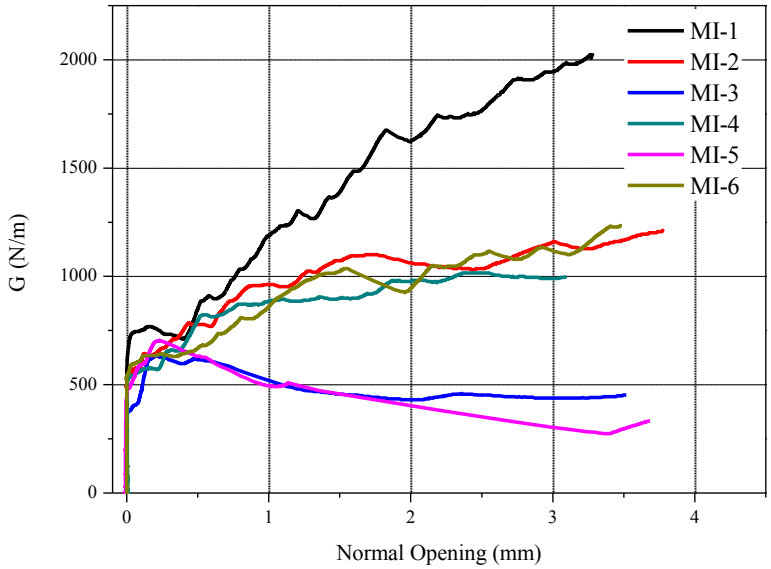

Figure 3.9. Energy release rate versus normal opening for MCFRP/MSteel=+2

As was expected from the experimental results, specimens MI-2, MI-4 and MI-6 take values closer than the rest of the specimens. For these specimens, the crack starts to propagate for values of the energy release rate of about G=500 N/m. The energy release rate then increases reaching a first slope, attaining a steady value of about G=600 N/m and then increases again reaching much higher value of about G=1000 N/m. The reason for this two different steady-state values was explained in the previous chapter: the first slope may refer to the adhesive layer failure (cohesive failure) and the second value to the interfacial failure. For specimen MI-5, the crack starts propagating for the same value as the aforementioned specimens, G=500 N/m, reaches a value of G=700 N/m and then drops substantially due to the rapid crack growth that was observed. Specimen MI-3 also presents the same rapid drop of energy release rate after having reached a value of G=650N/m. The crack started to propagate at G≈350 N/m for this specimen. For specimen MI-1, the crack starts propagating for G≈700N/m, reaching a steady value of G=750N/m and then increases rapidly as the crack moves into the CFRP beam.

- For moment ratio $\frac{M_{CFRP}}{M_{Steel}} = -6$, the four specimens gave the results shown in Figures 3.12 and 3.13:

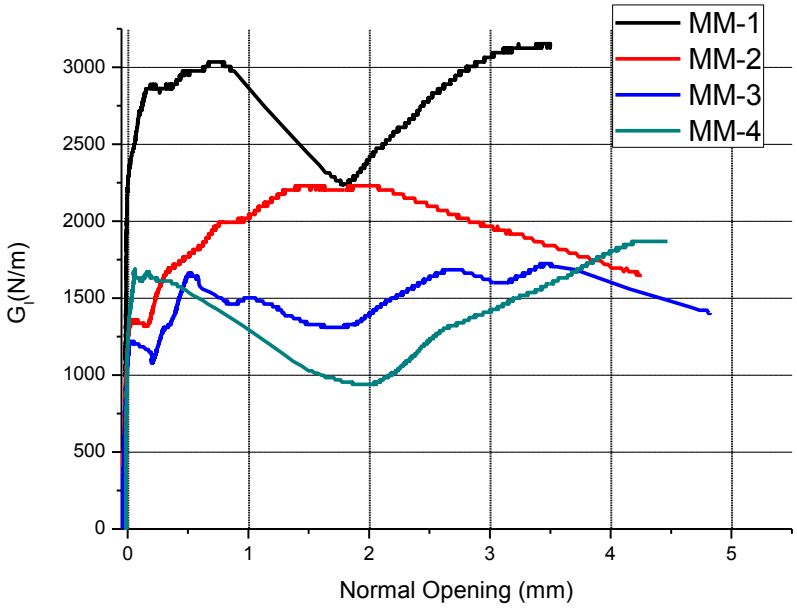

Figure 3.10. Energy release rate versus normal opening for MCFRP/MSteel=-6

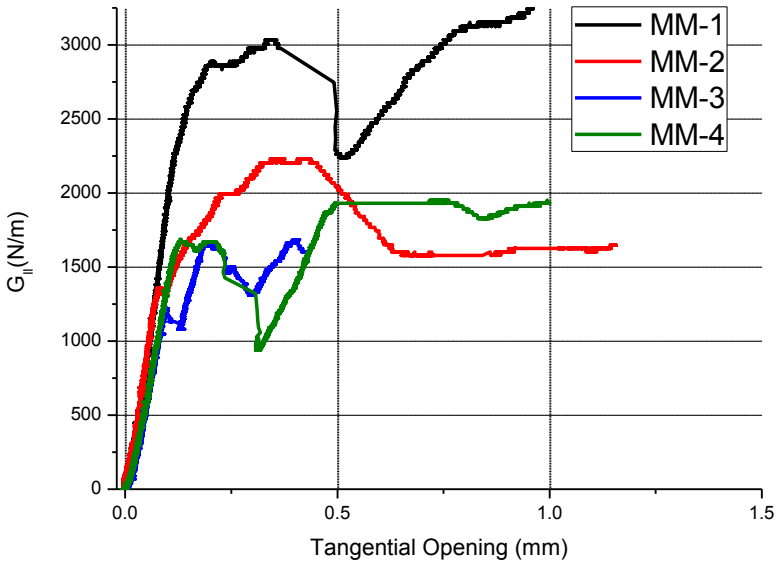

Figure 3.11. Energy release rate versus tangential opening for MCFRP/MSteel=-6.

Specimen MM-1 attains values of energy release rate much higher than the rest of the specimens, a fact that can be explained by the fact that a higher load was applied to this specimen as seen in the experimental data. The results present a significant variation that can reach values more than 100%, with MM-1 specimen reaching a maximum value of energy release rate G of 3000 N/m. The crack for MM-1 started propagating at a value of G=2300N/m. For the rest of the specimens the crack started to propagate from G=1200N/m up to G=1700N/m. For all the specimens, rapid crack growth and the respective load drop is the reason of the energy release rate decrease. With the exception of MM-1 specimen, the variation is of an average value of 50%.

- For moment ratio $\frac{M_{CFRP}}{M_{Steel}} = -3.4$ results from five specimens are presented. In Figure 3.14 the energy release rate versus the normal opening and in Figure 3.15 the energy release rate versus the tangential opening are shown:

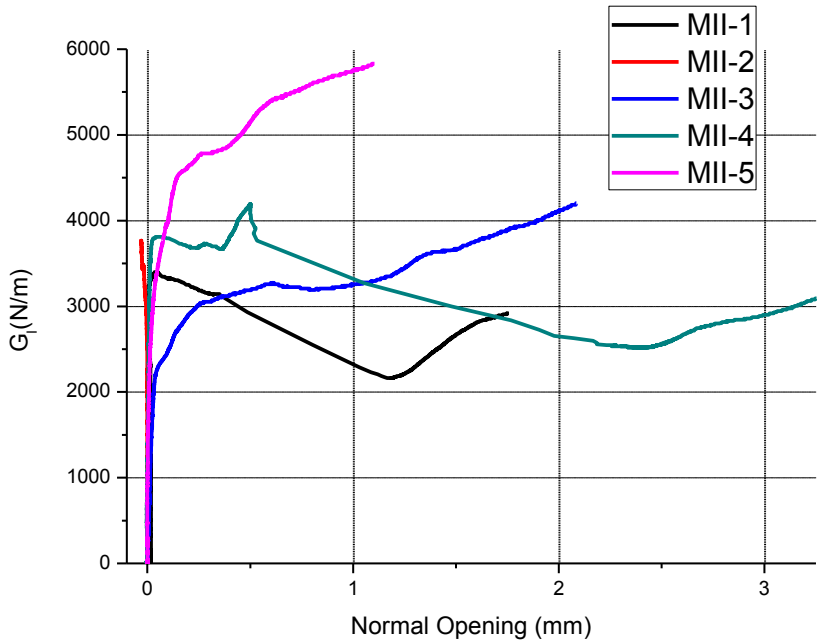

Figure 3.12. Energy release rate versus normal opening for MCFRP/MSteel=-3.4.

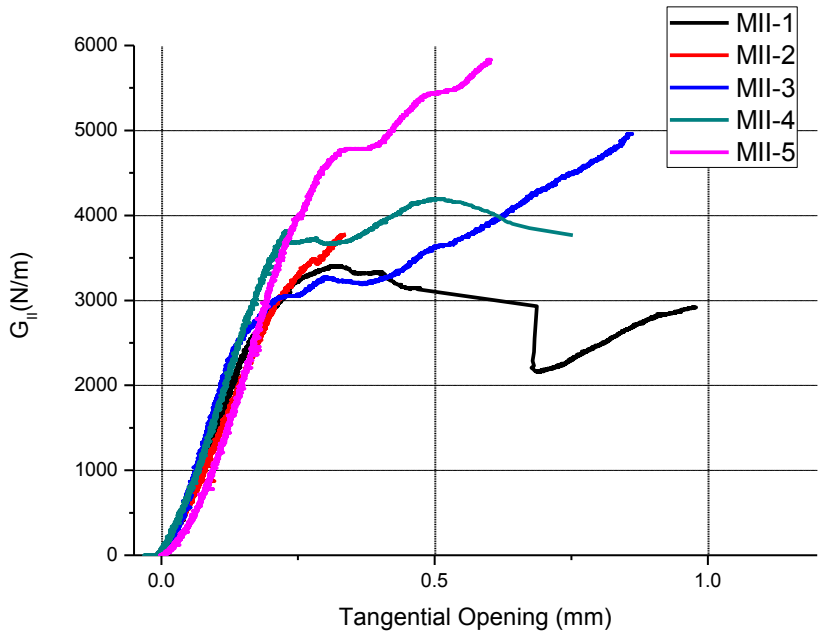

Figure 3.13. Energy release rate versus tangential opening for MCFRP/MSteel=-3.4.

As it can be seen, for this moment ratio the results present a certain divergence, with the G-δ_n curved presenting greater divergence than the G-δ_t curves. Specimen MII-2 as was expected doesn't give any significant results since the delamination occurred before the crack started to propagate significantly. The fact that specimen MII-3 presented the lowest thickness of the CFRP beam **(**see Table 2.7**)** can explain the fact that it attained the lowest values of energy release rate. In the same

way the high values of specimen MII-1 can be explained by the greater thickness of the CFRP beam of this specimen. Specimen MII-5 reached a value of 6000N/m before delamination was presented. Specimens MII-1 and MII-3 obtain closer energy release rate values with an average variaton of 25%.

From all the figures above presenting the energy release rate from experiments with three different moment ratios, it can be extracted that as the mode mixity increases and the opening is getting closer to Mode II, higher energy release rates are attained, as it was expected; the increase in fracture energy with the increase of the tangential opening can be attributed to different causes like crack face contact with the resulting friction or even to electrostatic effects between the two crack faces.

3.3. Curve Fitting

Before the cohesive laws are obtained, the G-δ curves need to be fitted to make the results smoother and facilitate the differentiation of the curve. Since the results don't present the repeatability wanted and most of the specimens do not reach a steady-state value but the curve keeps rising as the opening increases, only a part of the curve of each specimen will be used for differentiation. More specifically, the part that will be used to obtain the cohesive law will start from the first inflexion point of the curve and it will end at the first plateau of the measured curve. This first part of each curve will give the cohesive law of the adhesive; the data of this part were obtained as the crack started propagating through the adhesive layer (cohesive failure).

In Figure 3.16 a typical G-δ_n curve that will be used for the fit is presented along with useful dimensions. G_o is the initial value of the energy release rate at the inflexion point and G_{ss} is the steady-state value, meaning the value of G as it reaches the plateau. Figure 3.17 shows a typical G-δ_t curve. Its shape is different from the G-δ_n curve, as there is a change of curvature for small opening values. A steady-state value of the energy release rate is also reached here at the critical opening.

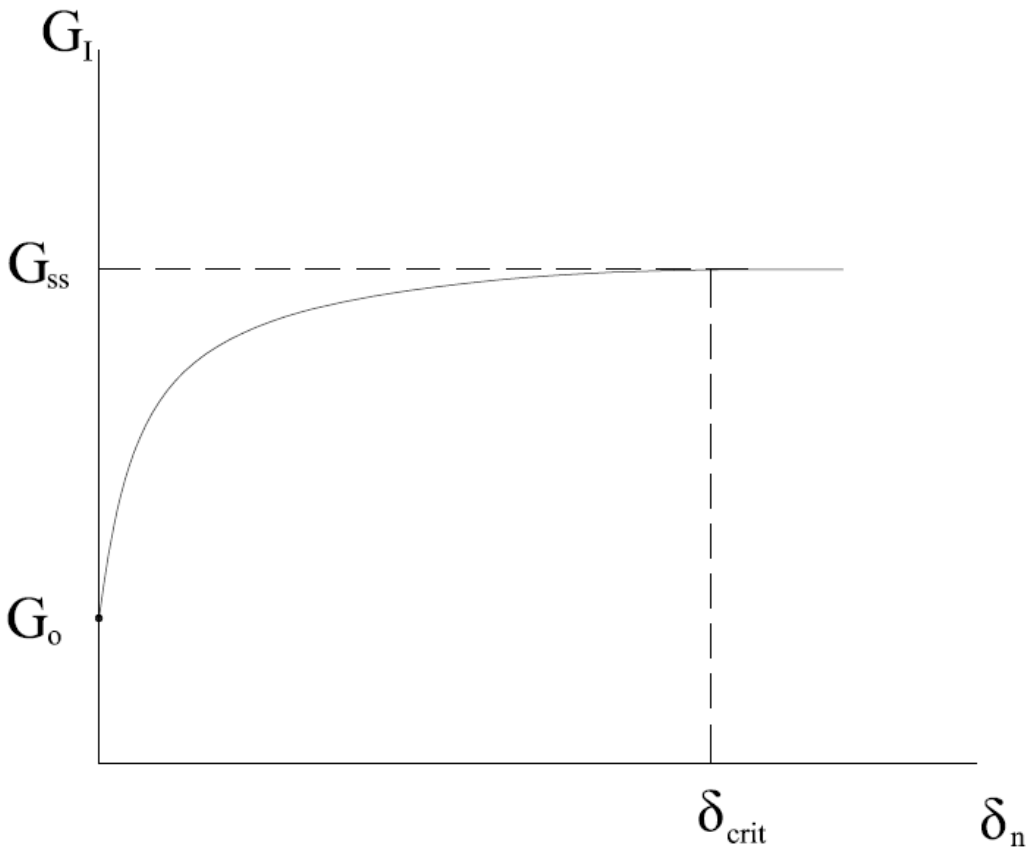

Figure 3.14. Typical curve of energy release rate versus normal opening.

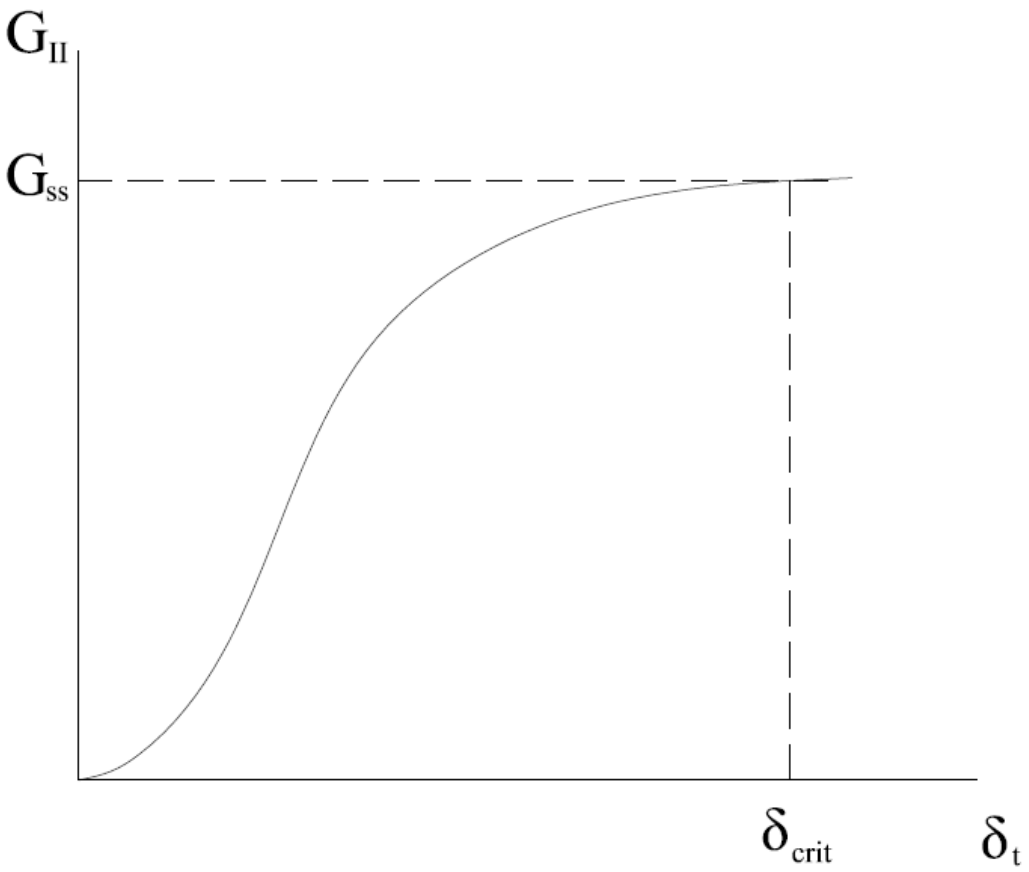

Figure 3.15. Typical curve of energy release rate versus tangential opening.

In the following figures, the fitted part of the G-δ curves is presented along with the fitted curve of each specimen followed by a table with the data used to produce the fitted curve.

First, the specimens with moment ratio $\frac{M_{CFRP}}{M_{Steel}} = +2$ are presented. The adjusted R-Square is a measure of the goodness of the fit, with a value equal to one being a perfect fit.

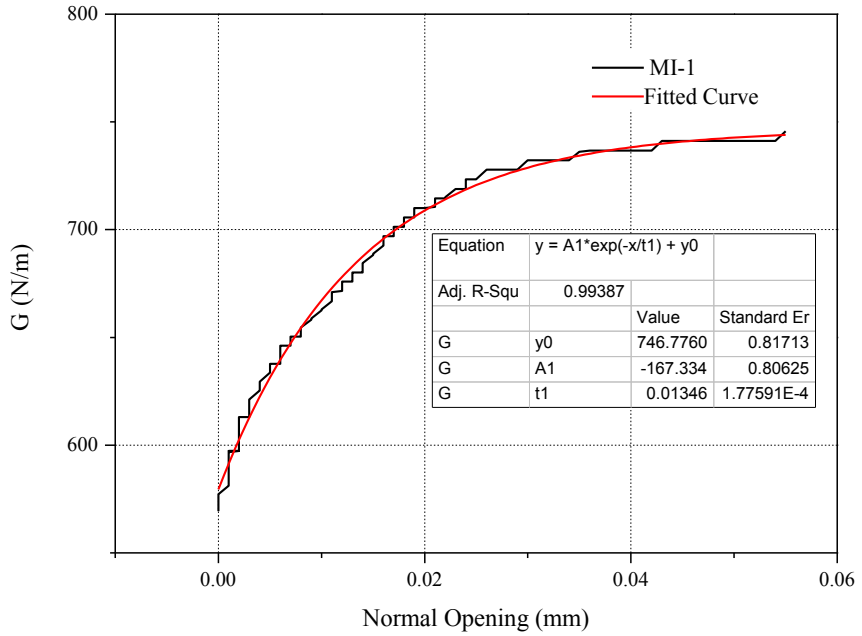

Figure 3.16. The fitted curve with the original data for specimen MI-1.

Table 3.1. The data used to produce the fitted curve of Figure 3.14.

Equation	y = A1*exp(-x/t1) + y0	
Adj. R-Square	0.99387	
		Value
	y0	746.77609
	A1	-167.33415
	t1	0.01346

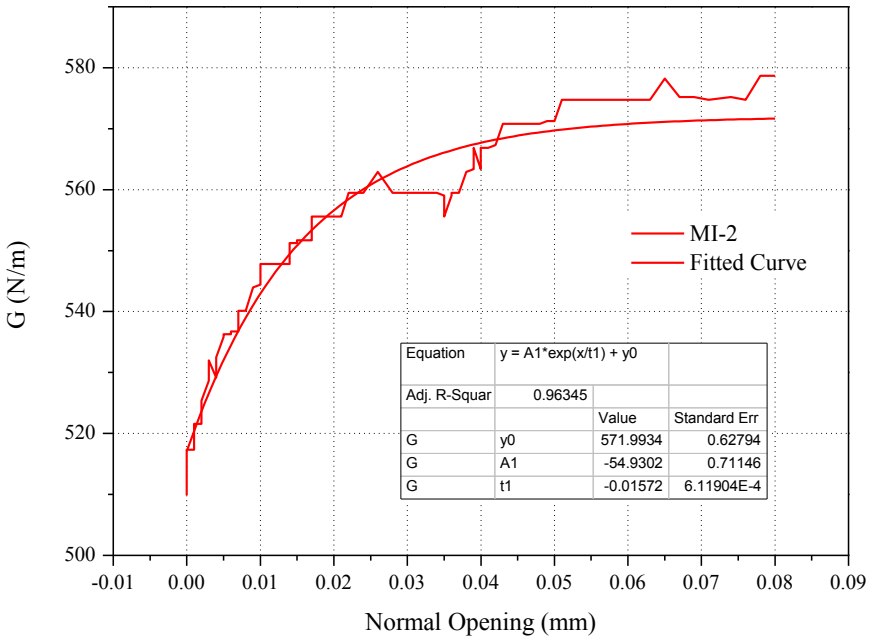

Figure 3.17. The fitted curve with the original data for specimen MI-2.

Table 3.2. The data used to produce the fitted curve of Figure 3.15.

Equation	y = A1*exp(x/t1) + y0	
Adj. R-Square	0.96345	
		Value
	y0	571.99344
	A1	-54.93021
	t1	-0.01572

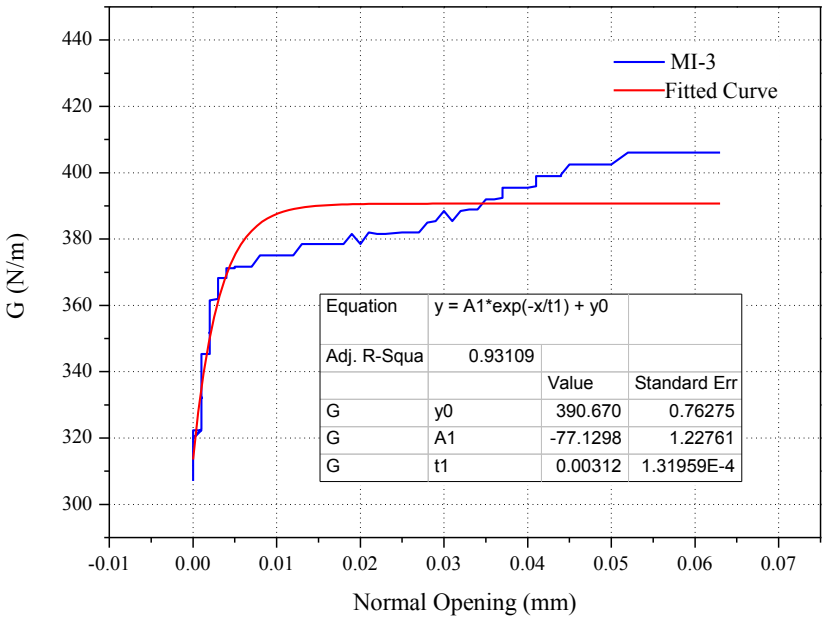

Figure 3.18. The fitted curve with the original data for specimen MI-3.

Table 3.3. The data used to produce the fitted curve of Figure 3.16.

Equation	y = A1*exp(-x/t1) + y0	
Adj. R-Square	0.93109	
		Value
	y0	390.67092
	A1	-77.12987
	t1	0.00312

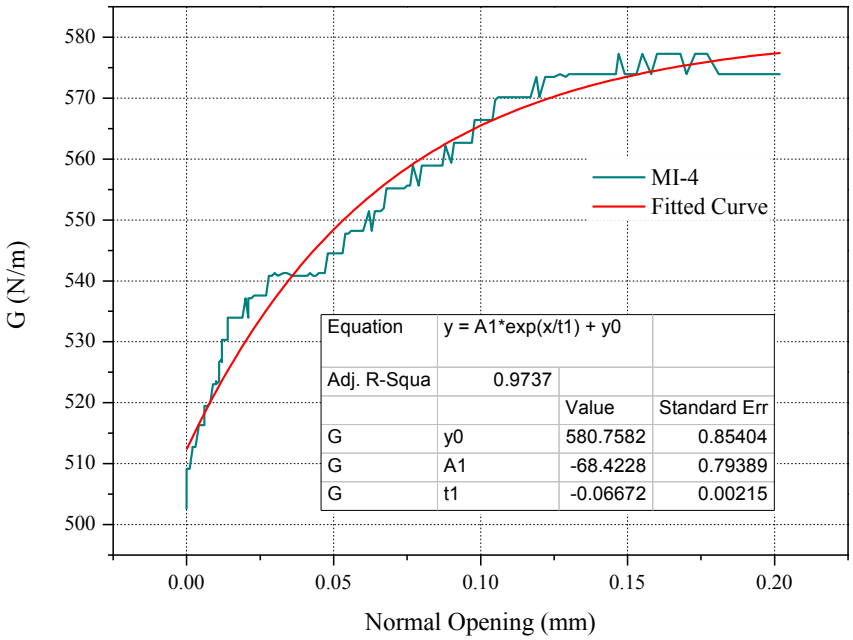

Figure 3.19. The fitted curve with the original data for specimen MI-4.

Table 3.4. The data used to produce the fitted curve of Figure 3.17.

Equation	y = A1*exp(x/t1) + y0	
Adj. R-Square	0.9737	
		Value
	y0	580.75825
	A1	-68.42289
	t1	-0.06672

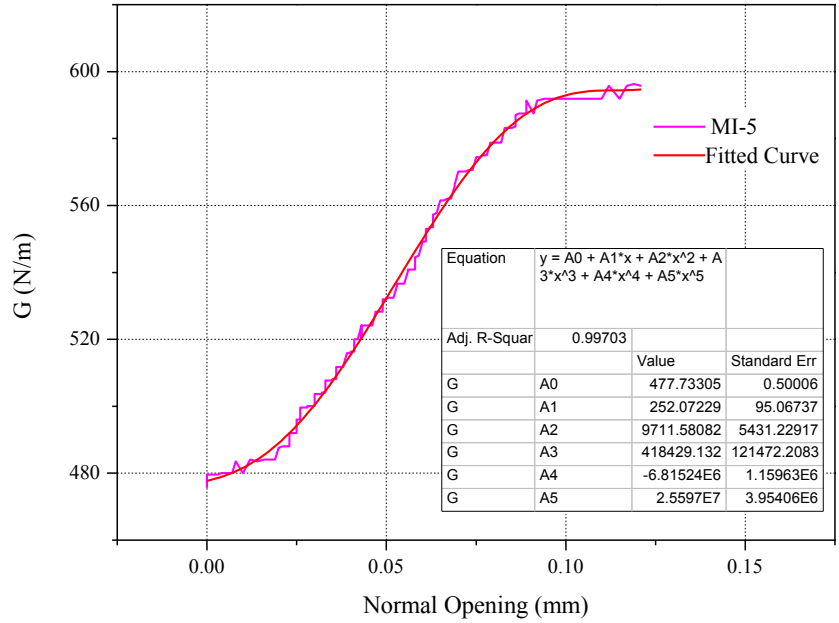

Figure 3.20. The fitted curve with the original data for specimen MI-5.

Table 3.5. The data used to produce the fitted curve of Figure 3.18.

Equation	y = A0 + A1*x + A2*x^2 + A3*x^3 + A4*x^4 + A5*x^5
Adj. R-Square	0.99703
	Value
A0	477.73305
A1	252.07229
A2	9711.58082
A3	418429.1327
A4	-6.82E+06
A5	2.56E+07

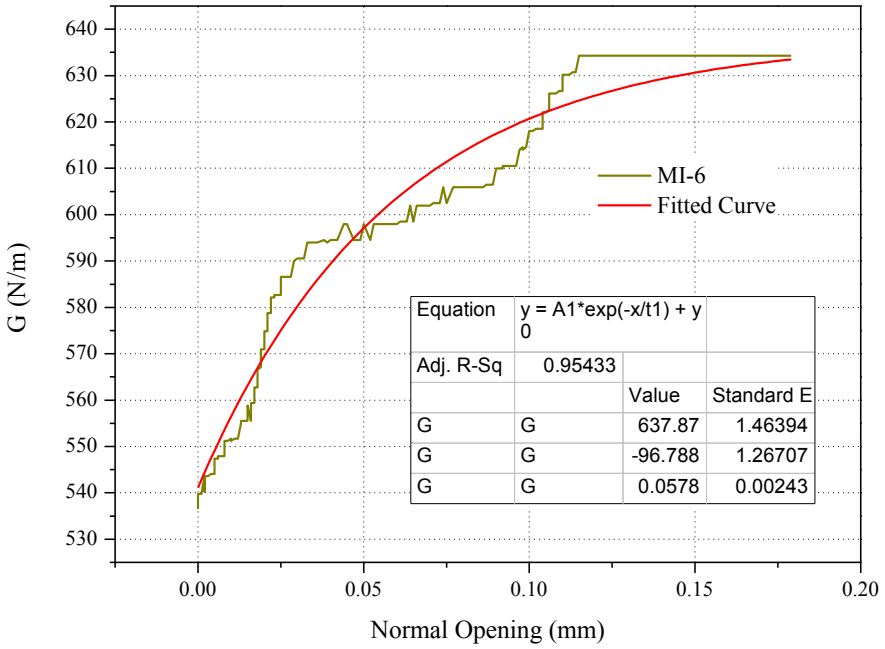

Figure 3.21. The fitted curve with the original data for specimen MI-6.

Table 3.6. The data used to produce the fitted curve of Figure 3.19.

Equation	y = A1*exp(-x/t1) + y0	
Adj. R-Square	0.95433	
		Value
	y0	637.8726
	A1	-96.78836
	t1	0.05785

All fitted curves present an adjusted R-square more than 0.9 which means a good approximation has been made. All specimens, with the exception of MI-5 present the same shape; the energy release rate increases monotonically with the increase of the normal opening, reaching a first steady state value. These specimens were fitted with an exponential equation. Specimen MI-5 presents a sigmoidal shape and thus a different equation had to be chosen. A polynomial fit was done resulting with a very high R-square, meaning a very good fit was achieved.

Next, the specimens with moment ratio $\frac{M_{CFRP}}{M_{Steel}} = -6$ are presented, first the energy release rate versus the normal opening in Figures 3.24 to 3.27 and then the energy release rate versus the tangential opening in Figures 3.28 to 3.31.

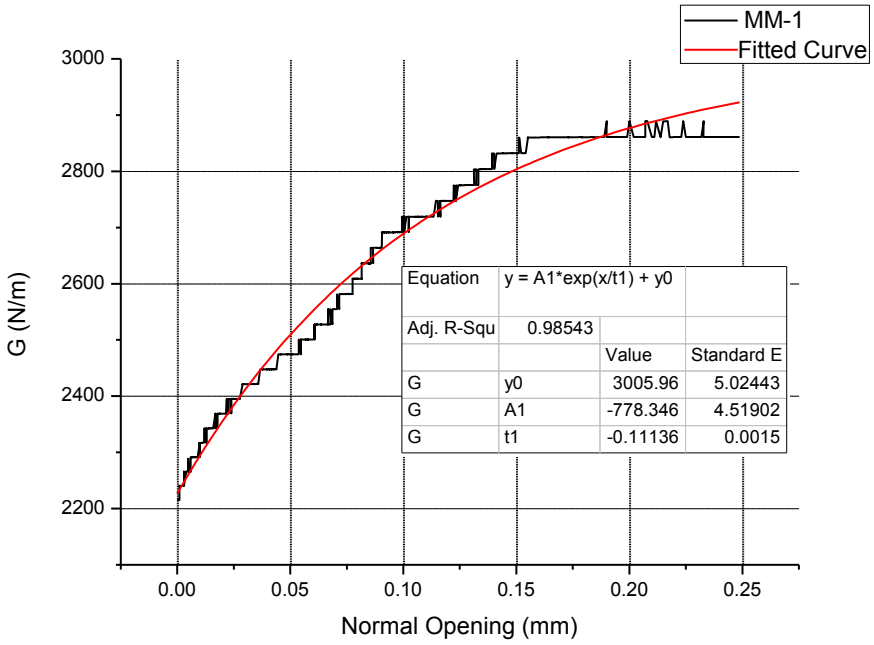

Figure 3.22. The fitted curve with the original data for specimen MM-1.

Table 3.7. The data used to produce the fitted curve of Figure 3.20.

Equation	y = A1*exp(x/t1) + y0
Adj. R-Square	0.98543
	Value
y0	3005.9628
A1	-778.34695
t1	-0.11136

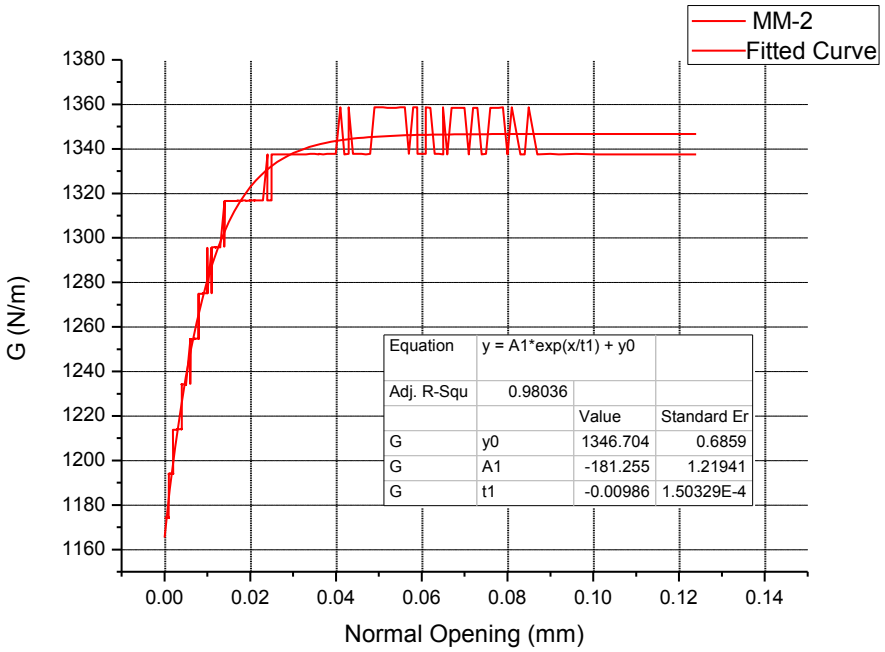

Figure 3.23. The fitted curve with the original data for specimen MM-2.

Table 3.8. The data used to produce the fitted curve of Figure 3.21.

Equation	y = A1*exp(x/t1) + y0
Adj. R-Square	0.98036
	Value
y0	1346.70459
A1	-181.25557
t1	-0.00986

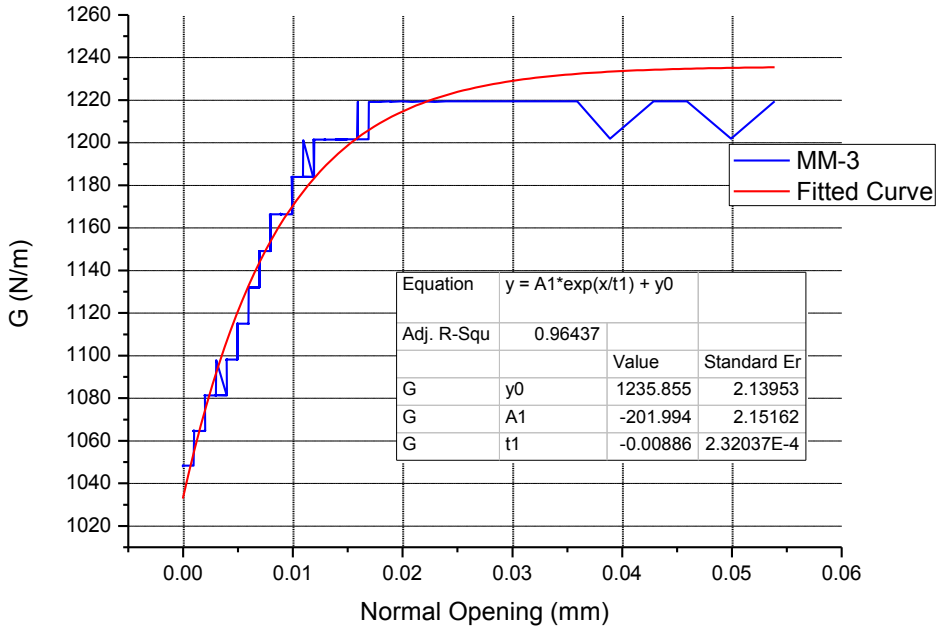

Figure 3.24. The fitted curve with the original data for specimen MM-3.

Table 3.9. The data used to produce the fitted curve of Figure 3.22.

Equation	y = A1*exp(x/t1) + y0	
Adj. R-Square	0.96437	
		Value
	y0	1235.85501
	A1	-201.99493
	t1	-0.00886

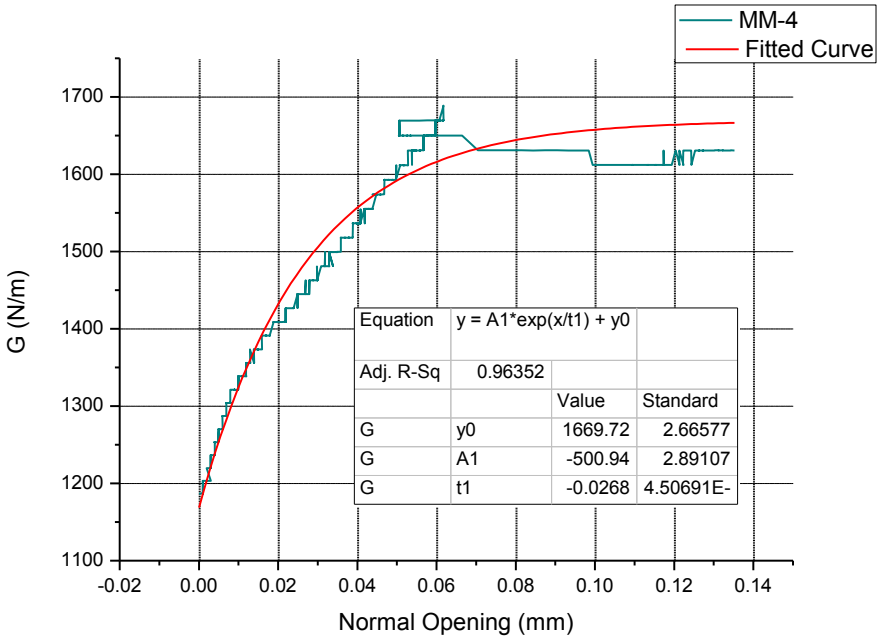

Figure 3.25. The fitted curve with the original data for specimen MM-4.

Table 3.10. The data used to produce the fitted curve of Figure 3.23.

Equation	y = A1*exp(x/t1) + y0
Adj. R-Square	0.96352
	Value
y0	1669.72571
A1	-500.94574
t1	-0.02688

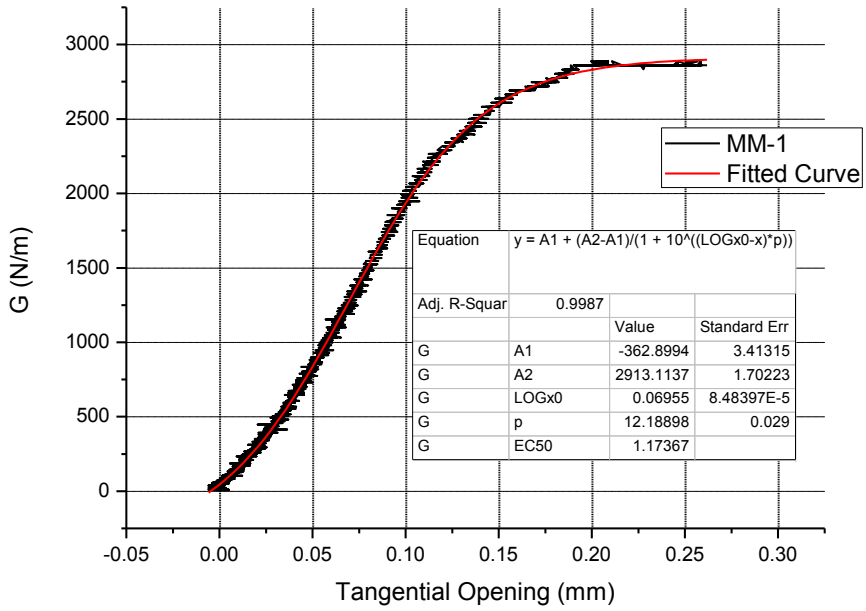

Figure 3.26. The fitted curve with the original data for specimen MM-1.

Table 3.11. The data used to produce the fitted curve of Figure 3.24.

Equation	y = A1 + (A2-A1)/(1 + 10^((LOGx0-x)*p))
Adj. R-Square	0.9987
	Value
A1	-362.89947
A2	2913.11371
LOGx0	0.06955
p	12.18898
EC50	1.17E+00

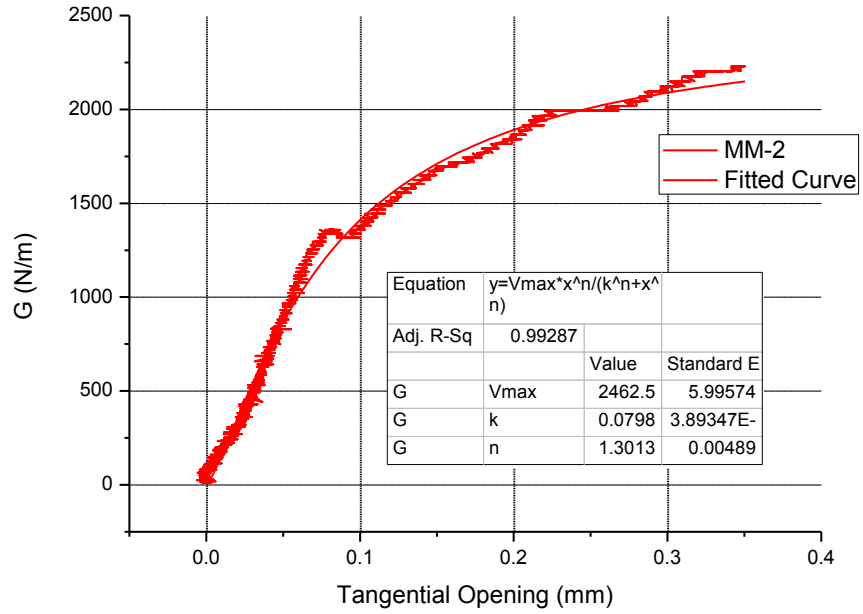

Figure 3.27. The fitted curve with the original data for specimen MM-2.

Table 3.12. The data used to produce the fitted curve of Figure 3.25.

Equation	y=Vmax*x^n/(k^n+x^n)	
Adj.	R-Square	0.99287
	Value	
	Vmax	2462.5321
	k	0.07983
	n	1.30134

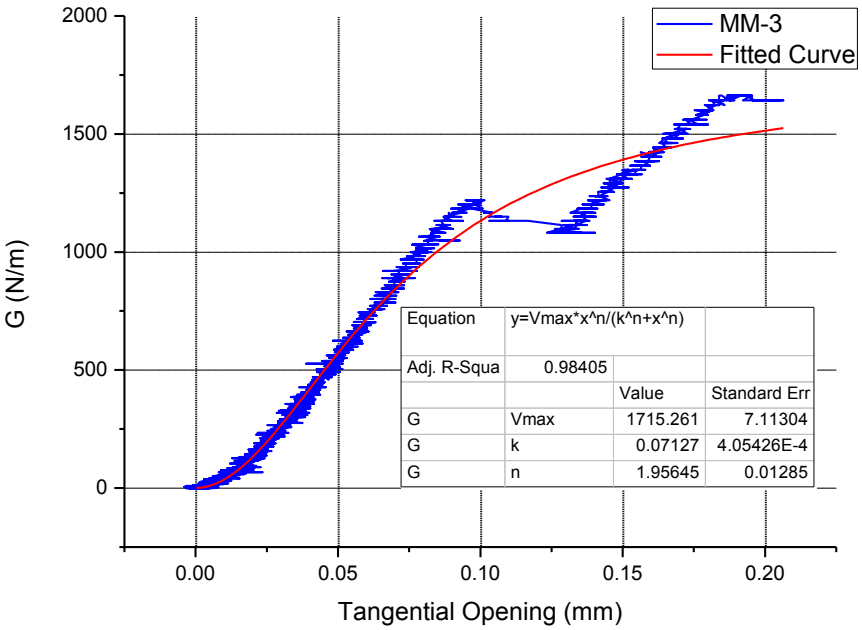

Figure 3.28. The fitted curve with the original data for specimen MM-3.

Table 3.13. The data used to produce the fitted curve of Figure 3.26.

Equation	y=Vmax*x^n/(k^n+x^n)	
Adj. R-Square	0.98405	
		Value
	Vmax	1715.26109
	k	0.07127
	n	1.95645

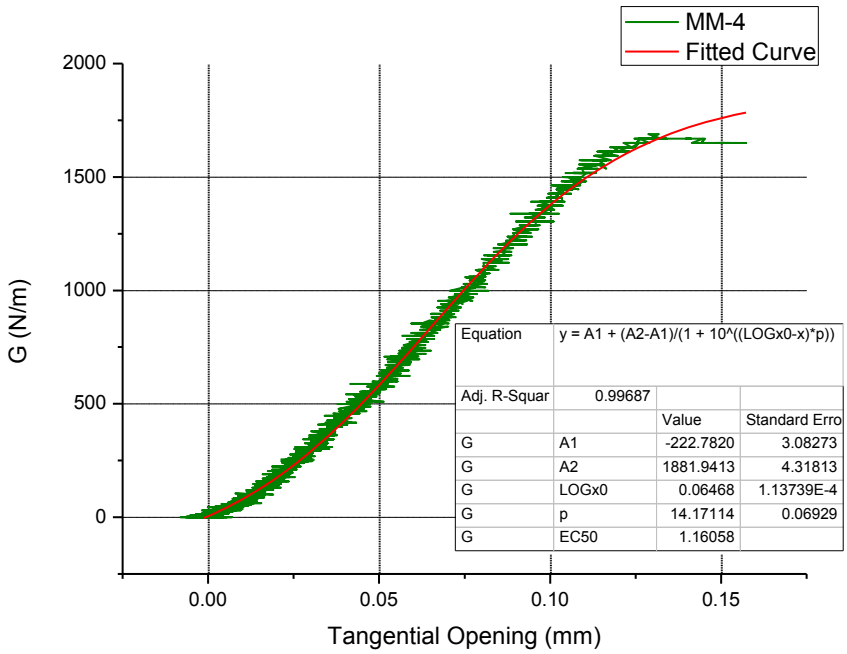

Figure 3.29. The fitted curve with the original data for specimen MM-4.

Table 3.14. The data used to produce the fitted curve of Figure 3.27.

Equation	y = A1 + (A2-A1)/(1 + 10^((LOGx0-x)*p))
Adj. R-Square	0.99687
	Value
A1	-222.78202
A2	1881.94137
LOGx0	0.06468
p	14.17114
EC50	1.16E+00

All the fitted curves present high values of the adjusted R-square. For the G-δ_n curves, an exponential equation has been fitted with very good results while for the G-δ_t a sigmoid equation has been used since the curves present a sigmoidal shape.

The fitted curves for the specimens with moment ratio $\frac{M_{CFRP}}{M_{Steel}} = -3.4$ are presented next. Figures 3.32 to 3.35 show the energy release rate versus the normal opening, while Figures 3.36 to 3.39 the energy release rate versus the tangential opening. Specimen MII-2 is not used for fitting due to the early delamination that occurred, and so it didn't give any significant results.

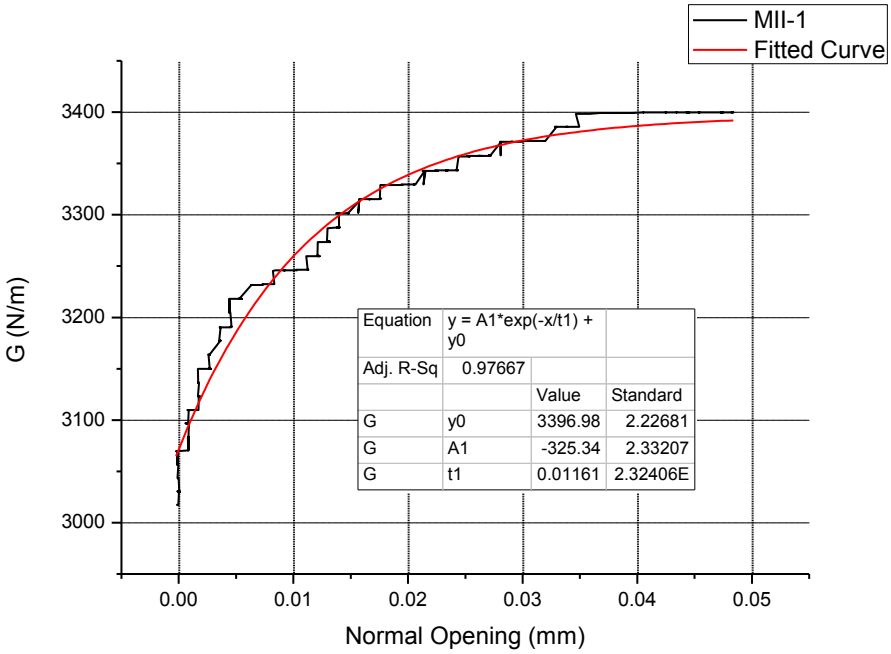

Figure 3.30. The fitted curve with the original data for specimen MII-1.

Table 3.15. The data used to produce the fitted curve of Figure 3.28.

Equation	y = A1*exp(-x/t1) + y0	
Adj. R-Square	0.97667	
		Value
	y0	3396.98825
	A1	-325.34453
	t1	0.01161

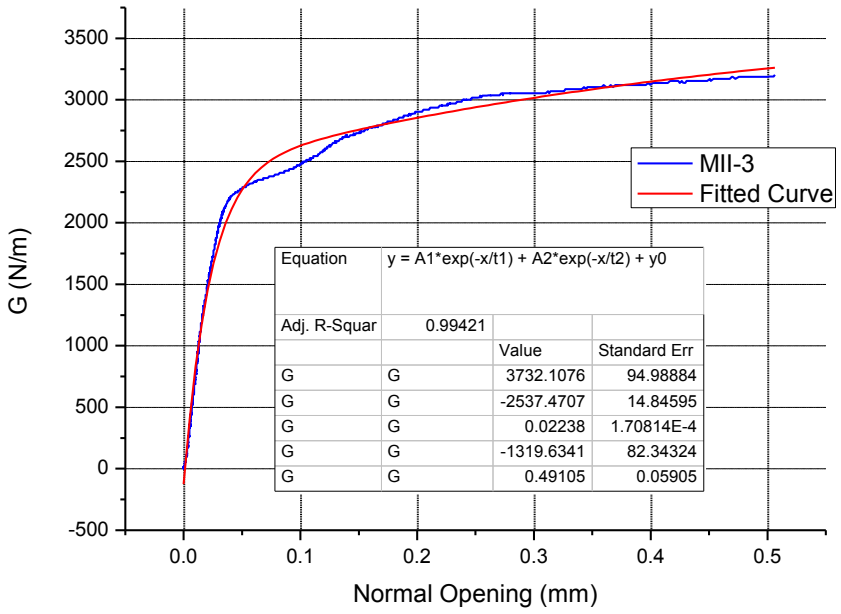

Figure 3.31. The fitted curve with the original data for specimen MII-3.

Table 3.16. The data used to produce the fitted curve of Figure 3.29.

Equation	y = A1*exp(-x/t1) + A2*exp(-x/t2) + y0	
Adj. R-Square	0.99421	
		Value
	y0	3732.10769
	A1	-2537.47075
	t1	0.02238
	A2	-1319.63412
	t2	4.91E-01

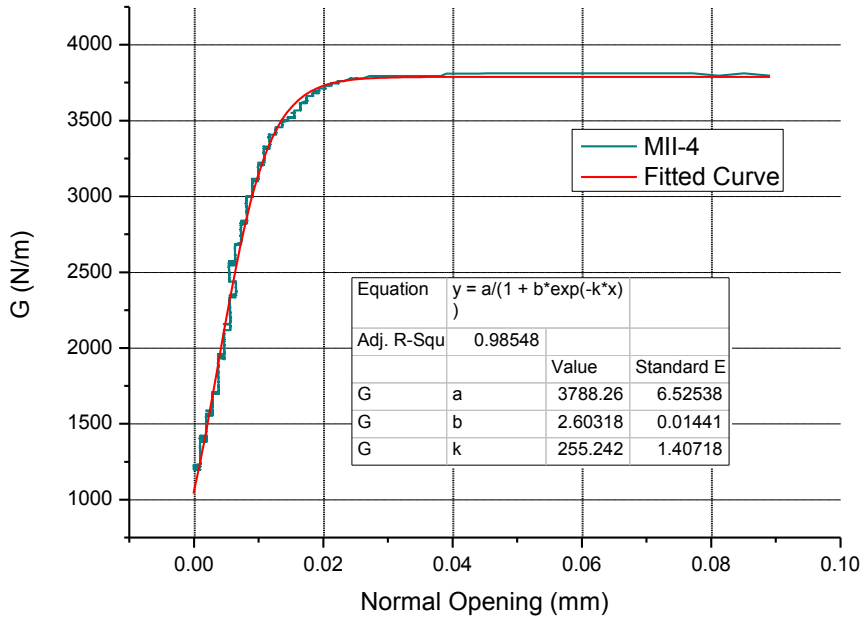

Figure 3.32. The fitted curve with the original data for specimen MII-4.

Table 3.17. The data used to produce the fitted curve of Figure 3.30.

Equation	y = a/(1 + b*exp(-k*x))	
Adj. R-Square	0.98548	
		Value
	a	3788.26849
	b	2.60318
	k	255.24219

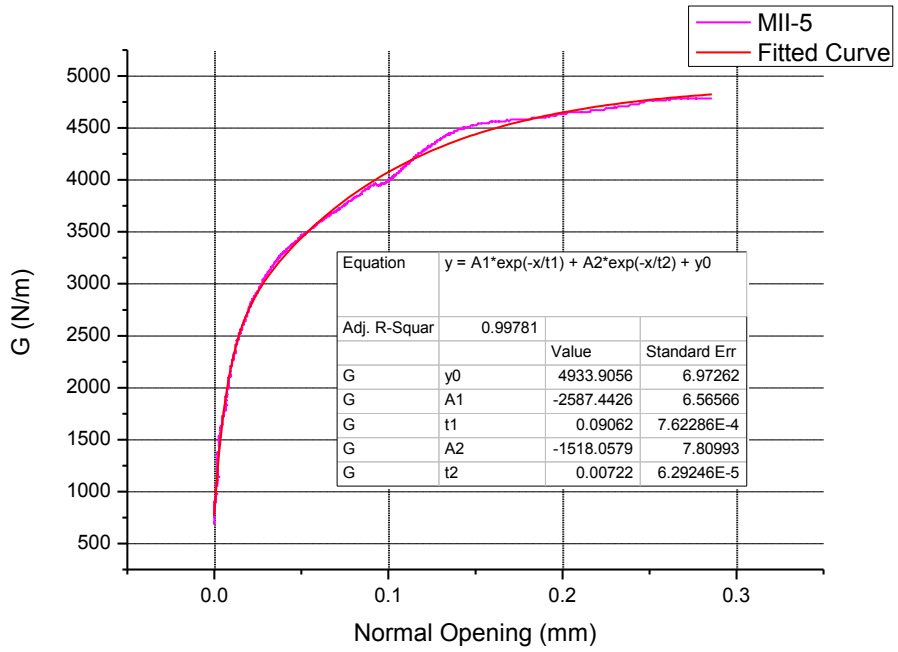

Figure 3.33. The fitted curve with the original data for specimen MII-5.

Table 3.18. The data used to produce the fitted curve of Figure 3.31.

Equation	y = A1*exp(-x/t1) + A2*exp(-x/t2) + y0	
Adj. R-Square	0.99781	
		Value
	y0	4933.90565
	A1	-2587.44268
	t1	0.09062
	A2	-1518.05791
	t2	7.22E-03

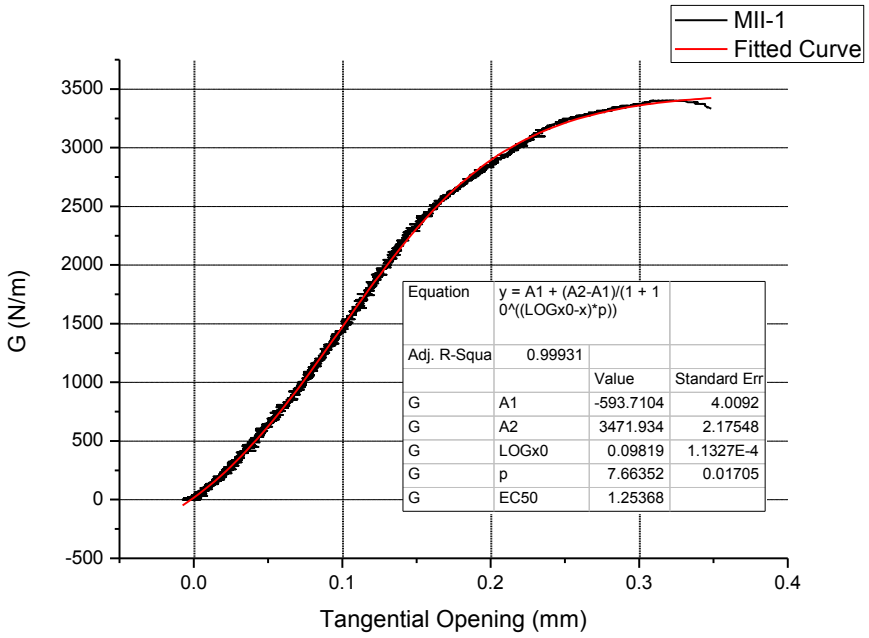

Figure 3.34. The fitted curve with the original data for specimen MII-1.

Table 3.19. The data used to produce the fitted curve of Figure 3.32.

Equation	y = A1 + (A2-A1)/(1 + 10^((LOGx0-x)*p))
Adj. R-Square	0.99931
	Value
A1	-593.71041
A2	3471.93457
LOGx0	0.09819
p	7.66352
EC50	1.25E+00

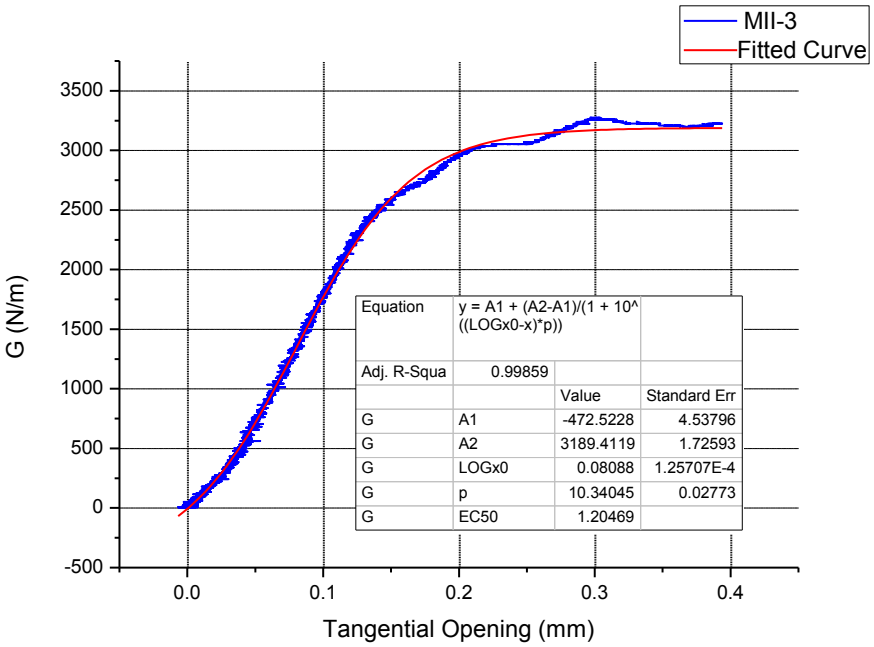

Figure 3.35. The fitted curve with the original data for specimen MII-3.

Table 3.20. The data used to produce the fitted curve of Figure 3.33.

Equation	y = A1 + (A2-A1)/(1 + 10^((LOGx0-x)*p))
Adj. R-Square	0.99859
	Value
A1	-472.52283
A2	3189.41198
LOGx0	0.08088
p	10.34045
EC50	1.20E+00

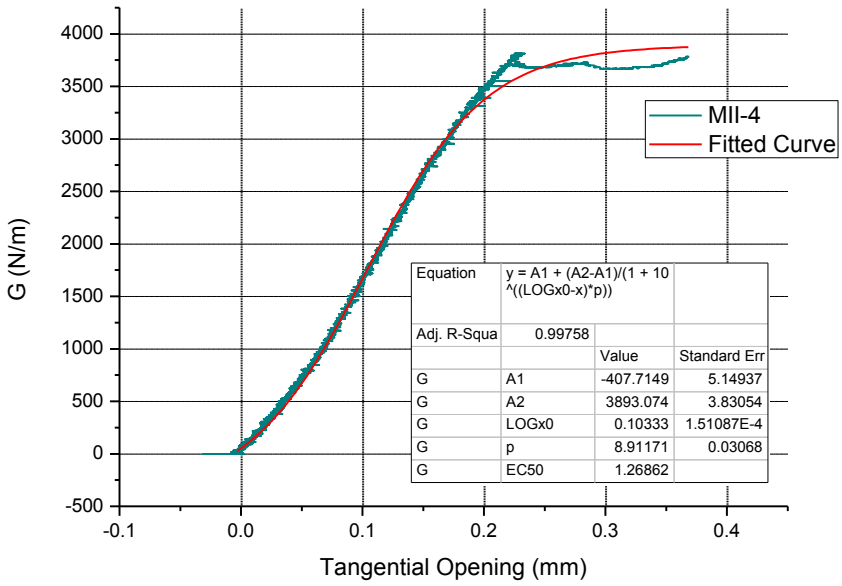

Figure 3.36. The fitted curve with the original data for specimen MII-4.

Table 3.11. The data used to produce the fitted curve of Figure 3.34.

Equation	y = A1 + (A2-A1)/(1 + 10^((LOGx0-x)*p))
Adj. R-Square	0.99758
	Value
A1	-407.71495
A2	3893.07428
LOGx0	0.10333
p	8.91171
EC50	1.27E+00

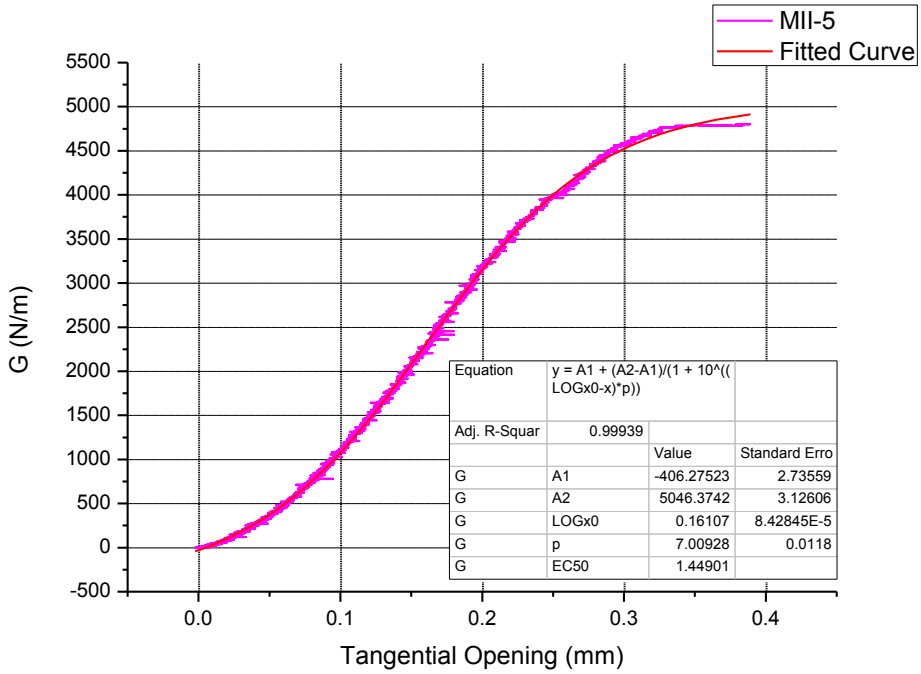

Figure 3.37. The fitted curve with the original data for specimen MII-5.

Table 3.22. The data used to produce the fitted curve of Figure 3.35.

Equation	y = A1 + (A2-A1)/(1 + 10^((LOGx0-x)*p))
Adj. R-Square	0.99939
	Value
A1	-406.27523
A2	5046.3742
LOGx0	0.16107
p	7.00928
EC50	1.45E+00

All the fitted curves present a value of adjusted R-square higher than 0.97. For the G-δ_n curves exponential equations were fitted to the data, while for the G-δ_t curves sigmoid equations were used.

3.4. Derivation of cohesive laws

Having fitted the G-δ curves, the derivation of the cohesive laws is now straight-forward according to Equations (1.3) and (1.4) (since LEFM apply in our case, then the energy release rate is equal to the J-integral). Mode I cohesive laws will be obtained through the differentiation of the G-δ_n curves and Mode II cohesive laws through the differentiation of the G-δ_t curves. That means that the differentiation will result to a curve of traction versus opening for each specimen.

Typical derived cohesive laws are presented in Figures 3.40 and 3.41. In the first Figure the Mode I cohesive law is shown; the curve starts with the maximum traction σ_{max} and then decreases in a non-linear way reaching zero at the critical opening δ_{crit}. In Figure 3.41, a typical Mode II cohesive law is shown with the traction starting at a certain value, then increasing up to the maximum traction σ_{max} and finally decreasing again to zero at the critical tangential opening. The area enclosed by the traction-separation curve is equal to the $G_{coh}=G_{ss}-G_o$ (see Fig.3.16) for Mode I and $G_{coh}=G_{ss}$ (see Fig.3.17) for Mode II.

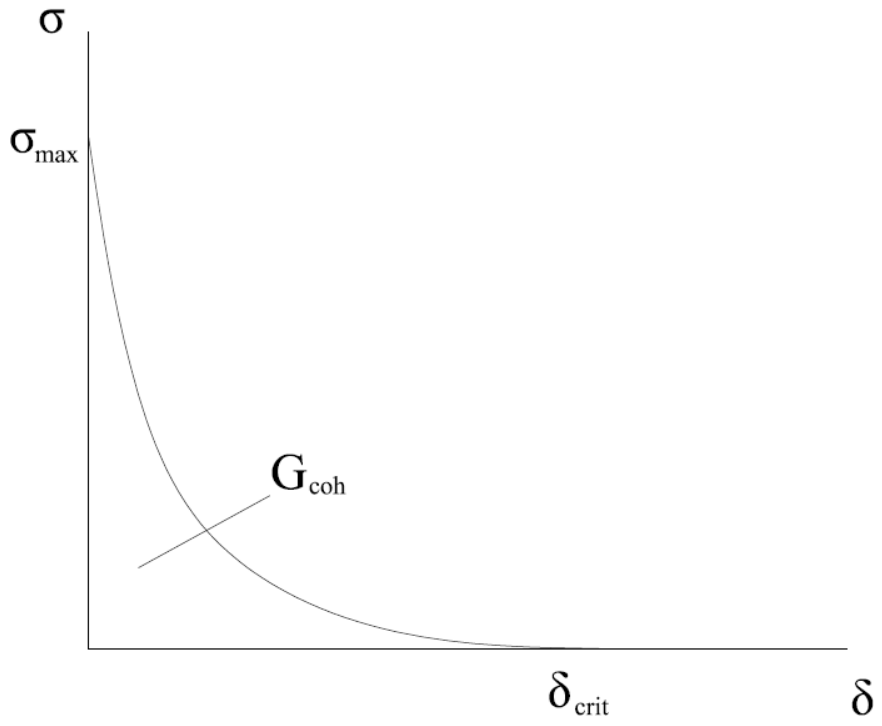

Figure 3.38. Typical derived Mode I cohesive law.

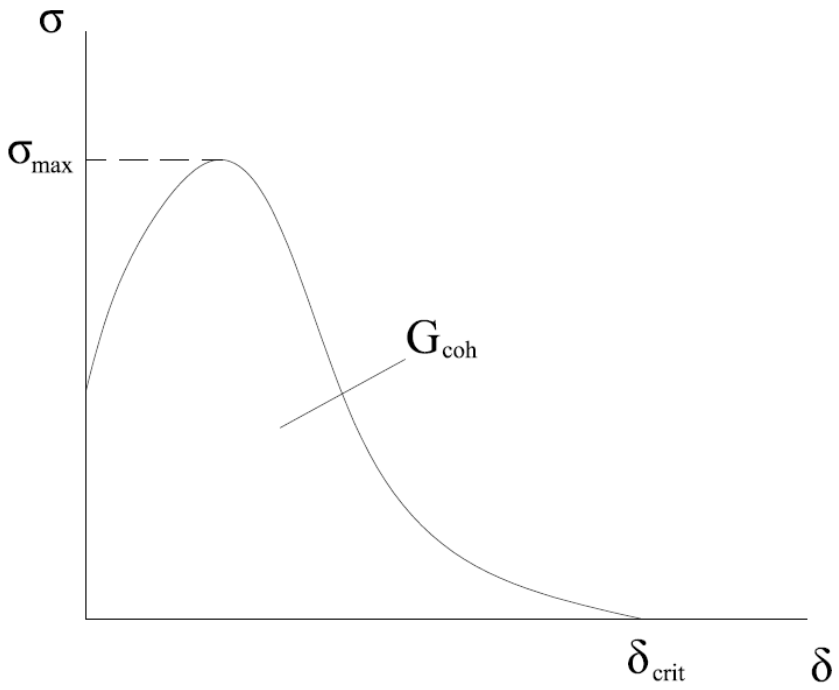

Figure 3.39. Typical derived Mode II cohesive law.

The cohesive laws are presented in the following figures. In Figure 3.42 and 3.43 the cohesive laws for specimens with moment ratio $\frac{M_{CFRP}}{M_{Steel}} = +2$ are presented.

Since the results from specimens MI-1 and MI-3 give much higher values than the rest of the specimens, they are treated as a different set and they are presented in a different graph, Figure 3.43.

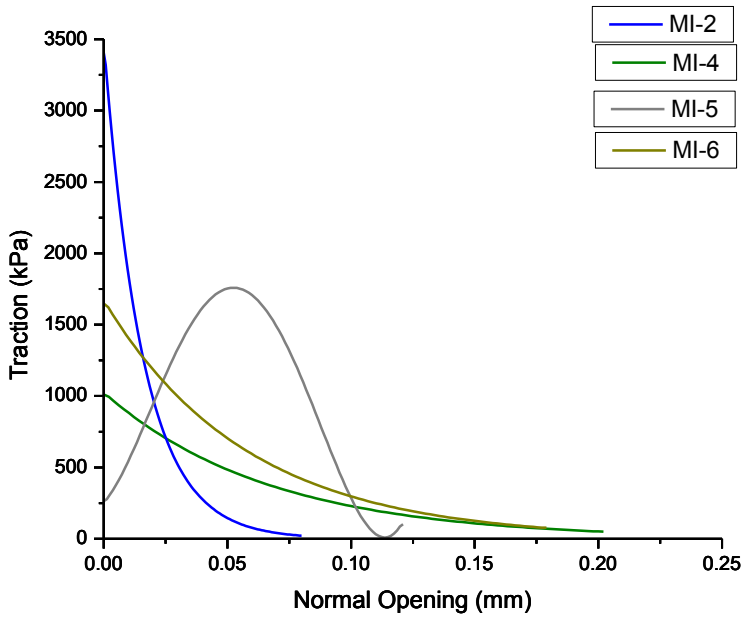

Figure 3.40. Derived Mode I cohesive laws of specimens MI-2, MI-4, MI-5 and MI-6.

With the exception of specimen MI-5, all the other specimens present the same shape, since their derivation came from the differentiation of an exponential equation, while for MI-5 a polynomial equation was used. For δ_n=0, the traction starts with the highest value, ranging from 1000 kPa for specimen MI-4 up to 3000 kPa for specimen MI-2. The traction decreases as the opening increases reaching eventually zero at the critical opening. The traction of specimen MI-5 reaches its highest value of about σ_{max}=1.8MPa at δ=0.05mm and then starts decreasing again.

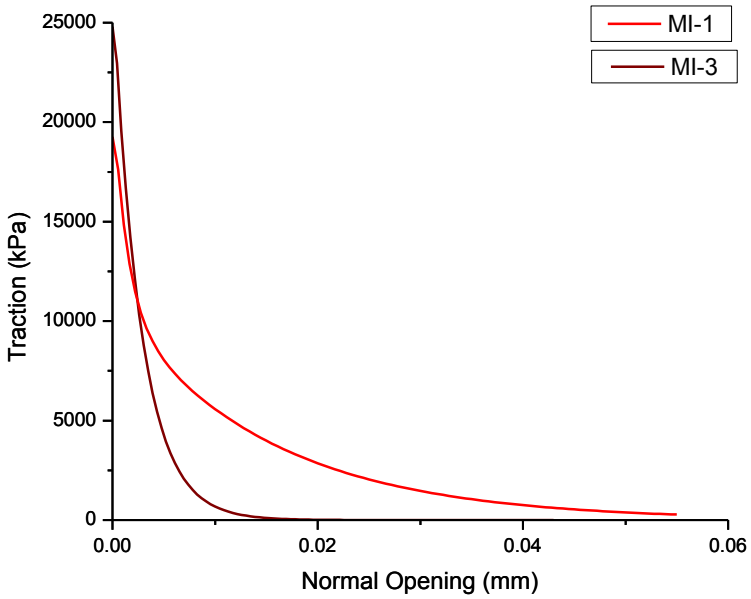

Figure 3.41. Derived Mode I cohesive laws of specimens MI-1 and MI-3.

Traction of specimens MI-1 and MI-3 began with higher values (σ_{max}=19.3MPa for MI-1 and σ_{max}=24.8MPa for MI-3) compared to the other specimens of the same moment ratio. The shape of the cohesive law however remains the same.

The cohesive laws are derived from the results that were measured during the experiments, so it is expected that they do not present the repeatability wanted. The energy release rate curves measured from the experiments presented significant deviation, thus the obtained cohesive laws present a similar deviation. The same stands for the rest of the calculated cohesive laws.

Next, the derived cohesive laws of the specimens with moment ratio $\frac{M_{CFRP}}{M_{Steel}} = -6$ are presented. In Figure 3.44 the Mode I traction-separations laws are shown, with specimens MM-2, MM-3 and MM-4 giving more similar results than specimen MM-1. Specimen MM-3 presented the highest value of traction with σ_{max}=22.2MPa while specimen MM-1 gave lower results than the rest of the specimens.

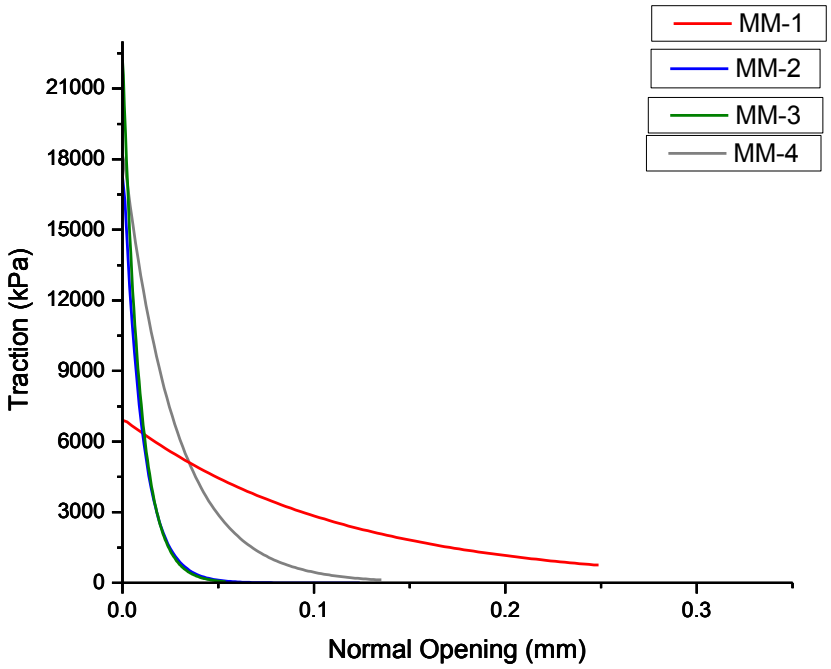

Figure 3.42. Derived Mode II cohesive laws of specimens MM-1 to MM-4.

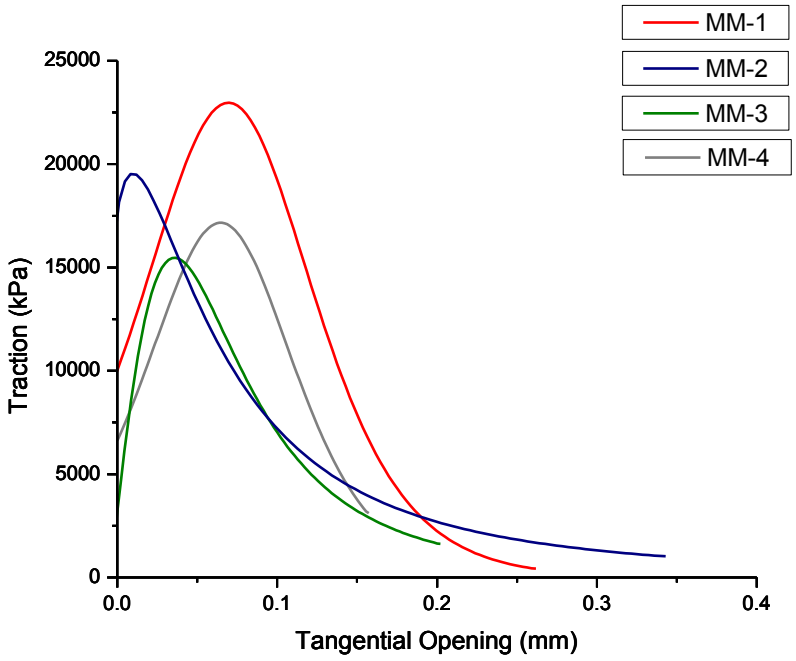

Figure 3.43. Derived Mode II cohesive laws of specimens MM-1 to MM-4.

In Figure 3.45 the Mode II traction-separation laws are shown. Specimen MM-4 gives again the highest value of traction. The results are not so sparse as was observed with the specimens with moment ratio $\frac{M_{CFRP}}{M_{Steel}} = +2$. Specimens MM-1 and MM-4 present more similar results than the other specimens.

Finally, the results from the specimens with moment ratio $\frac{M_{CFRP}}{M_{Steel}} = -3.4$ are shown in Figures 3.46 and 3.47. The results for the Mode I cohesive laws do not present significant repeatability as it can be seen in the following graph. For specimen MII-4 the G-δ_n was fitted with a sigmoid curve to obtain a better fit and the cohesive law shape derived is different than the rest of the specimens that were fitted with an exponential equation.

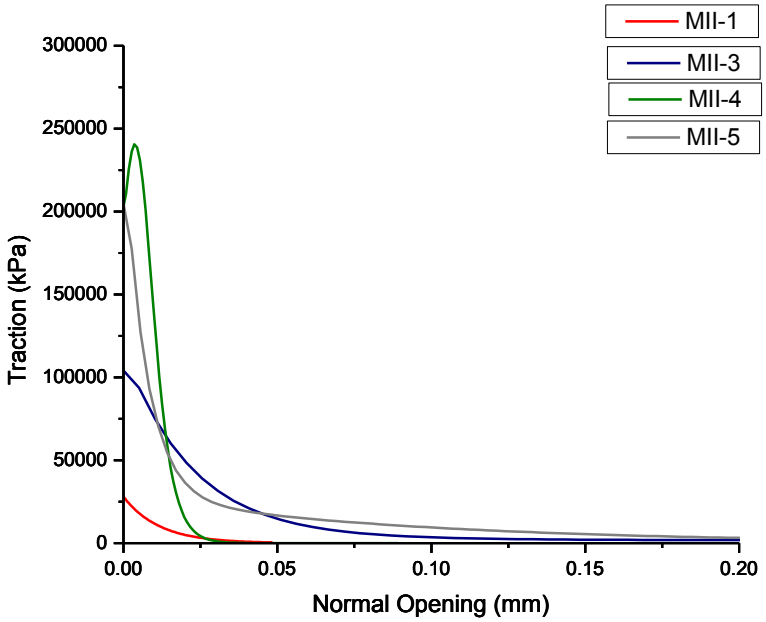

Figure 3.44. Derived Mode I cohesive laws of specimens MII-1, MII-3, MII-4 and MII-5.

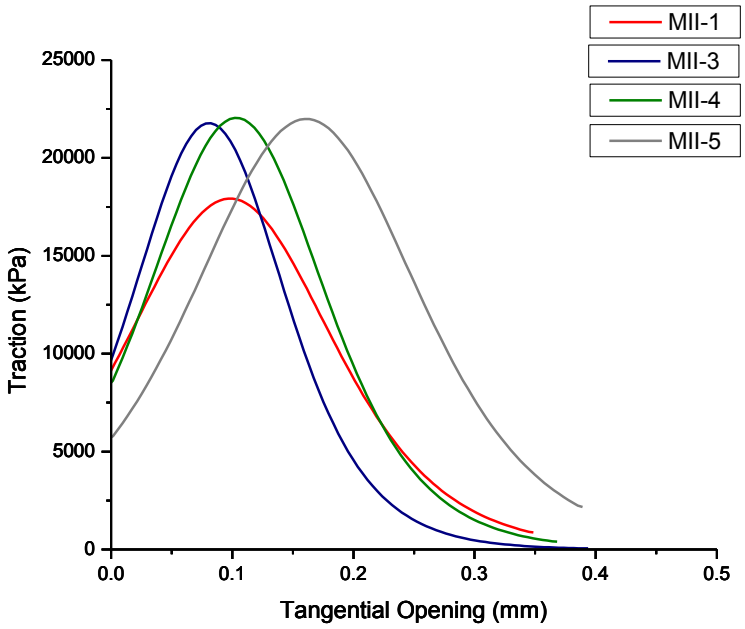

Figure 3.45. Derived Mode II cohesive laws of specimens MII-1, MII-3, MII-4 and MII-5.

For Mode II cohesive laws, specimens MII-3, MII-4 and MII-5 reach about the same maximum traction, $\sigma_{max} \approx 22.5$ MPa. The critical openings are not the same for all the specimens, without having however very sparse values, ranging around 0.37mm.

Next, the data that can be extracted from all the previous figures are summarized in Tables 3.23-3.27. For each specimen, the steady-state value of the energy release rate G_{ss} is presented, the initial value of the energy release rate G_o, the critical openings and the maximum tractions. G_{coh}/data equals to the subtraction G_{ss}-G_o and G_{coh}/integrated is the result from integrating the cohesive laws using the data analysis software OriginLab. These two values should be close for the traction-separation law derivation procedure to be correct. Otherwise, it is an indication of a mathematical error in the procedure. Thus, their percentage difference is presented in the same table. It can be seen that the derivation is mathematically correct since the difference of these two values is very small.

As it was mentioned before, the derived data present the same characteristics with the cohesive law curves, meaning that there is a deviation in the values listed below due to the dissimilar curves of the experimental results. Specimen MI-1 and MI-3 present higher values of energy release rate and maximum traction than the rest of the Mode I specimens. The critical openings for the Mode I specimens range from 0.02mm for specimen MI-3 up to 0.2mm for specimen MI-4 and MI-6. About the mixed mode specimens, for the Mode I cohesive law data, specimen MM-1 takes the highest values of energy release rate compared to the other specimens. It presents G_{ss}=2922N/m at a δ_{nc}=0.3mm, while the rest of the specimens range from 1234N/m up to 1666N/m with δ_{nc}=0.06 up to 0.14mm. For Mode II, the mixed mode specimen MM-1 presents again the highest values, while the critical opening is about the same for all specimens, around δ_{tc}=0.3mm. From the specimens with moment ratio

M_{CFRP}/M_{steel}=-3.4, MII-5 presents the highest values of the energy release rate and maximum traction while the rest of the specimens take closer values of G_{ss} ranging from 3260N/m up to 3788N/m for the Mode I cohesive law and 3187N/m up to 3874N/m for the Mode II cohesive law. Specimen MII-1 presents a very low value of maximum normal traction compared to the other specimens.

Table 3.23. Data derived from the Mode I cohesive laws from specimens with moment ratio M_{CFRP}/M_{steel}=+2.

Specimen	**MI-1**	**MI-2**	**MI-3**	**MI-4**	**MI-5**	**MI-6**
Gss (N/m)	746.2	571.7	385.6	577.4	594.7	633.5
Go (N/m)	573.4	517.1	312.8	512.3	477.7	541.1
Gcoh/data (N/m)	172.8	54.6	72.8	65.1	117.0	92.4
Gcoh/integrated (N/m)	172.7	54.6	72.9	65.1	116.9	92.4
Percentage Difference	0.1	0.0	-0.1	0.0	0.1	0.0
Crit. Normal Opening (mm)	0.062	0.08	0.023	0.2	0.12	0.2
σ_{max} (MPa)	19.3	3.4	24.8	1.0	1.7	1.6

Table 3.24. Data derived from the Mode I cohesive laws from specimens with moment ratio M_{CFRP}/M_{steel}=-6.

Specimen	**MM-1**	**MM-2**	**MM-3**	**MM-4**
Gss (N/m)	2922.6	1346.7	1235.4	1666.5
Go (N/m)	2226.8	1165.4	1032.9	1168.8
Gcoh/data (N/m)	695.8	181.3	202.5	497.7
Gcoh/integrated (N/m)	695.7	181.3	202.5	497.7
Percentage Difference	0.0	0.0	0.0	0.00
Crit. Normal Opening (mm)	0.3	0.06	0.06	0.14
σ_{max} (MPa)	6.9	17.2	22.2	18.1

Table 3.25. Data derived from the Mode II cohesive laws from specimens with moment ratio M_{CFRP}/M_{steel}=-6.

Specimen	**MM-1**	**MM-2**	**MM-3**	**MM-4**
Gss (N/m)	2898.3	2148.9	1524.8	1784.2
Go (N/m)	0	0	0	0
Gcoh/data (N/m)	2898.3	2148.9	1524.8	1784.2
Gcoh/integrated (N/m)	2908.5	2138.8	1524.8	1788.4
Percentage Difference	-0.4	0.5	0.0	-0.2
Crit. Tangential Opening (mm)	0.28	0.4	0.3	0.25
τ_{max} (MPa)	22.9	19.5	15.5	17.1

Table 3.26. Data derived from the Mode I cohesive laws from specimens with moment ratio M_{CFRP}/M_{steel}=-3.4.

Specimen	**MII-1**	**MII-3**	**MII-4**	**MII-5**
Gss (N/m)	3391.9	3261.6	3788.3	4823.5
Go (N/m)	3064.9	0	1040.8	767.2
Gcoh/data (N/m)	327.0	3387	2747.5	4056.3
Gcoh/integrated (N/m)	327.0	3387	2747.5	4056.3
Percentage Difference	0.0	0.0	0.0	0.0
Crit. Normal Opening (mm)	0.05	0.2	0.04	0.25
σ_{max} (MPa)	28	104	240	207

Table 3.27. Data derived from the Mode II cohesive laws from specimens with moment ratio M_{CFRP}/M_{steel}=-3.4.

Specimen	**MII-1**	**MII-3**	**MII-4**	**MII-5**
Gss (N/m)	3423.5	3187.3	3874.4	4912.5
Go (N/m)	0	0	0	0
Gcoh/data (N/m)	3423.5	3187.3	3874.4	4912.5
Gcoh/integrated (N/m)	3423.5	3187.1	3874.4	4912.5
Percentage Difference	0.0	0.0	0.0	0
Crit. Tangential Opening (mm)	0.34	0.38	0.36	0.38
τ_{max} (MPa)	17.9	21.7	22.0	21.9

4. FINITE ELEMENT MODELING OF THE EXPERIMENT

4.1 Finite Element Model description-Preprocessing and Solving

Cohesive zone models present the advantage that they can be introduced in a numerical analysis and simulate the fracture process of an adhesive joint. In this project, the validity of the derived cohesive laws will be assessed with the simulation of the DCB-UBM experiments and the insertion of the cohesive laws using the commercial code ANSYS 12.0.1. The results from the simulation will be compared to the experimental results which will lead to the validation of the procedure.

A numerical model of an adhesive joint that can predict sufficiently its fracture behavior is very important in the level of design; if the comparison between the numerical and experimental data leads to the conclusion that the model is correct, then no more time-spending experiments will be necessary to evaluate a similar structure, since a numerical model can be sufficient. As it has been mentioned in the first Chapter of this work, cohesive zone models have been successfully implemented in finite element models giving a very good prediction of failure analysis (e.g. [16], [17]). In this chapter the finite element model along with the input data and parameters that were used to simulate the DCB-UBM experiment are presented.

The CFRP and steel beams of the DCB-UBM specimen were meshed with plane elements. ANSYS includes contact elements that can be used to simulate interface fracture using the cohesive zone model. These contact elements were used throughout the interface of the steel-CFRP joint and by implementing the derived values of fracture parameters from the experiments, the desired cohesive zone model could be created.

After creating the finite element model, by modifying the applied moments, the different moment ratios used in the experiments can be simulated. In this way, the Mode I and the mixed mode tests were studied by using the cohesive laws derived from the respective experiments.

For the modeling, the built-in design language of the ANSYS program was used. The commands that were used are presented at each step.

4.1.1. Material Properties

The materials used in the simulation were modeled as linear elastic except for the material used for the contact elements. Interface fracture is activated by associating a cohesive zone material model (input with TB,CZM) with the contact elements. The values used are the same as the ones mentioned in Chapter 2.2 and are shown in Table 4.1.

Table 4.1. Properties of Materials used in the finite element model.

	Young's Modulus	Shear Modulus	Poisson's ratio
CFRP	E_1=35GPa	G_{12}=2GPa	v_{12}=0.35
	E_2=E_3=3GPa	G_{23}=G_{13}=1.5GPa	v_{23}=v_{13}=0.3
Steel	E=170GPa	G=65GPa	v=0.3

Interface delamination with contact elements is referred to as debonding. Debonding is modeled with contact elements which are bonded and have a cohesive zone material model defined. ANSYS provides two cohesive zone material models with bilinear behavior to represent debonding: the first model is defined in terms of contact stresses (normal and tangential) while the second model is defined in terms of critical contact separation distances (normal gap and tangential sliding). In this work, the first option has been chosen, which means that stresses were inserted as a material parameter. The material behavior is characterized by linear elastic loading followed by linear softening (see Fig. 4.1). The slope of the curve depends on contact stiffness and a debonding parameter which is defined in terms of material constants. Debonding allows three modes of separation:

- Mode I debonding for normal separation
- Mode II debonding for tangential separation
- Mixed mode debonding for normal and tangential separation

Material softening can lead to convergence difficulties during the solution. In order to facilitate the solution, artificial damping is provided by the program as a parameter that can be used to overcome these problems. After debonding is completed, the surface interaction is governed by standard contact constraints for normal and tangential directions. Frictional contact is used if friction is specified for the contact elements.

The cohesive zone material model with bilinear behavior is defined as:

$$P = K_n u_n (1-d) \tag{4.1}$$

$$\tau_y = K_t u_y (1-d) \tag{4.2}$$

$$\tau_z = K_t u_z (1-d) \tag{4.3}$$

where:

P = normal contact stress (tension)

τ_y = tangential contact stress in y direction

τ_z = tangential contact stress in z direction

K_n = normal contact stiffness

K_t = tangential contact stiffness

u_n = contact gap

u_y = contact slip distance in y direction

u_z = contact slip distance in z direction

d = debonding parameter

The axes that are referred above can be seen in Figure 4.3.

So, the shape of the cohesive law that it is used by the ANSYS program is bilinear as it is derived from Equations 4.1 to 4.3. In our case, equations 4.1 and 4.2 are of interest since normal and tangential stresses are present and the debonding parameter d is defined as [24]:

$$d = \left(\frac{\Delta_m - 1}{\Delta_m} \right) \chi \tag{4.4}$$

with d=0 for $\Delta_m \leq 1$ and $0 \leq d \leq 1$ for $\Delta_m > 1$ and Δ_m and χ are defined below.

$$\Delta_m = \sqrt{\Delta^2{}_n + \Delta^2{}_t} \tag{4.5}$$

$$\Delta_n = \frac{u_n}{\overline{u}_n} \tag{4.6}$$

$$\Delta_t = \frac{u_t}{\overline{u}_t} \tag{4.7}$$

$$\chi = \left(\frac{u^c{}_n}{u^c{}_n - \overline{u}_n} \right) = \left(\frac{u^c{}_t}{u^c{}_t - \overline{u}_t} \right) \tag{4.8}$$

The constraint on χ that the ratio of the contact gap distances is the same as the ratio of tangential slip distances is enforced automatically by appropriately scaling the contact stiffness values.

The Mode I cohesive law used by the program is shown in Figure 4.1. The Mode II cohesive law is of the same shape as the Mode I with the dimensions used are the tangential slip opening u_t instead of the normal opening u_n as the x-axis, and the tangential stress τ_y instead of the normal stress P as the y-axis.

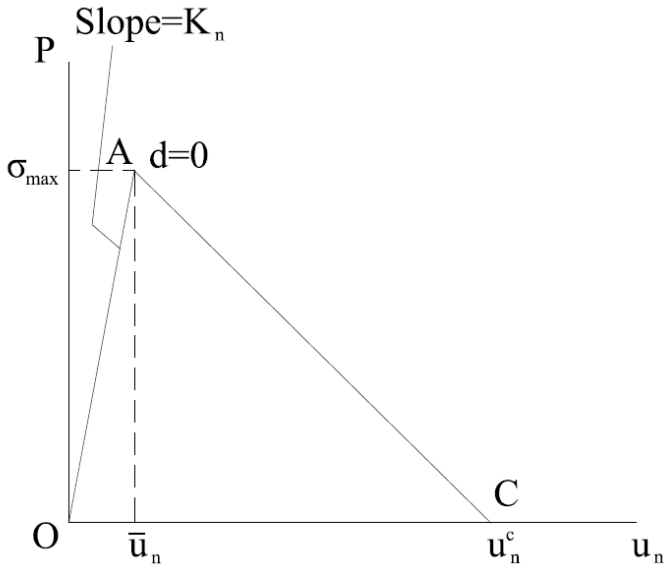

Figure 4.1. The Mode I cohesive law used in the finite element model analysis.

The cohesive law curve in Figure 4.1 shows linear elastic loading (OA) followed by linear softening (AC). The maximum normal contact stress is achieved at point A with a normal opening value equal to $\overline{u}_n$ (for tangential opening $\overline{u}_t$). Debonding begins at point A and is completed at point C when the normal contact stress reaches zero value; any further separation occurs without any normal contact

stress. The area under the curve OAC is the energy released due to debonding, called the critical fracture energy.

For mixed mode debonding, both normal and tangential contact stresses contribute to the total fracture energy and debonding is completed before the critical fracture energy values are reached for the components. Therefore, a power law based energy criterion is used to define the completion of debonding [24]:

$$\left(\frac{G_n}{G_{cn}}\right)+\left(\frac{G_t}{G_{ct}}\right)=1 \tag{4.9}$$

where :

$$G_n=\int P du_n \tag{4.10}$$

$$G_t=\int \tau_t du_t \tag{4.11}$$

are, respectively, the normal and tangential fracture energies.

To model bilinear material behavior with tractions and critical fracture energies, the ANSYS command TB,CZM is used. The following material constants have to also be input with the TBDATA command:

Table 4.2. Input parameters for the definition of the cohesive zone material model.

Constant	Symbol	Meaning
C1	σ_{max}	maximum normal contact stress
C2	G_{cn}	critical fracture energy for normal separation
C3	τ_{max}	maximum equivalent tangential contact stress
C4	G_{ct}	critical fracture energy for tangential slip
C5	η	artificial damping coefficient
C6	β	flag for tangential slip under compressive normal contact stress

The following is an example of how a cohesive zone material is defined with the TB and TBDATA commands:

```
TB,CZM,,,,CBDE   ! bilinear behavior with tractions and contact stresses
TBDATA,1,C1,C2,C3,C4,C5,C6
```

So, it has been seen that the parameters needed for the cohesive zone material model are the critical fracture energies for Mode I and Mode II and the maximum normal and tangential stresses. These data are obtained from the measured cohesive laws, presented in Chapter 3.4. Two cohesive laws were investigated for the Mode I tests and one more for the mixed mode tests.

- *Mode I cohesive law*

The cohesive laws derived from specimens MI-1 and MI-2 were chosen for the study of the Mode I experiments. Specimen MI-1, as it has been seen in Chapter 3.4, presented higher fracture toughness and maximum stress values than the specimen MI-2, so the cohesive laws derived from both these specimens will be examined for a more complete analysis. In Case 1 the data from specimen MI-1 are used while in Case 2 the data from specimen MI-2. The data obtained from the experiments that were inserted into the model are shown in the following Table 4.3.

Table 4.3. Input parameters for the Mode I cohesive law used to simulate the Mode I tests.

	Case 1	**Case 2**
Specimen	MI-1	MI-2
G_{cn} (N/m)	746	571.7
σ_{max} (MPa)	19.3	3.4

For the material properties to be fully defined, input for the Mode II opening had to be inserted also. Since, there were no data for that in Mode I experiments, the Mode II data from specimen MM-4 were used seen in the following Table 4.4. However, the values that will be inserted for the Mode II opening will not affect the results significantly since this is a Mode I dominated test.

Table 4.4. Input parameters for the Mode II cohesive law used to simulate the Mode I tests (both cases).

G_{ct} (N/m)	1784
τ_{max} (MPa)	17.1

- *Mixed mode cohesive law*

For the third case that will be examined, the cohesive law derived from specimen MM-4 is chosen for evaluation since its dimensions are of an average value compared to the cohesive laws derived from the rest of the specimens. The data that were used as input in the finite element model are presented in Table 4.5.

Table 4.5. Input parameters for Mode I and Mode II cohesive laws used to simulate the mixed mode tests.

Case 3	
G_{cn} (N/m)	1666.5
σ_{max} (MPa)	18.1
G_{ct} (N/m)	1784
τ_{max} (MPa)	17.1

4.1.2. Geometry of the model

The general geometry of the model that was created is shown in Figure 4.2 along with the dimensions used. A two-dimensional model was used for simplicity and save of computational time, since the DCB-UBM specimen does not present a complex geometry. The adhesive was not modeled; instead contact elements were meshed at the interface of the two adhered materials representing the cohesive law that was derived from the experiments. Moreover, the change of the thickness of the DCB-UBM specimen was not modeled for reasons of simplicity; the specimen was modeled having a uniform thickness of the steel and CFRP beam.

For the correct definition of the geometry of the model, the density of the desired mesh has to be taken into account. The meshed areas around the interface of the two materials should be more dense than the areas at the rest of the model. This means that the model will be divided into different areas according to the mesh density. For the creation of areas, the first step is to create keypoints at the edge of the areas that will be the base of the model. Moreover, two extra keypoints were created near the cracked edge of the specimen so that the moments can be applied; this will be explained later in details.

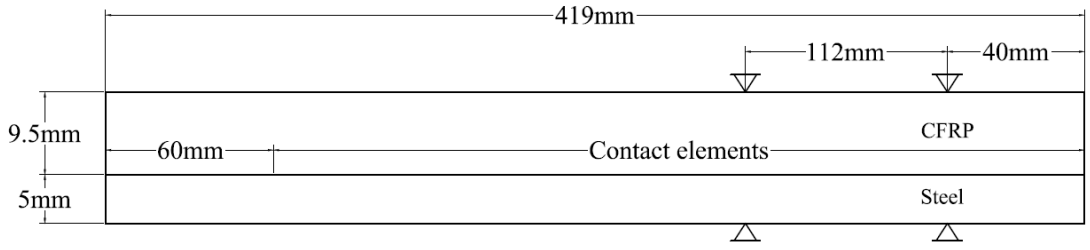

Figure 4.2. Geometry and boundary conditions of the created finite element model of the DCB-UBM specimen.

In Figure 4.3 the created keypoints are presented.

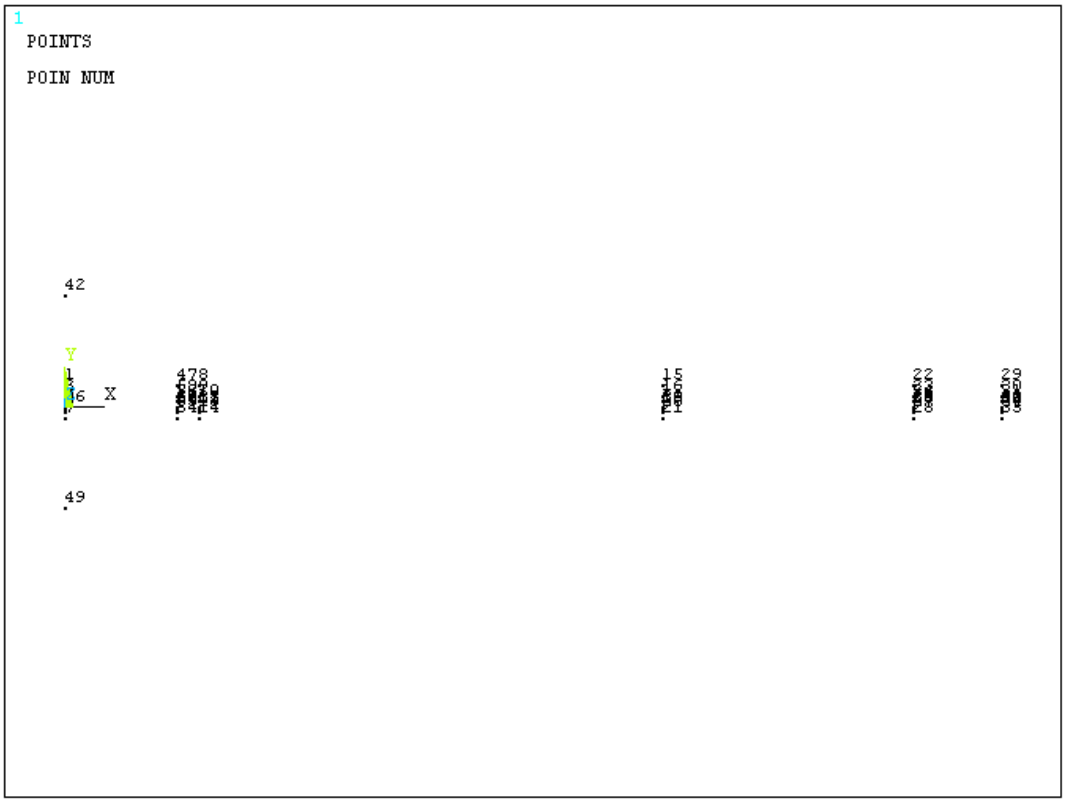

Figure 4.3. Created keypoints of the two-dimensional model.

The commands used for the definition of the keypoints are presented below. The values were inserted in meters. The x-axis runs through the interface of the two materials.

K,1,0,0.0095
K,2,0,0.00475
K,3,0,0.002375
…
K,59,0.0499,0.00475
K,60,0.0499,0

Before creating areas, lines had to be defined first based on the created keypoints. These lines will help the meshing of the model later. The lines that were created are shown in Figure 4.4.

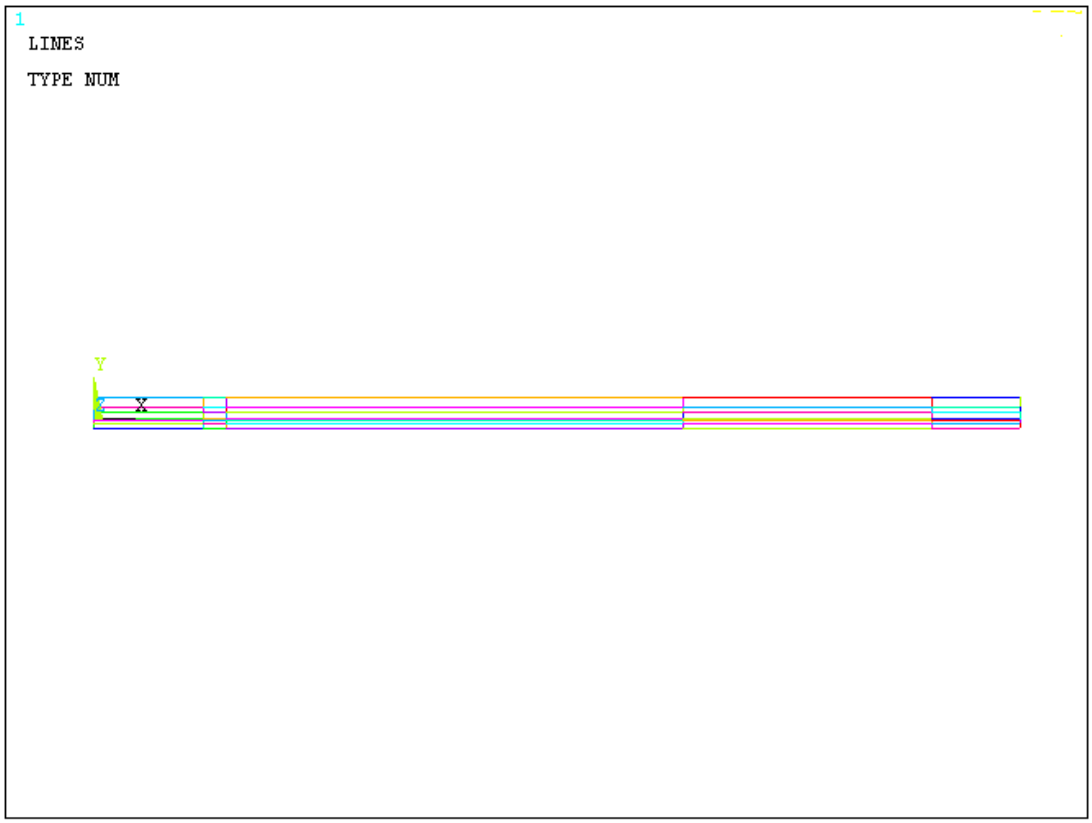

Figure 4.4. Lines that were created based on the keypoints.

A part of the commands that were used for the definition of the lines is presented below. The numbers represent the keypoints at the edge of the created line:

```
L,     1,     2
L,     2,     3
L,     3,     4
…
L,    48,    53
L,    49,    52
L,    50,    51
```

The next step was the creation of the areas, presented in Figure 4.5. The commands used are:

```
A,1,2,59,47
A,2,3,58,59
A,3,4,57,58
…
A,26,27,34,33
A,27,28,35,34
```

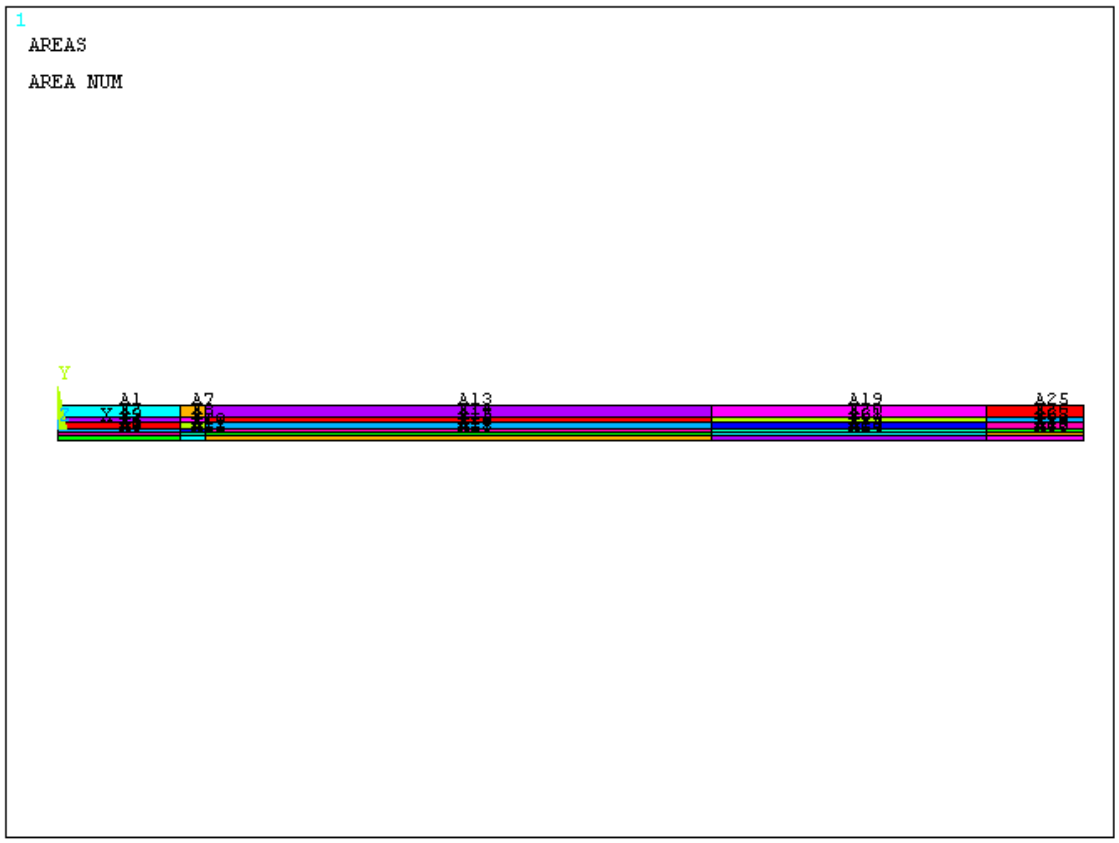

Figure 4.5. Areas representing the DCB-UBM model.

Next, before the meshing of the model, the lines that were created before had to be divided so that the element size can be defined based on the line divisions. The most important part of the model is the interface that will be meshed with contact elements. So, before a mesh size was chosen, its validity had to be checked. An optimization procedure was made in order to find an optimum contact element length. Three case studies were performed: for contact element length 2mm, 1mm and 0.5mm, meaning the creation of 180, 359 and 718 contact elements across the interface respectively. The same geometry was used and by applying a 0.05mm displacement as a boundary condition at keypoint 1 and -0.05mm at keypoint 7, crack propagation was simulated. Reaction forces were measured at those keypoints as a result to check which value of element length converges. The results are presented in Table 4.6.

Table 4.6. Reaction forces values taken from the element length optimization.

	Reaction Force (N)	
Element Length	Keypoint 1	Keypoint 7
2mm	563.654	-359.899
1mm	598.228	-338.427
0.5mm	599.029	-337.362

It can be extracted from Table 4.6 that results converge for element length 1mm and 0.5mm. Since the computational time increased significantly with the 0.5mm element length, the final value chosen for the contact element of the DCB-UBM model is 1mm.

The commands called for the division of the lines are presented below.

```
LSEL,,,,1,31,6
LESIZE,ALL,,,4
LSEL,,,,2,32,6
LESIZE,ALL,,,2
LSEL,,,,51,57,1
LESIZE,ALL,0.001
…
LSEL,,,,6,36,6
LESIZE,ALL,,,2
```

Before meshing, the element that will be used had to be defined. The element chosen for the meshing of the two beams is the PLANE182. This is used for 2-D modeling of solid structures. The element can be used as a plane element (plane stress, plane strain or generalized plane strain). It is defined by four nodes having two degrees of freedom at each node: translations in the nodal x and y directions. The element has plasticity, hyperelasticity, stress stiffening, large deflection, and large strain capabilities. The geometry of the element is shown in Figure 4.6.

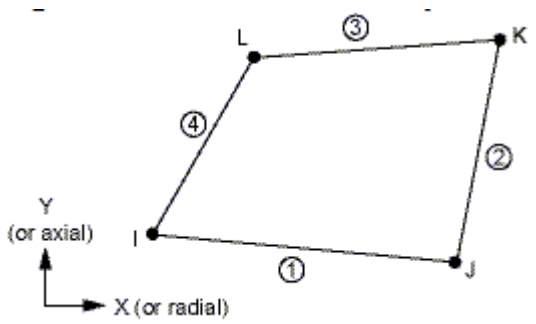

Figure 4.6. PLANE182 geometry.

In our case, the plane stress with thickness option was chosen. The thickness that was inserted as input was 30mm, the width of the DCB-UBM specimens. The command called for choosing the element and defining the plane stress with thickness option was:

```
ET,1,PLANE182
KEYOPT,1,3,3
R,1,0.03,
```

The meshing process can now be performed, having defined the element, the areas and the line division. The commands used to create the mesh are shown below. Before each command, a material was chosen for each area that will be meshed.

```
MAT,1
AMESH,1,25,6
AMESH,2,26,6
AMESH,3,27,6
MAT,2
AMESH,4,28,6
AMESH,5,29,6
AMESH,6,30,6
```

The produced mesh is presented in Figure 4.7.

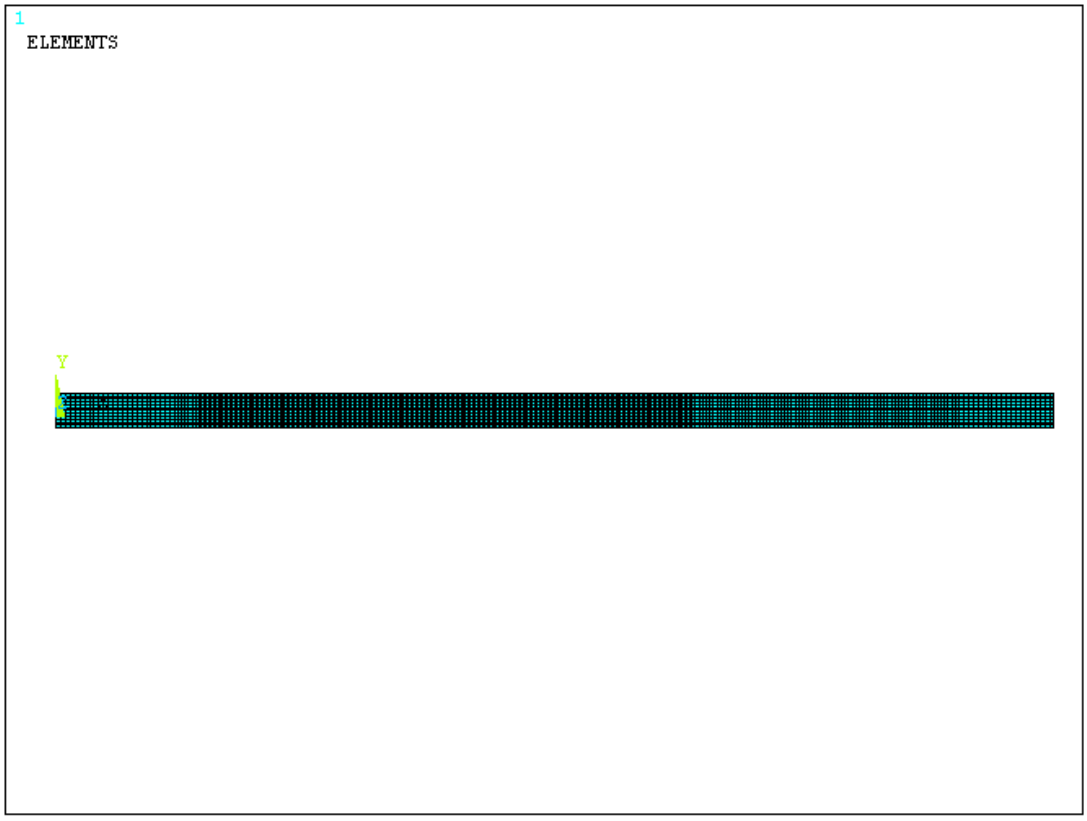

Figure 4.7. Element mesh of the DCB-UBM model.

The contact elements have not been yet created. The built-in contact wizard of the ANSYS program was used to create these elements. A flexible surface-to-surface contact was chosen with the option "Bonded (always)" to bring the desired surfaces of the two beams together. The CFRP surface was chosen as the target surface as this material is less stiff than the steel. The cohesive zone material was chosen for the elements that are to be created. The created elements are not shown in the graphic interface of the program, so they cannot be presented.

Using the contact wizard a rigid constraint was also defined in order to facilitate the application of the moments on the model. In the experiment, pure moments were applied on the specimen, so a way had to be found to apply pure moments on the two-dimensional model that has been created. The two extra keypoints 42 and 49 that were defined outside the meshed areas were used as the free

keypoints for the node-to-surface rigid constraint that was needed for the loading of the model. Each one of these two keypoints was rigidly constraint with the nodes of the line at the cracked edge of the specimen as shown in Figure 4.8. Keypoint 42 was constrained to the CFRP beam and keypoint 49 to the steel beam.

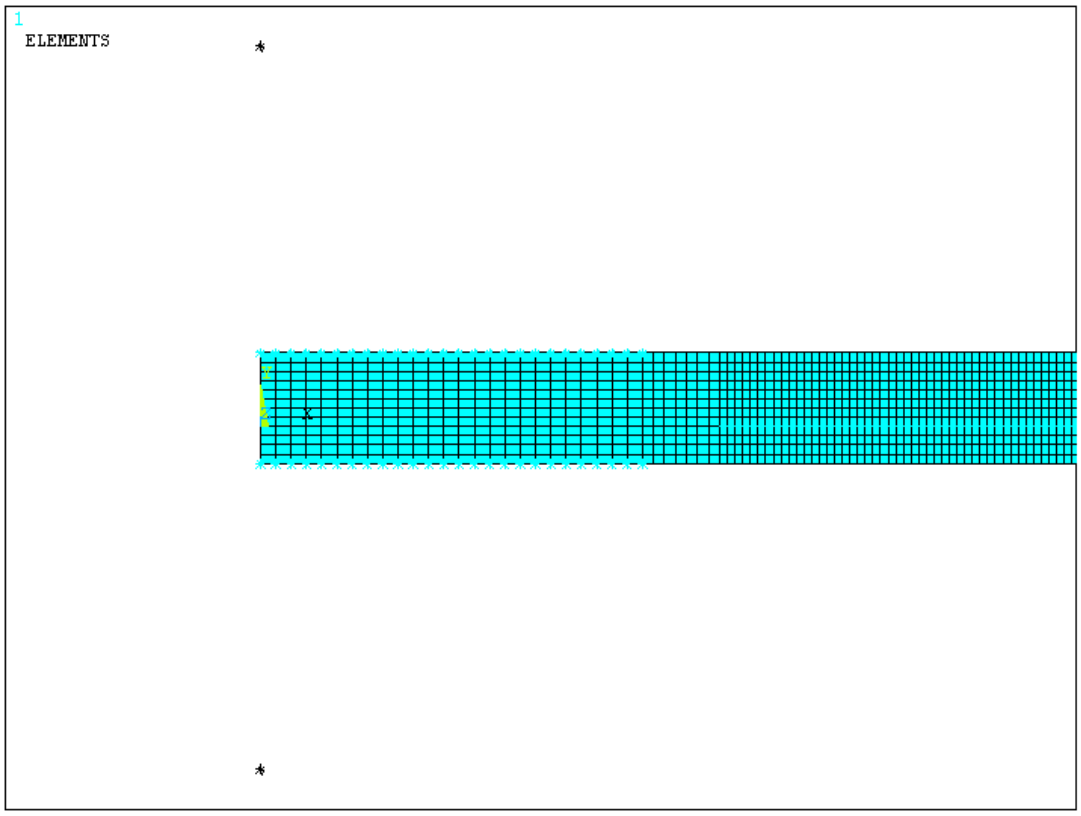

Figure 4.8. Rigid constraint of the two keypoints (shown as black stars) with lines at the cracked end of the specimen (shown as blue stars on the upper and lower edge of the model).

The degrees of freedom that were constrained between the keypoints and the nodes of the lines were the displacements at the x and y-axis along with the rotation around the z-axis. To better simulate the loading procedure of the experimental set-up, these lines were of the same length as the aluminum part that were used for the loading of the DCB-UBM specimen during the experiments.

4.1.3. Moment application and boundary conditions

Having created the model, the definition of the loads and the boundary conditions is next. The model was fixed at four keypoints; these are shown in Figure 4.9 as also in Figure 4.2. These keypoints represent the location where the supports of the DCB-UBM specimens were located during the experiments. The commands called for the definition of the boundary conditions are shown below:

```
DK,15,ALL,0
DK,22,ALL,0
```

DK,21,ALL,0
DK,28,ALL,0

These commands mean that all the degrees of freedom of keypoints 15,21,22 and 28 are constrained to zero.

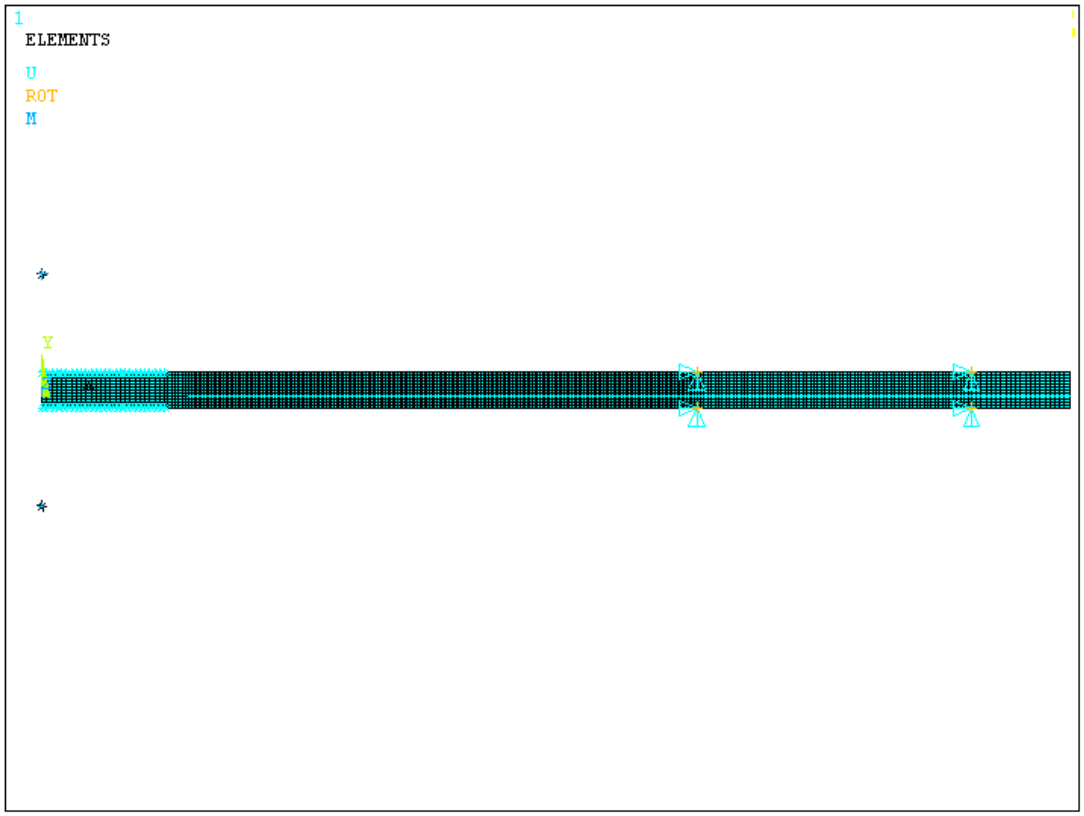

Figure 4.9. The full finite element model, showing all the plane elements, the boundary conditions and constraints.

The loading of the model will be achieved through keypoints 42 and 49 that were constrained with the lines of the model as was mentioned before. The values of the moments will vary depending on the cohesive zone material studied. Since, the experiments may have presented a small variation from the desired moment ratio, the load results from the experiment that each cohesive law was derived will be used. The values of the applied moments for each of the three cases are presented in Table 4.7. Keypoint 42 applies load to the CFRP beam while keypoint 49 applies load to the steel beam. The moment ratio of the model is also presented in this table along with the average moment ratio of the respective experiment.

Table 4.7. Moments applied for each case that was studied and values of the moment ratios of the model and the respective experiment.

	Case 1	Case 2	Case 3
M_{CFRP} (Nm)	51.5	55.4	100.0
M_{Steel} (Nm)	26.0	26.0	-18.0
M_{CFRP}/ M_{Steel} - Model	1.98	2.14	-5.56
M_{CFRP}/ M_{Steel} - Experiment	1.98	2.14	-5.54

The commands used for the definition of the moments are shown below for Case 1. The same commands with the respective load values were called for the other cases. The program considers positive the counter-clock wise direction, so th

```
FK,42,MZ,-51.5
FK,49,MZ,26
```

The contact constraint that has been applied between the keypoints and the lines will transmit the pure moments to the model. The final step that follows before taking the results is defining the solver parameters.

4.1.4. Solving the model

The solving of the model was done using the non-linear assumption by choosing the large-displacement static option. The program then performs a non-linear static analysis which includes large deformations and also takes into account any material non-linearities, which is our case; the cohesive zone material model is not a linear material model and a non-linear analysis is needed to get a solution.

The non-linear analysis consists in applying the boundary conditions and loads gradually and calculating at the end of each time step all the stresses and deformations of the model. In our case, a proper time step size division had to be determined that will yield valid results. The time at the end of the analysis was chosen equal to one and then three different time step division runs were made for the optimization of the parameters. These parameters of each run are shown in Table 4.8.

Table 4.8. Parameters of the time step optimization runs.

	Initial Time Step Size	Minimum step size	Maximum step size
Run 1	1.00E-03	1.00E-09	1.00E-03
Run 2	1.00E-04	1.00E-10	5.00E-04
Run 3	1.00E-05	1.00E-10	1.00E-03

The convergence of the runs was checked by the resulting rotation of keypoints 42 and 49 at a specific time, after the crack had started to propagate using the load values of Case 1.

Table 4.9. Rotation results of the optimization runs.

	Rotation at time=0.879 (rad) for Case 1 load values.	
	Keypoint 42	Keypoint 49
Run 1	-8.69E-02	-5.06E-02
Run 2	-8.74E-02	-5.10E-02
Run 3	-8.67E-02	-5.05E-02

The results present a maximum difference of 1% meaning that the solution is reached for all the parameters used. Thus, the parameters of Run 1 are chosen since the solution is reached with the least computational time. The commands used to define the non-linear analysis parameters are presented below.

```
ANTYPE,0
NLGEOM,1
TIME,1
DELTIM,0.001,0.000000001,0.001
LNSRCH,1
```

4.2. Post-processing of the model

4.2.1. Case 1

The post-processing of the model consists in obtaining all the results after the solution has been done that can lead to useful conclusions. The validity of the solution can first be checked by plotting the deformed shape of the model during the procedure along with the stress field that is created. This can be done using the contour plot command which plots the stress field on the model using different color for areas with different stress levels. The behavior of the model can then be evaluated and if it differs from the expected response, the causes of this differentiation can be located more easily.

In this section, the response of the Case 1 model is evaluated. This is a simulation of a Mode I experiment, using the cohesive law derived from specimen MI-1. In Figure 4.10, a contour plot of the Von Mises stress on the deformed model at time equal to 0.65 is presented. This means that the moment that has been applied to the model is 65% of the nominal values presented in Table 4.7. The stress field is plotted as expected, showing higher stress concentration around the crack tip. The steel and CFRP beams separate from each other as can be seen in the deformed shape of the model.

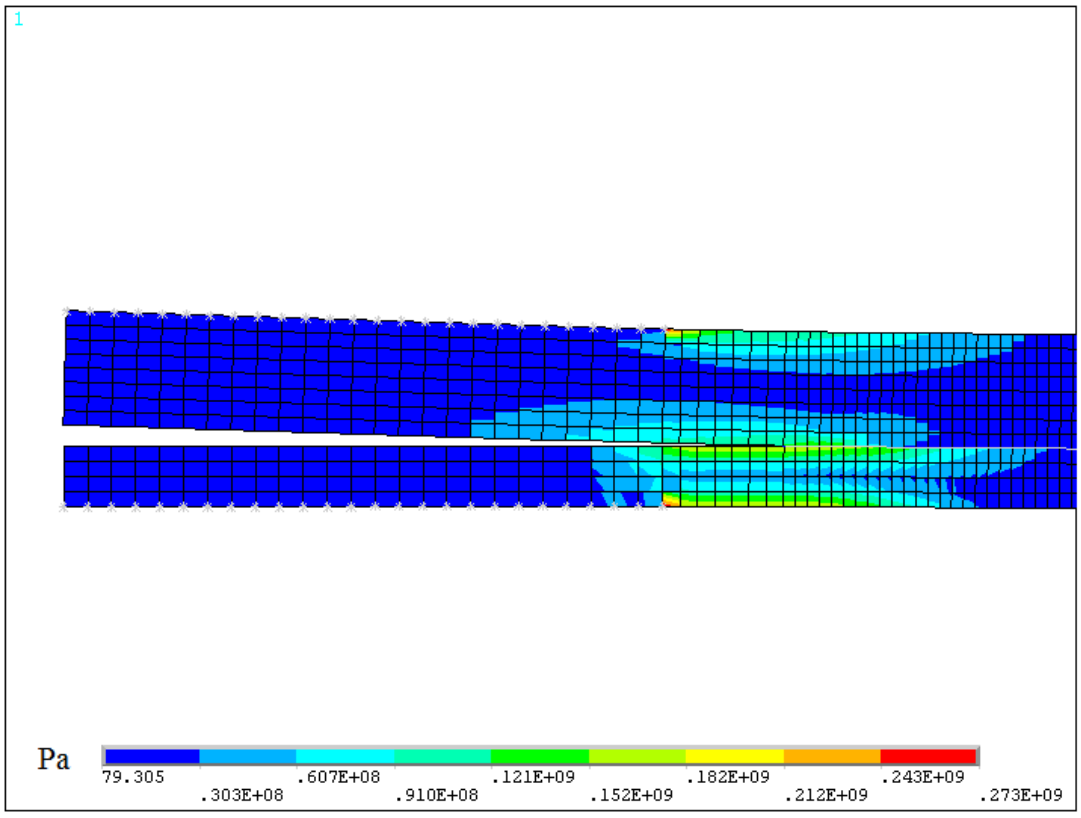

Figure 4.10. Stress contour of the deformed Case 1 model at time=0.65.

The most important graph is presented next. The comparison between the finite element model and the experiments will be done from the plot of the load versus normal opening. The load refers to the applied load of the wire during the DCB-UBM tests, so the applied moments have to be transformed to load values. The derivation of the load value of the model can be made by dividing the moment by the righting arm that was used at each beam at the experiments. This yields the following Figure 4.11 where the derived curve from the model is plotted along with the respective curve resulting from the experiments.

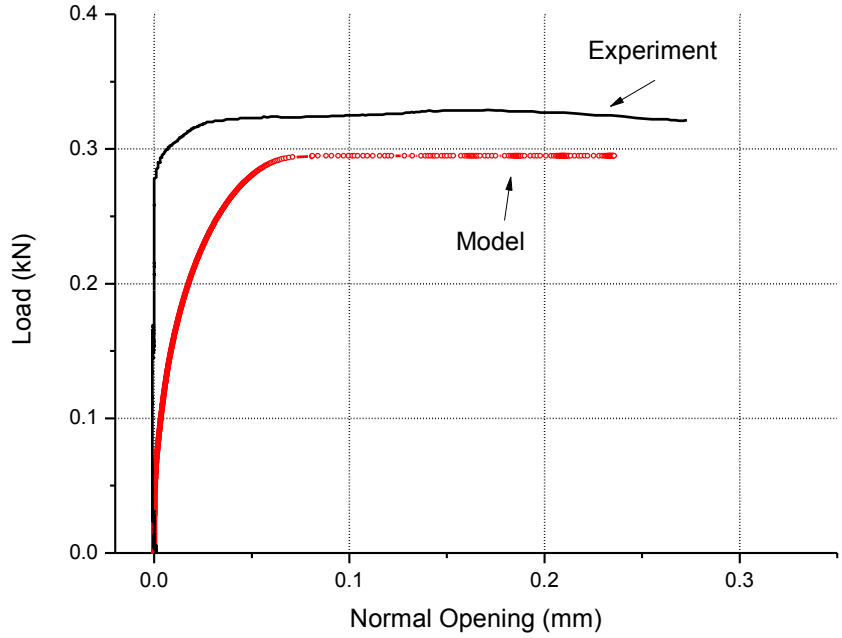

Figure 4.11. Load versus normal opening of the Case 1 model and of the MI-1 specimen.

The shape of the curve obtained from the finite element model presents the expected behavior. Firstly, the load increases with increasing normal opening in a non-linear fashion due to the non-linear nature of the cohesive zone material and the different elastic properties of the two beams. Then, as the crack starts to propagate at about δ_{nc}=0.06mm, the load reaches a plateau and the normal opening increases significantly while the load remains at the steady value of 0.295kN. The experimental load value reaches a steady-state value around 0.33kN at a critical normal opening 0.05mm. This means that the prediction between the model and the experiment of the peak load value presents a 10% difference while the critical opening is about the same for the two curves. The results of the Case 1 and Case 2 simulations will be discussed together later on.

In order to evaluate how close to Mode I the simulation was, both the normal and tangential openings were calculated at the initial crack tip. In Figure 4.12 the load versus the tangential opening is presented using the same axes as in Figure 4.11 for a better comparison of the data. It can be seen that the tangential opening takes much smaller values than the normal opening. The normal to tangential opening ratio

reaches a value of $\frac{\delta_n}{\delta_t} = 25$. This means that a good approximation of Mode I opening was achieved.

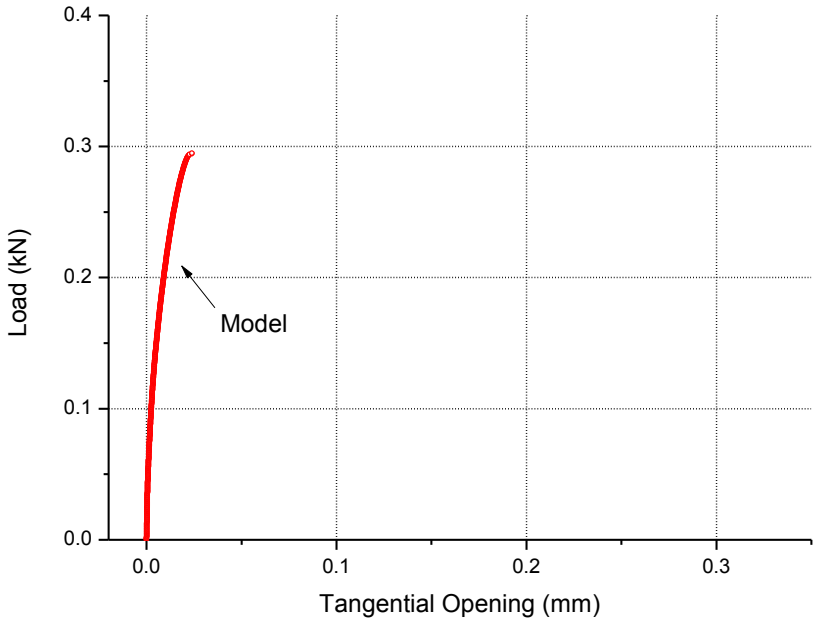

Figure 4.12. Load versus tangential opening of the Case 1 model and of the MI-1 specimen.

In the following graphs, the total stress throughout the interface is presented; this means the sum of the peel and shear stress that is calculated on the contact elements. Thus the development of the cohesive zone can be evaluated. First at time equal to 0.1, the cohesive zone is starting to develop as seen in Figure 4.13. A peak stress is reached at the edge of the initial crack followed by a stress decrease. This part of the cohesive zone is defined by the linear elastic loading part (OA) of the cohesive law used in the finite element model shown in Figure 4.1.

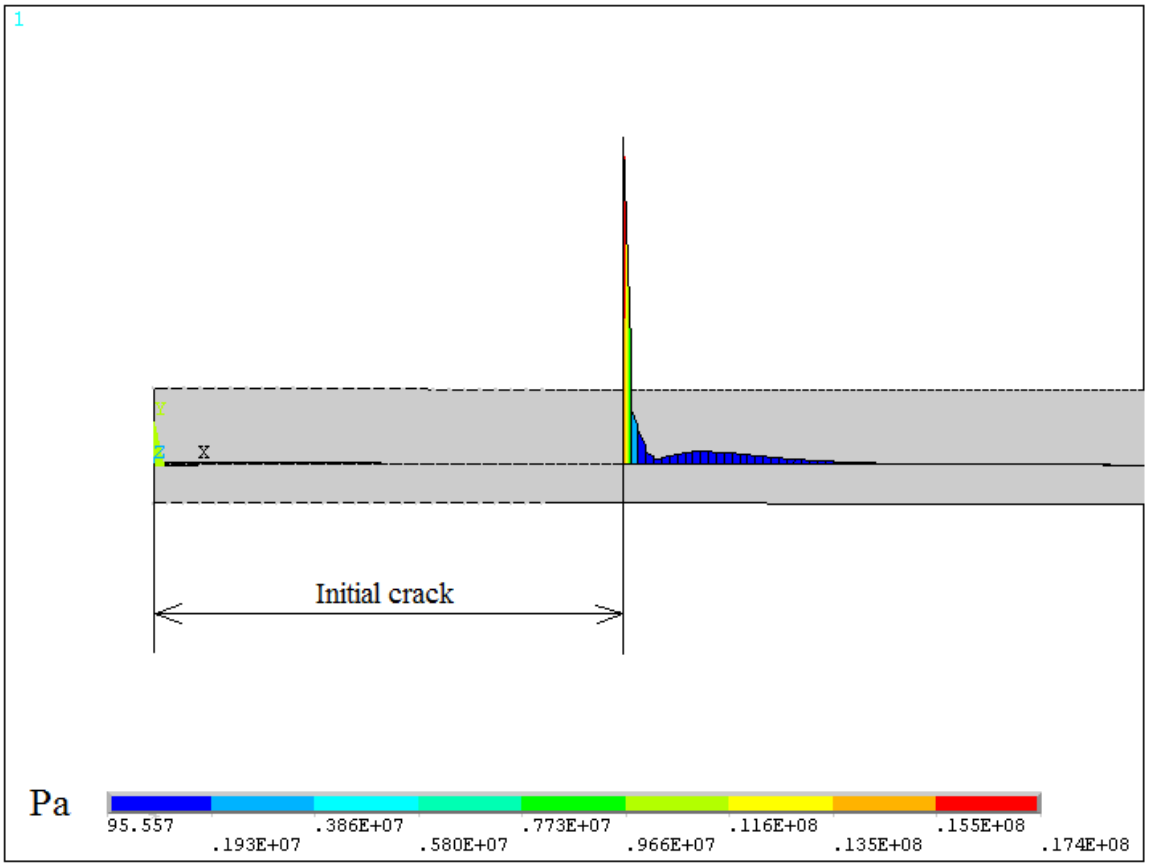

Figure 4.13. Distribution of total stress at the interface at time equal to 0.1.

In the following Figure 4.14 representing the model at a time equal to 0.7, the cohesive zone has developed more. The part defined by the linear softening of the cohesive law (AC) (see Figure 4.1) can now be seen where the stress is decreasing.

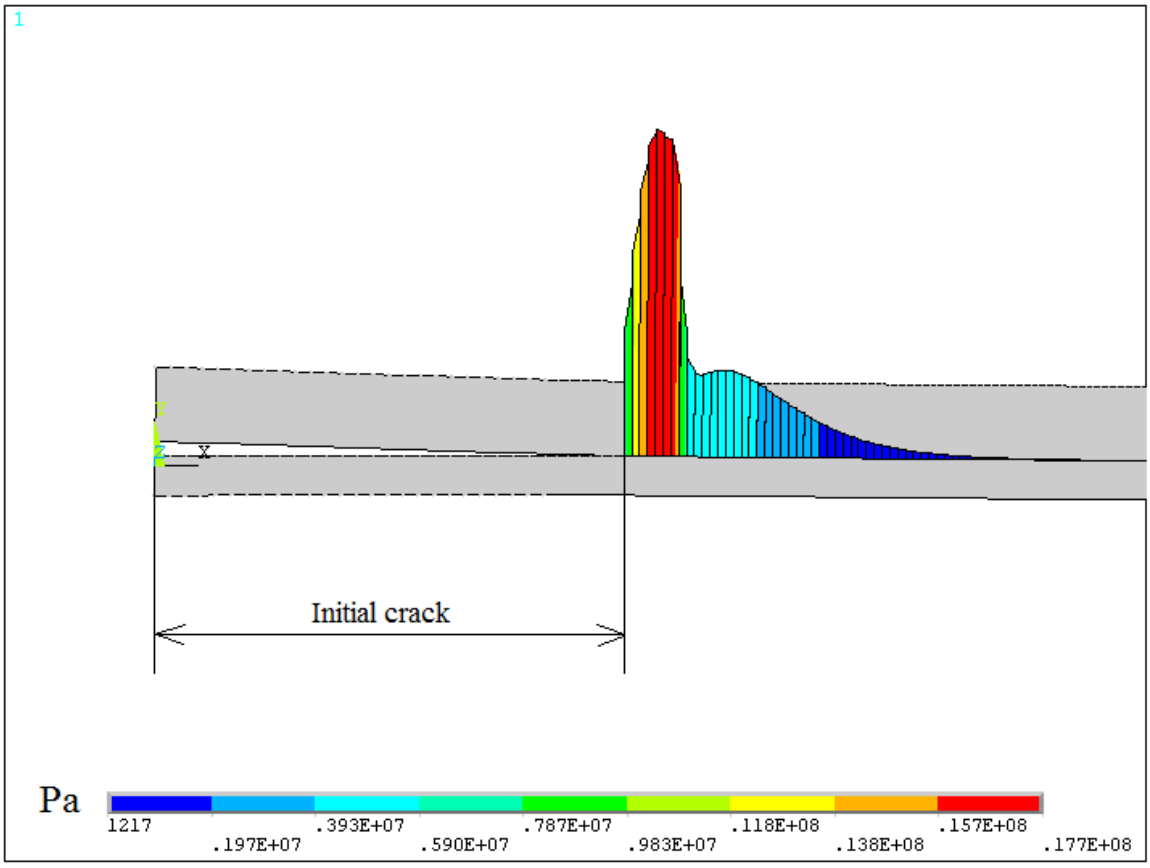

Figure 4.14. Distribution of total stress at the interface at time equal to 0.7.

However, the zone has not yet been fully developed, which means that the crack has not propagated still. The fully developed cohesive zone can be seen in Figure 4.15 where the model is depicted for time equal to 0.737. Three different parts of the model can be distinguished: the first part with no stress, presenting a length of 7mm where the crack has propagated through. The second part is defined by the linear elastic loading of the cohesive law and the stresses increase to a peak. The length of this part is 6mm. Finally, the third part is defined by the linear softening part of the cohesive law where the stresses decrease to zero gradually. The length of the third part is 43mm, so the cohesive zone has a total length of 49mm.

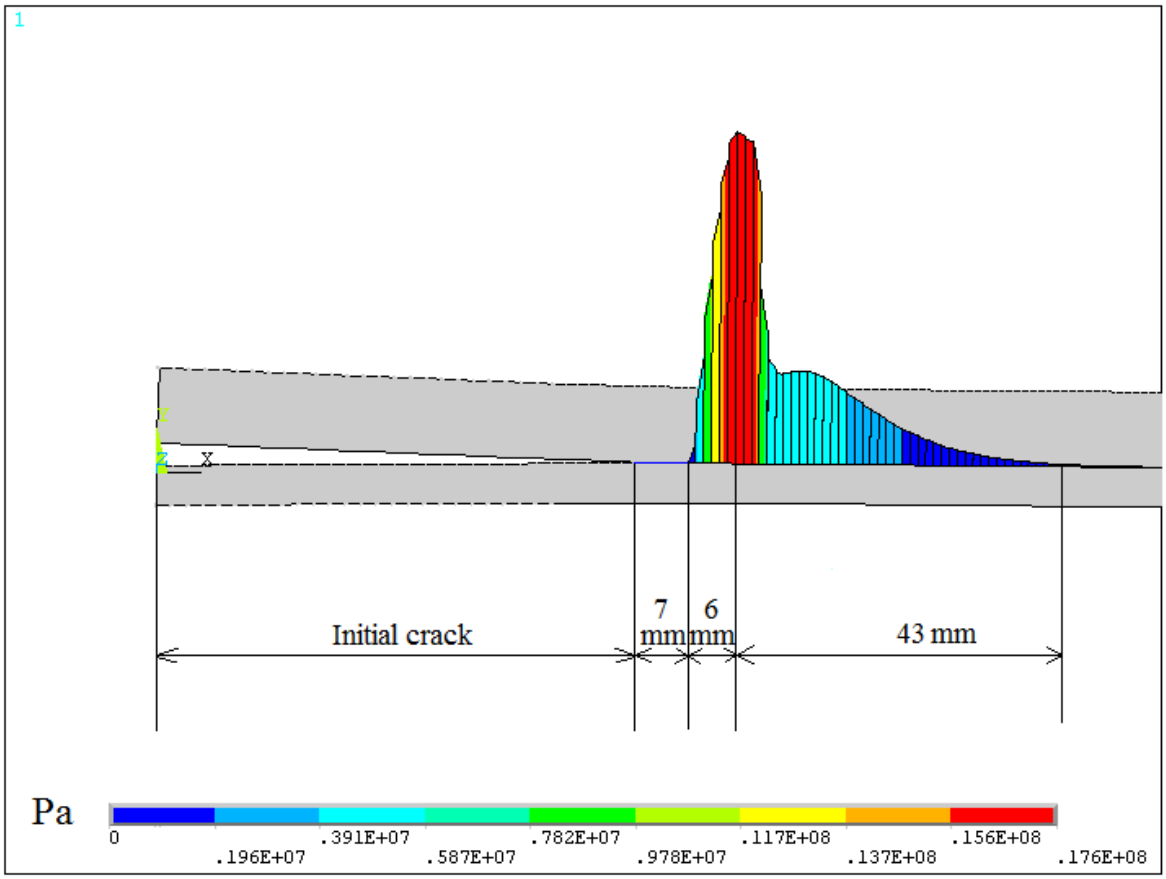

Figure 4.15. Typical fully developed cohesive zone: the length of the crack propagation is shown along with the two parts of the cohesive zone of the Case 1 model.

4.2.2. Case 2

The response of the Case 2 model follows. This is a Mode I experiment simulation of specimen MI-2. The details of the cohesive material model used can be seen in Tables 4.3 and 4.4. In Figure 4.16 the deformed shape of the model is presented with a von Mises stress contour. The response of the model is expected and similar to the Case 1 model. The area around the crack edge presents higher stress values while the two beams separate from each other.

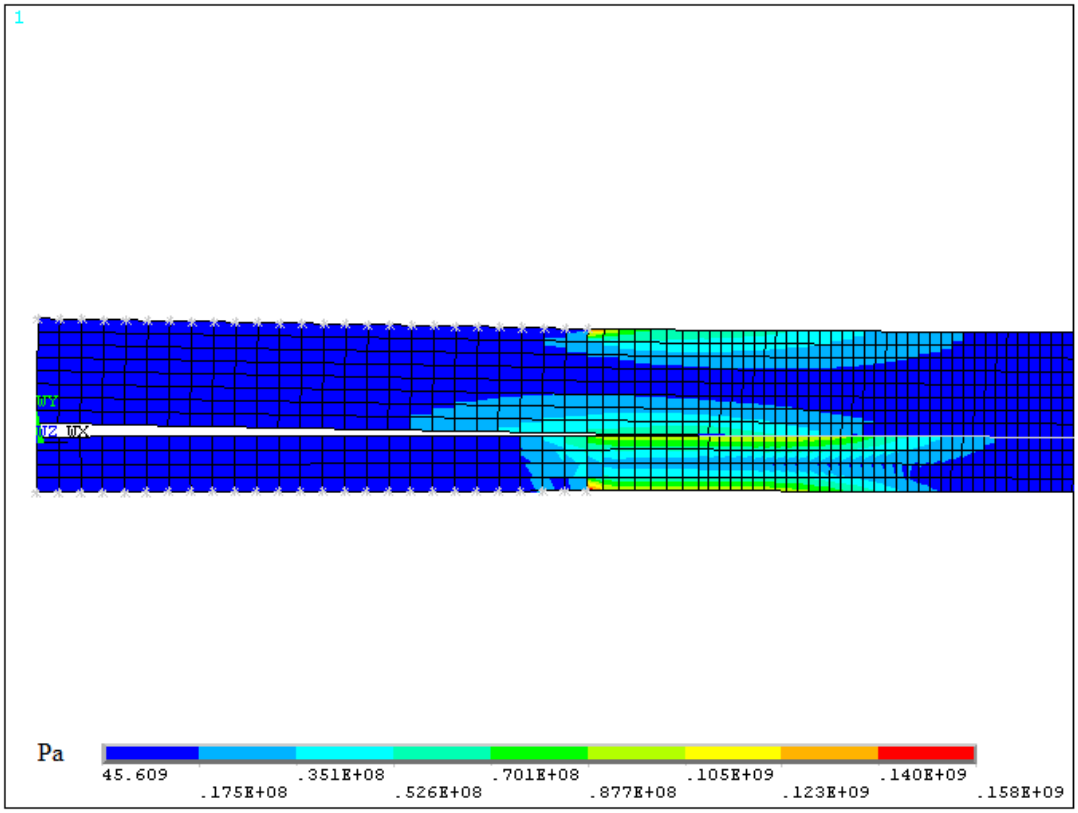

Figure 4.16. Stress contour of the deformed Case 2 model at time=0.5.

The prediction of the load versus the normal opening of the model and the experimental curve of the specimen is presented in Figure 4.17. The normal opening increases with the increase of the load reaching an almost steady value at 0.26kN. The steady-state value attained during the experiment was of a value around 0.3kN, so there is a deviation of 13.5% between the model and the experiment. The shape of the curve however does not represent accurately the response of the DCB-UBM specimen since the critical normal opening of the model δ_{nc}=0.3mm is not very close to the critical normal opening of the MI-2 specimen δ_{nc}=0.08mm.

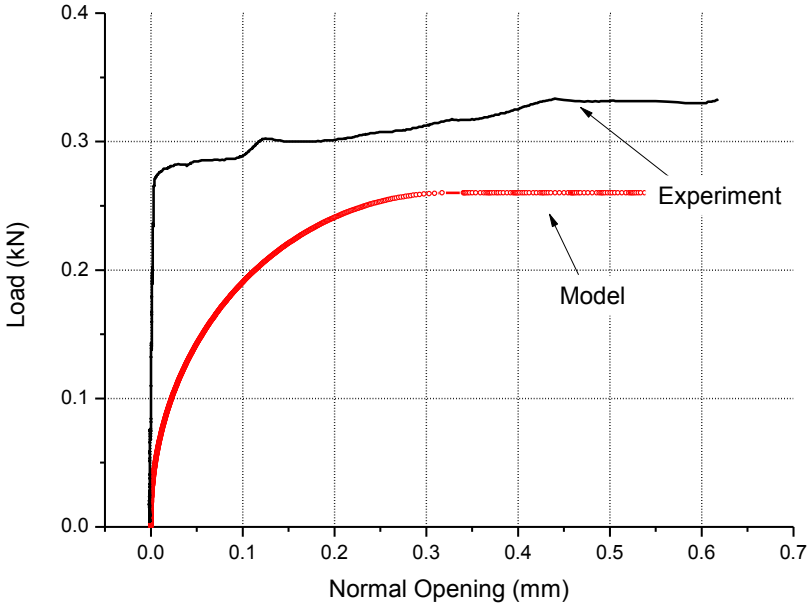

Figure 4.17. Load versus normal opening of the Case 2 model and of the MI-2 specimen.

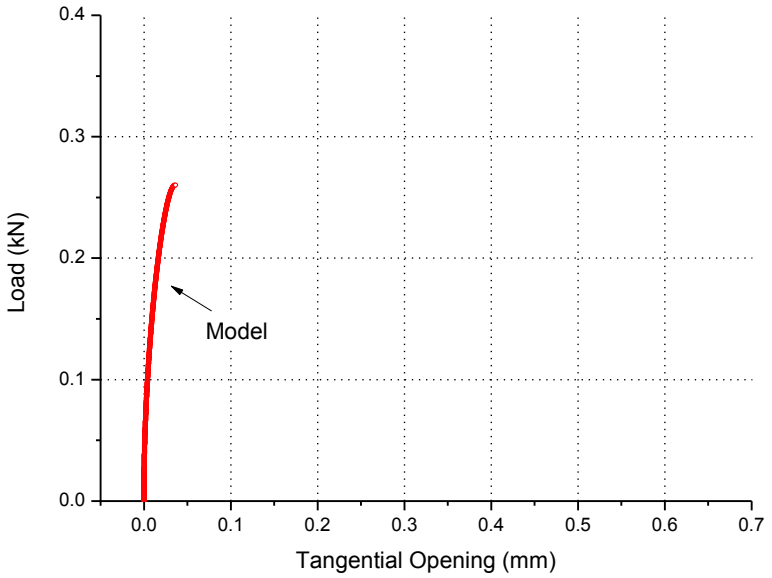

Figure 4.18. Load versus tangential opening of the Case 2 model and of the MI-2 specimen.

The load versus the tangential opening graph is presented in Figure 4.18 in order to evaluate how close to pure Mode I the model was, using the same axes as in Figure 4.17 for a better comparison of the data. The tangential opening, as in Case 1,

takes smaller values than the normal opening with an average ratio $\frac{\delta_n}{\delta_t} = 10$. This means that the normal opening is much higher than the tangential opening and the experiment can be called Mode I dominated.

It can be derived from the figures above that the parameters that were used in Case 1 give a better prediction of the experiment since the critical opening and the peak value of the load were better calculated in the previous case. Since the parameters of the cohesive law of the Case 1 study were derived from the specimens with the higher values of the parameters used it can be said that the results from these specimens should be considered more correct.

The deviation that is presented between the experiments and the models can be attributed to several reasons. The calculation of the energy release rate that was performed in the previous chapter includes many assumptions that can affect the results. Two of the main assumptions that were made for this project are: the adhesive joint was considered as a bi-material and that linear elastic fracture mechanics were valid. Moreover, the cohesive laws derived from the experiments were assumed as decoupled and the traction-separation laws that were implemented in the finite element model presented an idealized shape. Additionally, the geometry of the specimen that was used in the simulations was not exactly the same as of the specimens used in the experiments. An average geometry was used for the finite element model neglecting the adhesive layer while the DCB-UBM specimens that were manufactured presented a divergence in their geometric characteristics as it was analyzed in Chapter 2. All these assumptions were made in order to facilitate the procedure. Better results closer to the experimentally measured could have been obtained from the model if some of these assumptions were excluded from the procedure.

The fully developed cohesive zone of the model can be seen in Figure 4.19. The model at time equal to 0.865 is depicted in this graph. The crack has propagated 12mm. The first part of the cohesive zone defined by the linear elastic loading of the cohesive law has a length of 25mm while the second part of the zone defined by the linear softening part of the cohesive law has a length of 50mm. The cohesive zone has a total length of 75mm.

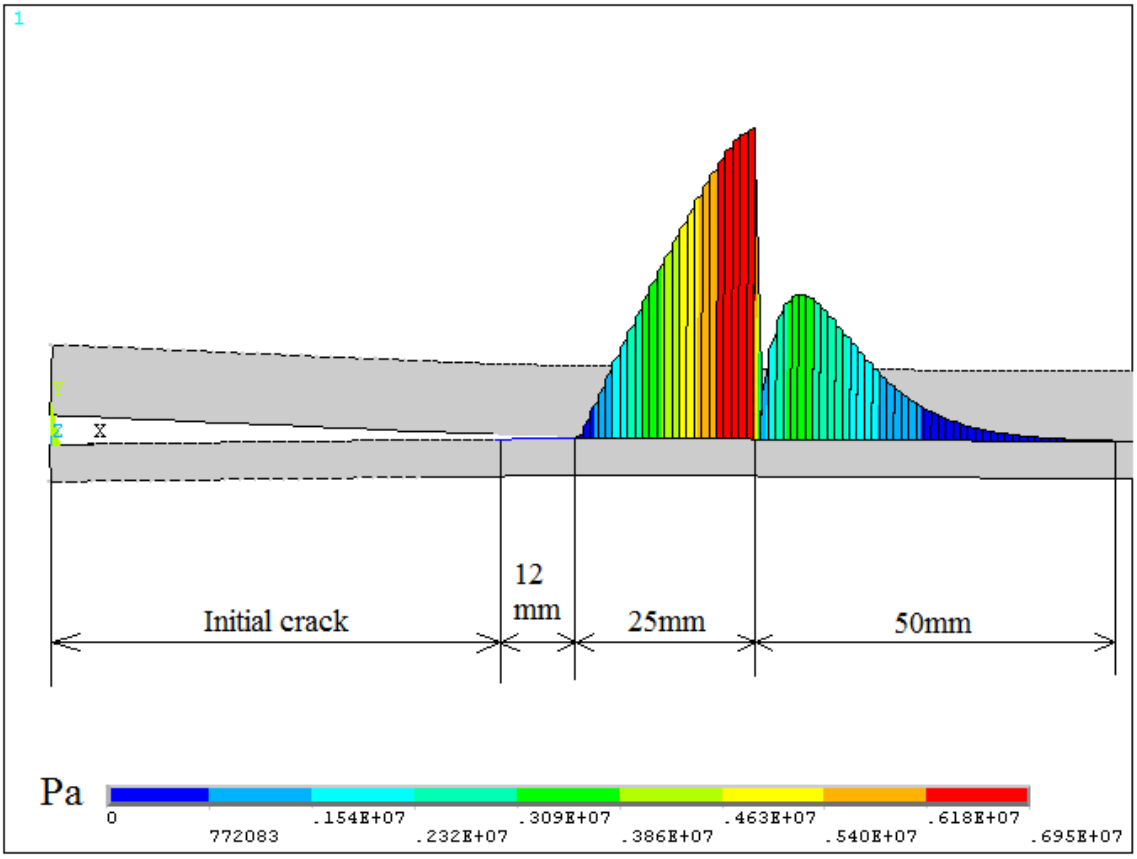

Figure 4.19. Typical fully developed cohesive zone with the two parts of the cohesive zone of the Case 2 model.

4.2.3. Case 3

Finally, the third case of the finite element model studied is presented. This is a simulation of a mixed mode experiment using the data obtained from the cohesive law from specimen MM-4. The input parameters of the cohesive material model can be found in Table 4.5. In Figure 4.20 the deformed shape of the model and the von Mises stress contour are shown at time equal to 0.7.

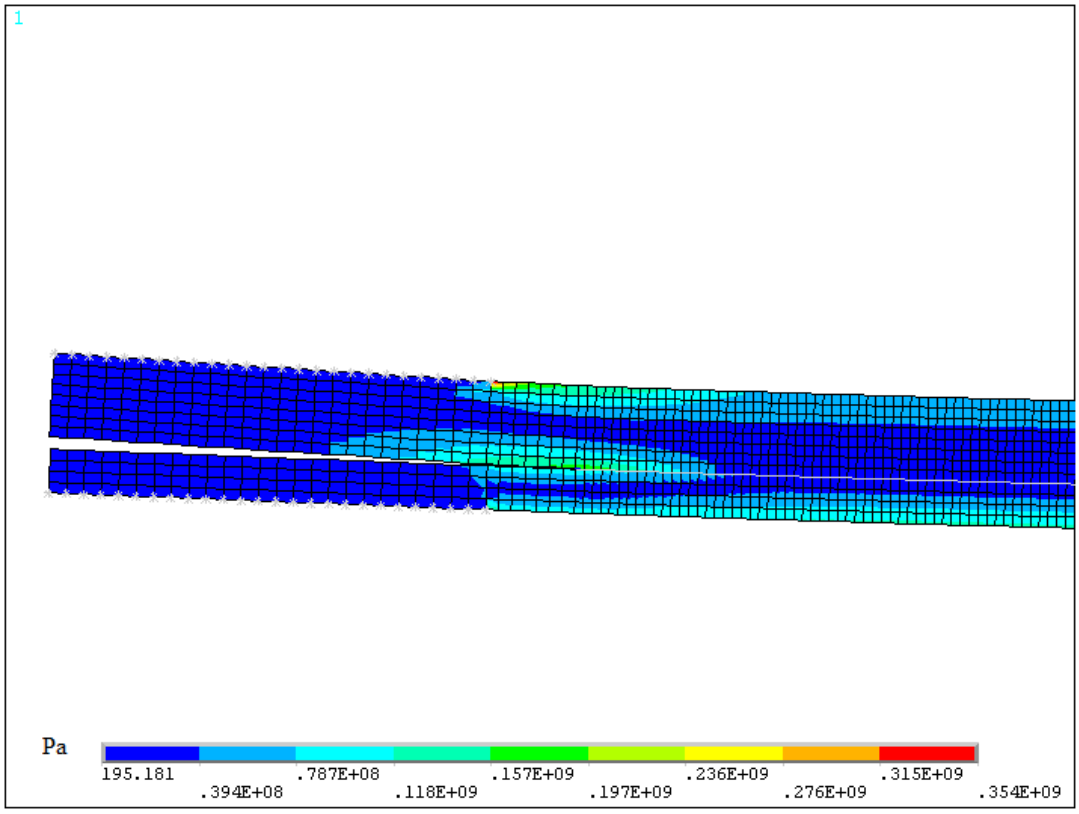

Figure 4.20. Stress contour of the deformed Case 3 model at time=0.7.

The response of the model is the expected; the stress is higher around the crack edge area and the deformed shape of the model shows the two beams moving at the same direction as in the experiments.

The prediction of the load versus the openings follows in Figures 4.21 and 4.22. The model curves present a very good prediction of the experimental results as it can be extracted from the graphs below.

In Figure 4.21 where the load versus the normal crack opening is presented, it can be seen that the predicted curve follows the shape of the experimental curve. The load of the predicted curve increases in a non-linear way with increasing normal opening reaching finally a steady-state value of 0.188kN at the critical normal opening equal to δ_{nc}=0.11mm. The experimental curve presents initially higher load values for the same normal opening compared to the model and as the normal opening reaches the critical value δ_{nc}=0.09mm the steady-state value of the load attained is about 0.18kN. So, there is a deviation of less than 5% between the predicted peak load value and the experimentally measured one.

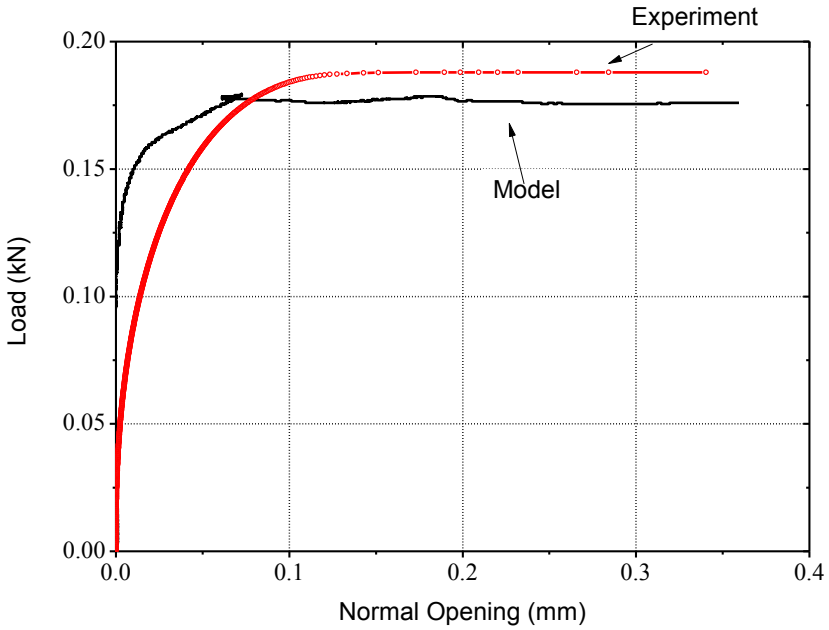

Figure 4.21. Load versus normal opening of the Case 3 model and of the MM-4 specimen.

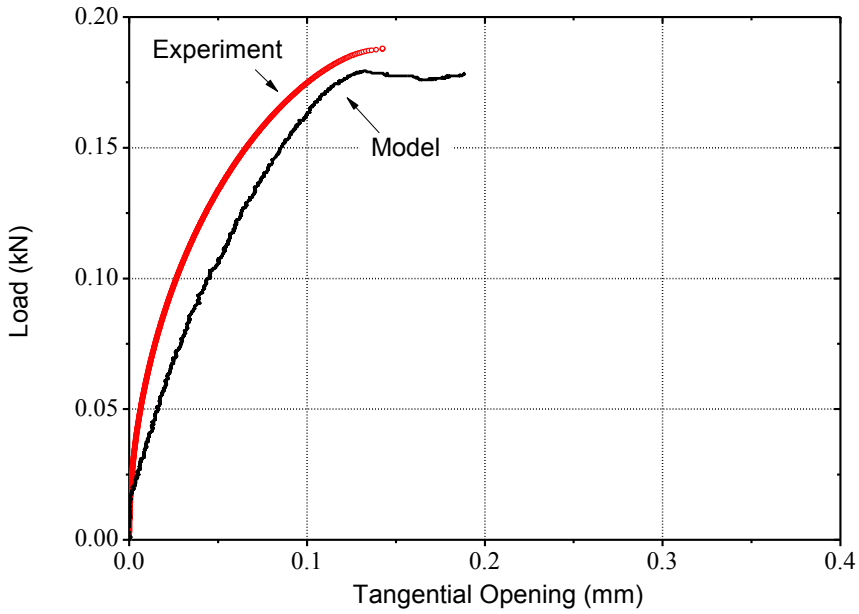

Figure 4.22. Load versus tangential opening of the Case 3 model and of the MM-4 specimen.

In Figure 4.22 the load versus the tangential opening is presented. The model presents significant normal and tangential opening, so a mixed mode experiment was simulated. The results from the model are similar to the experimental; the two curves present the same shape and they reach about the same steady-state value. The load increases non-linearly with increasing tangential opening and it reaches a steady-state value at the critical opening. The model predicts higher values of load for the same opening. The value of the critical opening of the model is at δ_{tc}=0.14mm while for the experimental curve the value is around 0.15mm, so there is a good approximation of the critical tangential opening. The steady-state load value of the model is at 0.175kN while the experimentally measured load reaches a plateau at 0.188kN. The deviation between the two curves is less than 7%.

The fully developed cohesive zone of the model follows in Figure 4.24. The model at time equal to 0.9 is depicted in this graph. The first part of the cohesive zone defined by the linear elastic loading of the cohesive law has a length of 32mm while the second part of the zone defined by the linear softening part of the cohesive law has a length of 50mm. The cohesive zone has a total length of 82mm. The crack has propagated for 15mm at that point.

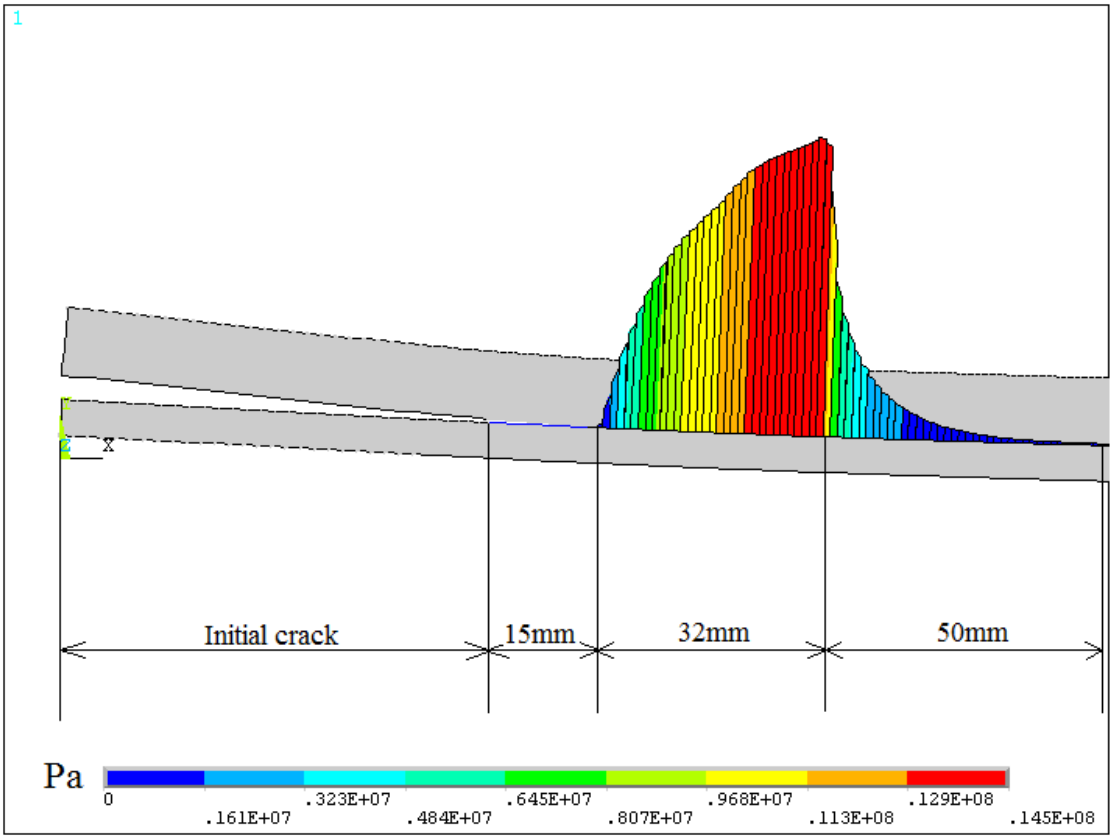

Figure 4.23. Typical fully developed cohesive zone with the two parts of the cohesive zone of the Case 3 model.

5. SUMMARY-CONCLUSIONS

In the present work, a special test set-up was used to experimentally measure the energy release rate of a dissimilar composite-to-steel adhesive joint. The DCB specimen geometry was used with the application of three different pure bending moments combinations. The specimen geometry is then called the Double Cantilever Beam loaded with Uneven Bending Moments (DCB-UBM). The energy release rate was calculated analytically by measuring the crack end normal and tangential openings along with the moments applied on the specimens. The purpose of this study was the derivation of the cohesive laws governing the interface of the adhesive joint and the evaluation of the method used by implementing the obtained cohesive laws to a finite element model and comparing the results between the model and the experiments.

The DCB-UBM test set-up proved to be an excellent choice for the calculation of the energy release rate and the derivation of cohesive laws of an adhesive joint for various mode ratios. Different mode ratios were achieved only by changing the applied moments and so the same specimen geometry was used for all the mode ratios.

The equation which yields the energy release rate was calculated by the J-integral approach along the external boundaries of the specimen in the context of linear elastic fracture mechanics. Assumptions were made so that the calculation of the release rate is feasible; plane stress condtitions were assumed, the adhesive layer was neglected in the analysis and the cohesive laws of Mode I and Mode II were considered as decoupled. The energy release rate was found to reach higher values as the mode mixity increased. In most of the specimens the crack propagated along or very near to the CFRP-adhesive interface with no fiber-bridging being observed. Then, by differentiating the energy release rate with respect to the crack openings, the cohesive stresses were calculated. These cohesive stresses define the cohesive laws of the interface of the joint. An evaluation of the derived cohesive laws had to be made in order to check the feasibility of the proposed analysis. So, the cohesive laws were inserted in a finite element model created with the commercial code ANSYS. Three cases were studied: two for the Mode I tests and one for a mixed mode test using the respective cohesive laws derived from the experiments. Two cases were studied for the Mode I tests since two different set of values were obtained from the experiments. The first set presented higher values of the parameters of the cohesive laws than the second. The prediction of the models for the Mode I tests gave reasonably good results with the first case using the higher cohesive law parameters giving more accurate results than the second case. The mixed mode model simulated the experiments really well and thus proving the feasibility of the analysis that is proposed in this study.

Further work can be proposed in order to obtain more clear results about the fracture characteristics of a dissimilar adhesive joint. In this study, only one adhesive thickness was examined. However, it is known from literature [11] that the adhesive thickness of a joint plays a very important role on its fracture toughness. So, the fracture toughness for different adhesive thicknesses should be also studied for the dissimilar adhesive joint like it was done in [11]. The effect of the adhesive layer to the fracture toughness can then be evaluated for this specimen geometry.

Moreover, cohesive laws from different mode ratios should be evaluated for the DCB-UBM specimen geometry so the complete behavior for all the mode mixities will be known for the adhesive joint. Also, it is important that a pure Mode II test is

made so the cohesive law from that test can be extracted. In this project, the cohesive laws were assumed as decoupled, so the Mode II cohesive law was measured from not a pure Mode II opening test. It has been mentioned before that various assumptions were made for the derivation of the cohesive laws, like neglecting the adhesive layer. An analysis which makes less assumptions would definitely lead to better results. For example, an analutical solution of the energy release rate that would take into account all three materials would give a better evaluation of the fracture data.

Another aspect that can be examined is the crack propagation and the use of a crack starter. During the experiments, no crack starter was used that would lead the crack through a specific interface. So, the crack propagated in different pathway for each specimen. It mainly started propagating inside the adhesive layer (cohesive failure-this part was used for the derivation of the cohesive laws) but as it was seen during the experiments, the crack then moved to the CFRP-adhesive interface. If a crack starter was used, this problem may had been overcome and the crack would have propagated constantly at a specific path.

Finally, concerning the numerical evaluation of the analysis, the cohesive law that was used was of an idealised shape (bilinear). However, this is not the case for the shape of the experimental cohesive laws. So, for a better assessment of the proposed method, different shapes of cohesive laws should be used. Ideally, the same cohesive law that was extracted from the experiments should be implemented in the finite element analysis. Different cohesive law shapes can give better results of the simulation of the experiments.

Appendix A: Calculation of the crack openings

The following calculations are a result from a private communication with Sørensen B.F.. Given the data from the experiments, the crack normal and tangential openings need to be measured. The known dimensions are the data from the measuring devices, Δ_1^{LVDT}, Δ_2^{LVDT} and Δ^{EXT}, the distance D between the measuring points of the LVDT and the thicknesses d_1 and d_2 of the two beams of the DCB-UBM specimen, which can be seen in Figure A.2.

Firstly, the angles θ_1 and θ_2 are defined measured by the difference between the deformed and the undeformed state, as seen in the following Figure A.1.

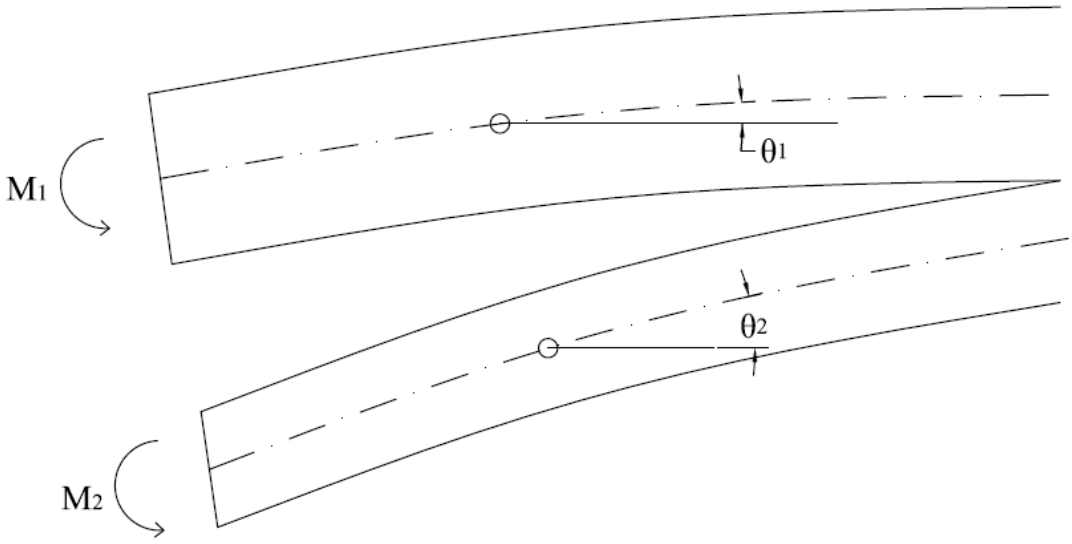

Figure A.1. Drawing representing the undeformed state of the DCB-UBM specimen.

The mean angle θ_3 is defined by

$$\theta_3 = \frac{\theta_1 + \theta_2}{2} \tag{a}$$

Equation (a) also yields

$$\begin{aligned} \theta_1 - \theta_3 &= \theta_1 - \frac{\theta_1}{2} - \frac{\theta_2}{2} = \frac{\theta_1 - \theta_2}{2} \\ \theta_2 - \theta_3 &= \theta_2 - \frac{\theta_1}{2} - \frac{\theta_2}{2} = -\frac{\theta_1 - \theta_2}{2} \end{aligned} \tag{b}$$

By defining angle θ_4 by

$$\theta_4 = \frac{\theta_1 - \theta_2}{2} \tag{c}$$

the previous equations can now be written as

$$\begin{aligned} \theta_1 &= \theta_3 + \theta_4 \\ \theta_2 &= \theta_3 - \theta_4 \end{aligned} \tag{d}$$

Angle θ_4 can be determined first with the help of Figure A.2:

$$m = \Delta_2^{LVDT} - \Delta_1^{LVDT} \tag{e}$$

$$\begin{aligned} \tan(2\theta_4) &= \frac{m}{D} = \frac{\Delta_2^{LVDT} - \Delta_1^{LVDT}}{D} \\ \Rightarrow \theta_4 &= \frac{1}{2} Arc\tan\left(\frac{\Delta_2^{LVDT} - \Delta_1^{LVDT}}{D}\right) \end{aligned} \tag{f}$$

So, the angle θ_4 is given by the known data measured from the LVDT. Trigonometric equations can be used to obtain the following equations:

$$\begin{aligned} g &= \Delta_1^{LVDT} \cos\theta_4 \\ h &= \Delta_1^{LVDT} \sin\theta_4 \end{aligned} \tag{g}$$

$$f_1 = \frac{d_1 \cos\theta_4}{2} \tag{h}$$

$$f_2 = \frac{d_2 \cos\theta_4}{2} \tag{h}$$

$$e_1 = \frac{d_1 \sin\theta_4}{2} \tag{i}$$

$$e_2 = \frac{d_2 \sin\theta_4}{2} \tag{i}$$

All the dimensions above depend on the known Δ_1^{LVDT} and Δ_2^{LVDT} through the angle θ_4.

The mean thickness is defined by:

$$\bar{d} = \frac{d_1 + d_2}{2} \tag{j}$$

A relation for Δ^{EXT} is given through angle θ_5:

$$(\bar{d} + \Delta^{Ext})\cos\theta_5 = n \tag{k}$$

From Figure A.2 the next equation can be obtained:

$$e_2 + n = \delta_t + e_1 \Rightarrow n = \delta_t + (e_1 - e_2) \tag{l}$$

And equation (k) using equations (k) and (l) can now be written as:

$$(\bar{d} + \Delta^{Ext})\cos\theta_5 + (e_2 - e_1) = \delta_t \tag{m}$$

Using trigonometric equation on the triangle defined by the sides Δ_1^{LVDT} and ($\Delta^{EXT}+\bar{d}$) and angle between them $\theta_4+\theta_5$ we obtain the following:

$$\frac{\bar{d}+\Delta^{Ext}}{\sin(90-2\theta_4)}=\frac{\Delta_1^{LVDT}}{\sin\left(\theta_4+90-\theta_5\right)}$$

$$\Rightarrow \sin\left(\theta_4+90-\theta_5\right)=\frac{\Delta_1^{LVDT}}{\bar{d}+\Delta^{Ext}}\sin(90-2\theta_4)$$

$$\Rightarrow \theta_4+90-\theta_5=Arc\sin(\frac{\Delta_1^{LVDT}}{\bar{d}+\Delta^{Ext}}\sin(90-2\theta_4))$$

$$\Rightarrow \theta_5=\theta_4+90-Arc\sin(\frac{\Delta_1^{LVDT}}{\bar{d}+\Delta^{Ext}}\sin(90-2\theta_4))$$

$$\Rightarrow \theta_5=\theta_4+90-Arc\sin(\frac{\Delta_1^{LVDT}}{\bar{d}+\Delta^{Ext}}\cos(2\theta_4)) \quad \text{(n)}$$

Again by using trigonometric equation on the triangle defined by the sides ($\Delta^{EXT}+\bar{d}$) and $p+f_1$ and angle between then $90+\theta_4-\theta_5$, we obtain:

$$(\bar{d}+\Delta^{Ext})\sin\theta_5=p+f_1 \quad \text{(o)}$$

where

$$p=\delta_n+f_2 \quad \text{(p)}$$

Equation (o) using Equations (p), (h) and (j) can now be written as:

$$(\bar{d}+\Delta^{Ext})\sin\theta_5=\delta_n+f_1+f_2$$

$$\Rightarrow \delta_n=(\bar{d}+\Delta^{Ext})\sin\theta_5-(f_1+f_2)$$

$$\Rightarrow \delta_n=(\bar{d}+\Delta^{Ext})\sin\theta_5-\bar{d}\cos\theta_4 \quad \text{(q)}$$

Thus, the normal crack opening can now be measured using Equation (q).

Finally, the tangential crack opening can be obtained by using Equation (m) combined with Equations (i):

$$\delta_t=(\bar{d}+\Delta^{Ext})\cos\theta_5+\frac{d_2-d_1}{2}\sin\theta_4 \quad \text{(r)}$$

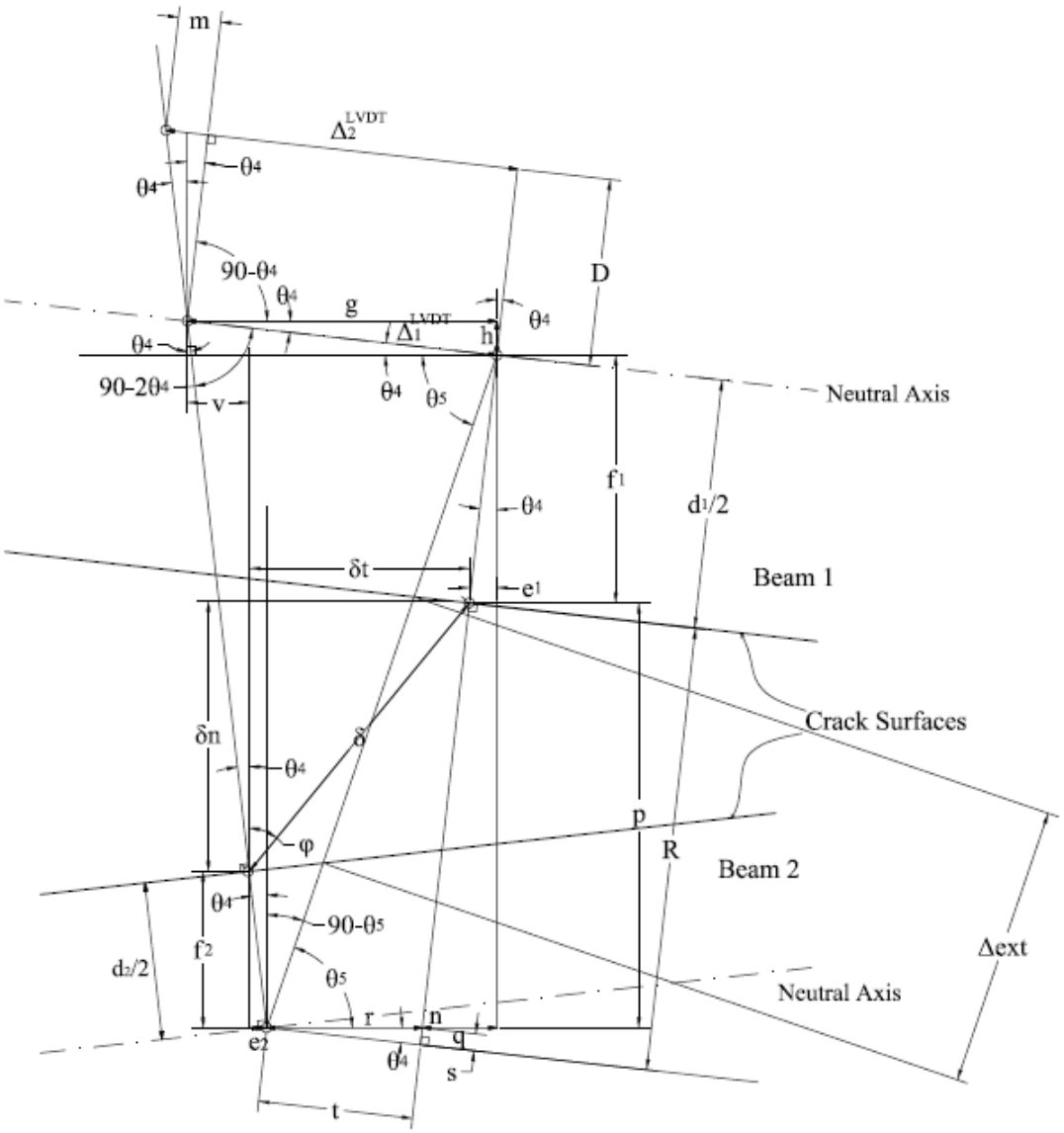

Figure A.2. Schematic drawing of the crack opening with the dimensions used to calculate the openings δ_n and δ_t.

REFERENCES

1. Mazza et al., 2006 P. Mazza, F. Martini, B. Sala, M. Magi, M. Colombini, G. Giachi, F. Landucci and C. Lemorini, A new Palaeolithic discovery: tar-hafted stone tools in a European Mid-Pleistocene bone-bearing bed, *Journal of Archaeological Science* **33**
2. Williams M. L., 1969 Journal of Applied Polymer Science 13,29
3. Williams M. L., 1959, "The Stress Around a Fault or Crack in Dissimilar Media," Bull. Seismol. Soc. Am., **49**, pp. 199–204.
4. Barenblatt, G. I., 1959, "The Formation of Equilibrium Cracks During Brittle Fracture. General Ideas and Hypotheses. Axially-Symmetric Cracks," J. Appl.Math. Mech., **23**, pp. 622–636.
5. Dugdale, D. S., 1960, "Yielding of Steel Sheets Containing Slits," J. Mech. Phys. Solids, **8**, pp. 100–104.
6. Rice, J. R., 1968, "A Path Independent Integral and the Approximate Analysis of Strain Concentration by Notches and Cracks," ASME J. Appl. Mech., **35**, pp. 379–386.
7. Zhang Z, Paulino GH, 2004, Cohesive zone modelling of dynamic failure in homogeneous and functionally graded materials. Int J Plasticity 21:1195–1254
8. Sorensen, B.F., Kirkegaard, P., 2006. Determination of mixed mode cohesive laws. Eng. Fract. Mech. 73, 2642–2661.
9. Yang QD, Thouless MD., 2001, Mixed-mode fracture analysis of plastically deforming adhesive joints. Int J Fract;110:175–87
10. Alfano G., 2005, On the influence of the shape of the interface laws on the application of cohesive-zone models
11. Ji G. et al., 2010, Effects of adhesive thickness on global and local Mode-I interfacial fracture of bonded joints
12. Zhenyu Ouyang, Gefu Ji, Guoqiang Li, 2010, On Approximately Realizing and Characterizing Pure Mode-I Interface Fracture Between Bonded Dissimilar Materials
13. Russell, A.J., 1982. On the measurement of mode II interlaminar fracture energies. Materials Report 82-0, Defence Research, Establishment Pacific, Victoria, British Columbia, Canada.
14. Leffler K., Alfredsson K.S., Stigh U., 2005, Shear behavior of adhesive layers
15. Silva M.A.L., Morais J.J.L., de Moura M.F.S.F., Lousada J.L., 2006, Mode II wood fracture characterization using the ELS test.
16. De Moura M.F.S.F., Oliveira J.M.Q., Morais J.J.L., Xavier J., 2009, Mixed-mode I/II wood fracture characterization using the mixed-mode bending test
17. Choupani N., 2007, Mixed-mode cohesive fracture of adhesive joints: Experimental and numerical studies.
18. Shivakumar K.N., Crews J.H., Avva V.S. Jr., 1998, Modified mixed- mode bending test apparatus for measuring delamination fracture toughness of laminated composites. J Compos Mater 32:804–828
19. Jurton T.J., Dalzel-Job J., Livingstone F., 2003, Oil platforms, destroyers and frigates-case studies of QinetiQ's marine composite patch repairs.
20. E.A.S. Marques and L.F.M. da Silva, 2008, Joint strength optimization of adhesively bonded patches, The Journal of Adhesion, 84: 915:934.
21. Sorensen BF, Jacobsen T.K., 2008, Characterizing delamination of fibre composites by mixed mode cohesive laws
22. Suo Z, Hutchinson JW, 1990, Interface crack between two elastic layers. Int J Fract 43(1):1-18
23. Ostergaard RC, Sorensen BF, 2006, Interface crack in sandwich specimen
24. ANSYS, User's Manual